NONLINEAR DYNAMICS OF RESONANCES IN, AND EJECTION FROM, PAUL TRAPS

A Thesis

Submitted for the Degree of

Doctor of Philosophy

in the Faculty of Engineering

By

N Rajanbabu

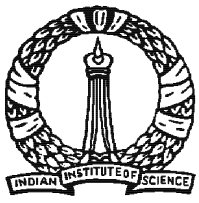

Department of Instrumentation

Indian Institute of Science

Bangalore - 560 012, India

September 2006

Dedicated
with regards and gratitude to

my research supervisors
Prof A G Menon and Prof Anindya Chatterjee
who motivated, guided and helped me in all possible ways
which I can never repay

&
Vaidya Balendu Prakash
who literally saved my life from the clutches of leukaemia

&
my wife
Geetha
who carried me during my times of trial and suffering

Acknowledgements

Writing 'Acknowledgements' is trying to translate gratitude into words which is a bit difficult when one's heart is filled with emotions. No book is ever written alone and no research endeavor is ever carried out in solitude. This thesis is no exception and I owe much, to many for its successful completion.

First of all, I would like to thank my research supervisors Prof. A. G. Menon and Prof. Anindya Chatterjee whose dedication and commitment to scientific research was the primary force in carrying out this research successfully.

Prof. Menon is more than a guide, he is a true 'friend, philosopher and guide' to me. In my acquaintance with him for the past 11 years, he has been a friend so close to my heart, an elder brother who stood by me in my troubled times, someone who deeply influenced me in the way I look at life and people, and a perfect guide when it comes to the domain of research. I record my deep sense of gratitude to Prof. Menon.

I am very much indebted to my co-guide Prof. Anindya Chatterjee whose direct involvement and motivation helped me to complete this work. His profound knowledge in nonlinear dynamics, sage advice and insightful criticisms has helped this thesis in innumerable ways.

The first problem of this thesis was a collaborative effort with Mr. Amol Marathe. Amol has been helpful to me in many ways through out my research. I owe him a deep debt of gratitude.

Prof. R M Vasu has always been a source of inspiration for me. I am grateful to him for allowing me to use the various facilities available in the department. I gratefully acknowledge the help and support I received from Prof. A Mohanty at various stages of my work. I am also thankful to Prof. Rangarajan and Prof. Vittal Rao for allowing me to audit their courses.

I thank Dr Uday Balakrishnan for providing me married apartment under DDQ. I gratefully acknowledge the encouragement and support I received from Dr Sevugarajan, Mr. Jiss Paul, Ms. Sandhya L Rao, Dr Shivaprkash, Dr Shrath Ahuja, Mr. Paneer Selvam, Mr. Dnyanesh, Mr. Ramkrishna Reddy, Mr. Deepak, Mr. Shivyogi and Mr. Pushkar. I would like to render a special thanks to Mr. Renuka Prasad for his suggestions and encouragement. Also I thank Lt. Prasanna N for his support and help during the initial stages of my research work. I thank Ms. Krishna Veni and Mr. Pavan T for helping me through out the preparation of my thesis. I also thank the office staff of Department of

Instrumentation, Mr. Nataraj and Ms. Udayakumari, for the timely help and assistance rendered by them.

I have learned much from the personal contact of Rajeev (CET) and Muralikrishnan (NITC). I thank them for their support and valuable suggestions at various stages of my work. I also thank Suresh, Ashraf, Rajmohan, Shahid, Harshan, Hari, Bijuna, Usha for their support. I acknowledge the help and support rendered by Viswanathan, Sindhu, Sudhir, Vasudevan, Vinod and Venugopal.

I thank Prof. Vinod A P (NTU, Singapore), Mr. Ajeesh P Kurian (Panasonic, Singapore), Mr Jaison Ambadan (Canada) for gathering literature which were not available at IISc. I would like to thank Mr Jaison, Mr Hari Varma and Mr Sumesh for helping me in sorting out various problems in computation.

Past one year has been a period of trial for me. My research called for non-academic inputs as well. I should acknowledge the hands that helped and the lips that prayed for my life. It is not possible to name them all. But I must at least mention the following friends who have been crucially significant in my recovery and return to normal life: Sreenadhan and Sailaja, Sunil and Jessy, Ramanujan, Sobhana, Sobhana's parents and sisters, Serji and Mini, George and Meena, Dani Thomas, Vinod and Smitha, Madan and Uma, Rajeevan, C L Thomas, Rakesh, Jaya and her mother, Sidhatrhan sir and Parvathy, Jagadanannd, Ajith Zachariah, NN Krishnadas, Kalakath Radhakrishnan.

In a special way I want to thank the doctors who have been so supportive of me during my illness: Dr Satheesh Rao of our health center, Dr Paul Sebastian, Dr Ramdas K and Dr Raichel Cherian (RCC), Dr Madanmohan (UK) and Dr Ramasway (PKD).

I thank Indian Institute of Science for providing the facilities for research. I thank Govt of Kerala and NSS College of Engineering for granting me deputation under QIP. I thank my colleagues at department of Instrumentation, NSSCE for their support and encouragement.

I thank my dear friends Sunil and Sreenathan for their continuous help and support which keeps me optimistic in life.

Now, I should acknowledge the people at home to whom I owe much. They were the real force behind me to guide this boat to its shore, in the midst of a plethora of problems. I would like to place my immense gratitude to Smt. Anandavally, my mother-in-law, who acted as a pivot of our family neglecting her own health problems. I thank my mother Janaki Amma, my brother Mohandas and other family members and relatives for their love and support. I thank my nephew Ajith for taking care of my children when I was away for treatment. Words are not enough to thank my wife Geetha, who is love incarnate. A perfect partner in life in all respects, she symbolizes all the sufferings of womanhood and has still remained my asylum throughout my life. Our kids, Ammu and Appu, though denied the parental cares at times were graceful enough to accept the situation and I thank them for enriching our life.

N Rajanbabu,
18 September, 2006

Preface

This thesis presents results of investigations that have been carried out to understand ion dynamics in Paul trap mass spectrometers. These mass spectrometers have a three electrode geometry mass analyzer consisting of a central ring electrode and two end cap electrodes. Although the electrode shape and electric potentials (applied across the electrodes) are designed to create a linear trapping field, misalignments in the geometry as well as experimental constraints introduce weak nonlinear fields within the trap cavity. This results in altering trap performance by way of affecting mass resolutions and mass assignments, in addition to causing nonlinear resonances which destabilize ions from the trap. Of the three problems that have been taken up for study in this thesis, the first concerns understanding early/delayed ejection of ions in mass selective boundary ejection experiments. The second looks at the differential resolution observed in forward and reverse scan resonance ejection experiments. The third study explores a coupled nonlinear resonance within the nominally stable region of trap operation.

The thesis has been divided into six chapters. Chapter 1 presents some background information to help understand the Paul trap mass spectrometer. We begin with a description of the Paul trap mass spectrometer and present the Mathieu equation which describes the motion of ions within the *ideal* trap. The nonlinear Mathieu equation and the Duffing equation, two equations which have been used in our studies, are next presented. This is followed by describing two modes of operation of the mass spectrometer which have been investigated in this thesis. Finally, the scope of the thesis is outlined.

In Chapter 2 we use the method of multiple scales to elucidate dynamics associated with early and delayed ejection of ions in mass selective ejection experiments in Paul traps. We develop a slow flow equation to approximate the solution of a weakly nonlinear Mathieu equation to describe ion dynamics in the neighborhood of the stability boundary of ideal traps (where the Mathieu parameter $q_z = q_z^* = 0.908046$). The method of multiple scales enables us to incorporate higher order multipoles, extend computations to higher orders, and generate phase portraits through which we view early and delayed ejection.

Our use of the method of multiple scales is atypical in two ways. First, because we look at boundary ejection, the solution to the unperturbed equation involves linearly growing terms, requiring some care in identification and elimination of secular terms. Second, due to analytical difficulties, we make additional harmonic balance approximations within the formal implementation of the method.

For *positive* even multipoles in the ion trapping field, in the stable region of trap operation, the phase portrait obtained from the slow flow consists of three fixed points, two of which are saddles and the third is a center. As the q_z value of an ion approaches q_z^*, the saddles approach each other, and a point is reached where all nonzero solutions are unbounded, leading to an observation of early ejection.

The phase portraits for *negative* even multipoles and odd multipoles of either sign are qualitatively similar to each other and display bounded solutions even for $q_z > q_z^*$, resulting in the observation of delayed ejection associated with a more gentle increase in ion motion amplitudes, a mechanism different from the case of the *positive* even multipoles.

In Chapter 3 we present a study of constraints on pre-ejection dynamical states which cause differential resolution in resonance ejection experiments using Paul traps with stretched geometry. Both analytical and numerical computations are carried out to elucidate the role of damping and scan rate in influencing coherence in ion motion associated with the forward and reverse scan.

Adopting the Dehmelt approximation, our analytical study is carried out on a damped, driven Duffing oscillator with octopole nonlinearity. Using the method of multiple scales, we derive approximate slow flow equations which describe the ion motion. The phase portraits generated from the slow flow equations, in the vicinity of the jump, display two stable equilibria (centers) and an unstable fixed point (saddle). Numerical studies on the original equation are used to understand the influence of damping and scan rate in causing coherent ion ejection in these experiments.

In the forward scan experiments, for a given damping, low scan rates result in coherent motion of ions of a given mass at the jump point. At this point, the amplitude and phase of ions of a given mass, starting at different initial conditions, become effectively identical. As the scan rate is increased, coherence is destroyed. For a given scan rate, increasing damping introduces coherence in ion motion, while decreasing damping destroys this coherence.

In reverse scan experiments, for a given damping, very low scan rates will cause coherent ion motion. Increasing the scan rate destroys this coherence.

The effect of damping in reverse scan experiments is qualitatively similar to that in

the forward scan experiments, but settling times in the forward scan are shorter, leading to improved coherence and resolution. For mass spectrometrically relevant scan rates and damping values, significantly greater coherence is obtained in the forward scan.

Chapter 4 is a preliminary investigation of some coupled resonances in Paul traps. Here we identify the points in the Mathieu stability diagram where coupled resonances occur in experimental Paul traps. We use the harmonic balance method to determine the a_z and q_z values corresponding to such resonant points, from the ideal Mathieu equation. The coupled nonlinear Mathieu equation accommodating octopole, decapole and dodecapole superpositions is numerically solved to study the nature of instability occurring in the neighborhood of these points.

The Poincaré sections are presented at select points on the Mathieu stability plot to demonstrate the variety of behavior. Among the six points studied one displays stable behavior, two display instability only in the z direction, and others show simultaneous instability in z and r directions. The coupled resonance occurring in the neighborhood of $a_z^* = -0.2313850427$ and $q_z^* = 0.9193009931$ is then selected for detailed investigation in Chapter 5. This corresponds to the intersection of $\beta_r = \frac{1}{2}$, $\beta_z = \frac{1}{2}$, $\beta_r + \beta_z = 1$. The r-direction or z- direction motions, in the neighborhood of this point, are not individually unbounded; however, if both r and z are nonzero, then there is an instability that leads to unbounded solutions.

In Chapter 5 we study the weakly coupled and nonlinear Mathieu equations governing ion motion in axial and radial directions in a Paul trap in the neighborhood of the above mentioned $a_z^* = -0.2313850427$ and $q_z^* = 0.9193009931$. Using harmonic balance based approximate averaging up to second order, we obtain a slow flow that, we numerically demonstrate, approximates the actual ion dynamics. We find that the slow flow is Hamiltonian. We study the slow flow numerically with the objective of exploring and displaying some of the possible types of interesting ion motions. In particular, we choose specific but arbitrary parameter values; study the stability of the individual radial and axial motion invariant manifolds; examine the rather large times associated with escape of ions; notice regions in the averaged phase space wherein trajectories do not, in fact, escape; observe apparently chaotic dynamics preceding escape for ions that do escape; and note that trajectories that do not escape appear to be confined to 4-tori. We conclude with some comments on the implications for practical operation of the Paul trap near this resonant point.

Chapter 6 presents the concluding remarks of this thesis.

Contents

Preface **i**

List of Figures **viii**

List of Tables **xiii**

1 Introduction **1**

1.1 The Paul trap mass spectrometer 2

1.2 Motion of ions in a Paul trap 3

1.2.1 The Mathieu equation 3

1.2.2 Mathieu stability plot 4

1.2.3 Secular frequency 5

1.2.4 Nonlinear Mathieu equation 6

1.2.5 Forced, damped Duffing equation 8

1.3 Modes of operation 9

1.3.1 Mass selective boundary ejection 9

1.3.2 Resonance excitation 10

1.4 Scope of the thesis 11

2 Multiple scales analysis of early and delayed boundary ejection in Paul traps **13**

2.1 Introduction 13

2.2 Equation of motion . . . 15
2.3 Analysis using multiple scales . . . 17
2.3.1 Solution at $\mathcal{O}(1)$ . . . 18
2.3.2 Solution at $\mathcal{O}(\sqrt{\epsilon})$ . . . 20
2.3.3 Solution at $\mathcal{O}(\epsilon)$ . . . 22
2.3.4 Numerical verification . . . 23
2.4 Results and discussion . . . 25
2.4.1 Positive octopole . . . 27
2.4.2 Negative octopole . . . 27
2.4.3 Hexapole . . . 29
2.4.4 Decapole . . . 30
2.4.5 Positive dodecapole . . . 31
2.4.6 Negative dodecapole . . . 32
2.5 Concluding remarks . . . 32
2.6 Appendix . . . 34
2.6.1 Fourth order MMS slow flow . . . 34
2.6.2 Choice of time scales in MMS . . . 35
2.6.3 Expressions for X_1 and X_2 . . . 36
2.6.4 Comparison of second order slow flow with beat envelope equation of Sudakov (2001) . . . 37
2.6.5 Initial condition calculation . . . 39

3 Motional coherence during resonance ejection of ions from Paul traps 41
3.1 Introduction . . . 41
3.2 Equation of motion . . . 43
3.3 Analytical treatment . . . 45
3.3.1 Numerical verification . . . 48

3.4 Results and discussion 51
3.4.1 Phase portraits 52
3.4.2 Mass resolution 54
3.4.3 Damping, scan rate, and coherence 54
3.4.4 Numerical simulations 57
3.5 Concluding remarks 58

4 Preliminary study of some coupled resonances 63
4.1 Introduction 63
4.2 Equations of motion 64
4.3 Nonlinear resonances 65
4.4 Numerical study 69
4.5 Concluding remarks 75

5 Approximate averaging of coupled radial/axial ion motions in Paul trap near a double resonance point 77
5.1 Introduction 77
5.2 Harmonic balance and initial numerics 78
5.3 Analytical treatment 79
5.3.1 Change of variables 79
5.3.2 Verification of modified equations 82
5.3.3 Averaging 83
5.4 Numerical investigation of the averaged equations 87
5.4.1 Invariant manifolds 87
5.4.2 Neighborhoods of invariant manifolds 87
5.4.3 Further investigation of specific solutions 90
5.4.4 Probabilities of escape 91
5.4.5 Closer look at $R = 0.2738$ 92

5.4.6 Further investigation of the dependence on θ 92

5.5 Concluding remarks 99

5.6 Appendix 100

5.6.1 Linearly independent solutions of the unperturbed Mathieu equations at $a_z = -0.2313850427$ and $q_z = 0.9193009931$. 100

5.6.2 First order slow flow equations. 101

5.6.3 Second order slow flow equations 102

6 Summary and concluding remarks **105**

References **107**

List of Figures

1.1 Paul trap mass analyzer 2

1.2 Mathieu stability plot 5

1.3 Experimental set up for resonance ejection experiment 10

2.1 Comparison of amplitude (A) determined by solving the slow flow with the original Mathieu equation ($\bar{z}$) for positive and negative octopole. In both plots, $\epsilon = 0.001$, $\bar{z}(0) = 0.01$, $\dot{\bar{z}}(0) = 0$, $A(0) = 0.0091$, $\dot{A}(0) = 0$ and $\bar{h} = \bar{d} = \bar{k} = 0$. Further, we use for (a) $\bar{f} = 1$, $\Delta = -1$; and for (b) $\bar{f} = -1$, $\Delta = 1$. 24

2.2 Comparison of amplitude (A) determined by solving the slow flow with the original Mathieu equation ($\bar{z}$) for hexapole and decapole. In both plots, $\epsilon = 0.001$, $\Delta = 1$, $\bar{z}(0) = 0.01$, $\dot{\bar{z}}(0) = 0$ and $\bar{f} = \bar{k} = 0$. Further, we use for (a) $\bar{h} = 1$, $\bar{d} = 0$, $A(0) = 0.0091$, $\dot{A}(0) = 0$; and for (b) $\bar{d} = 1$, $\bar{h} = 0$, $A(0) = 0.0101$, $\dot{A}(0) = 0$. 24

2.3 Comparison of amplitude (A) determined by solving the slow flow with the original Mathieu equation ($\bar{z}$) for positive and negative dodecapole. In both plots, $\epsilon = 0.001$, $\bar{z}(0) = 0.01$, $\dot{\bar{z}}(0) = 0$, $A(0) = 0.0091$, $\dot{A}(0) = 0$ and $\bar{h} = \bar{f} = \bar{d} = 0$. Further, we use for (a) $\bar{k} = 1$, $\Delta = -1$; and for (b) $\bar{k} = -1$, $\Delta = 1$. 25

2.4 Phase portrait for 1% octopole ($f = 0.01$, $\bar{f} = 20$, $\epsilon = 0.001$) for Δ values of (a) -2, (b) -0.5, (c) -0.1 and (d) -0.001. 28

2.5 Phase portrait for -1% octopole ($f = 0.01$, $\bar{f} = 20$, $\epsilon = 0.001$) for Δ values of (a) -1, (b) 0, (c) 2 and (d) 8. 29

2.6 Phase portrait for 1% hexapole ($h = 0.01$, $\bar{h} = 0.47$, $\epsilon = 0.001$) for Δ values of (a) -1, (b) 0, (c) 0.25 and (d) 0.6. 30

2.7 Phase portrait for 1% decapole ($d = 0.01$, $\bar{d} = 0.79$, $\epsilon = 0.001$) for Δ values (a) -1, (b) 0, (c) 0.25 and (d) 2. 31

2.8 Phase portrait for 1% dodecapole ($k = 0.01$, $\bar{k} = 30$, $\epsilon = 0.001$) for Δ values of (a) -0.5, (b) -0.1, (c) -0.01 and (d) -0.001. 32

2.9 Phase portrait for -1% dodecapole ($k = 0.01$, $\bar{k} = 30$, $\epsilon = 0.001$) for Δ values of (a) -1, (b) 0, (c) 1 and (d) 8. 33

2.10 Time period of the amplitude for (a) $\epsilon = 0.001$ and (b) $\epsilon = 0.002$. 36

2.11 Comparison between amplitude obtained by (Eq. (2.53)) and Eq. (2.52) for $\alpha_3 = 0.02828$ (4% hexapole), $q = q_0 = 0.908046$, $u(0) = 0.01, \dot{u}(0) = 0, Z(0) = 0.01, \dot{Z}(0) = 0$. 39

3.1 Escape velocity versus q_z. (1) unforced equation, (2) $V_s = 100$ mV, (3) $V_s = 200$ mV. 45

3.2 (a) Phase portrait of the system ((Eqs. (3.28) and (3.29)) at $\nu = 1.2$ ($\delta = 0.44$), $V_s = 500$ mV, $\alpha_3 = 0.4$, $\mu = 0$. (b) The time response from the original equation and amplitude from the slow flow for the initial condition corresponding to point P on the phase portrait. 49

3.3 Phase trajectories of slow flow equations generated for mass 78 Th, $V_s = 500$ mV, pressure = 1 Pascal and +5% octopole superposition at $\nu = 1.2$. 50

3.4 Amplitude-response curve of an ion of mass 78 Th with pressure= 0.1 Pascal and +5% octopole superposition. (—) for $V_s = 500$ mV, (....) for $V_s = 1.5$ V. (*) denotes the amplitude obtained from the slow flow equations. 51

3.5 Phase portraits of the system ((Eqs. (3.28) and (3.29)) for $V_s = 500$ mV, $\alpha_3 = 0.4$, $\mu = 0$ (no damping) at (a) $\nu = 0.8$ ($\delta = -0.36$) (b) $\nu = 1.2$ ($\delta = 0.44$). . . . 52

3.6 Amplitude-response plots and phase portraits plotted at (a) $\nu = 0.8$, (b) $\nu = 1.0$, (c) $\nu = 1.08$, (d) $\nu = 1.09$, (e) $\nu = 1.1$, (f) $\nu = 1.2$. 53

3.7 (a) Amplitude-response curves of ions of mass 78 Th and 79 Th with pressure= 0.1 Pascal and +5% octopole superposition and $V_s = 500$ mV. (b) Magnified region close to the jump point 55

3.8 Time trajectories in the forward scan for initial conditions (a) (0.1, 0) and (b) (0.25, 0), in the absence of damping. $\nu_0 = 3$, $\gamma = -0.0005$. The trajectories for the two initial conditions in the vicinity of the trap boundary ($\bar{z} \approx 0.7$) are presented in (c). Light curve corresponds to initial condition (0.1, 0) and dark curve corresponds to initial condition (0.25, 0). 59

3.9 Time trajectories in the reverse scan for initial conditions (a) (0.1, 0) and (b) (0.25, 0), in the absence of damping. $\nu_0 = 0.1$, $\gamma = 0.0005$. The trajectories for the two initial conditions in the vicinity of the trap boundary ($\bar{z} \approx 0.7$) are presented in (c). Light curve corresponds to initial condition (0.1, 0) and dark curve to initial condition (0.25, 0). 59

3.10 Time trajectories in the forward scan for initial conditions (a) (0.1, 0) and (b) (0.25, 0), He gas pressure 0.1 Pascal, $\nu_0 = 3$, $\gamma = -0.0005$. The trajectories for the two initial conditions in the vicinity of the trap boundary ($\bar{z} \approx 0.7$) are presented in (c). Continuous curve corresponds to initial condition (0.1, 0) and '*' to initial condition (0.25, 0). 60

3.11 Time trajectories in the reverse scan for initial conditions (a) (0.1, 0) and (b) (0.25, 0), He gas pressure 0.1 Pascal, $\nu_0 = 0.1$, $\gamma = 0.0005$. The trajectories for the two initial conditions in the vicinity of the trap boundary ($\bar{z} \approx 0.7$) are presented in (c). Light curve corresponds to initial condition (0.1, 0) and dark curve to initial condition (0.25, 0). 60

3.12 Time trajectories in the reverse scan for initial conditions (a) (0.1, 0) and (b) (0.25, 0), He gas pressure 1 Pascal, $\nu_0 = 0.1$, $\gamma = 0.0005$. The trajectories for the two initial conditions in the vicinity of the trap boundary ($\bar{z} \approx 0.7$) are presented in (c). Light curve corresponds to initial condition (0.1, 0) and dark curve to initial condition (0.25, 0). 61

3.13 Time trajectories in the forward scan for initial conditions (a) (0.1, 0) and (b) (0.25, 0), He gas pressure 0.1 Pascal, $\nu_0 = 3$, $\gamma = -0.0051$. The trajectories for the two initial conditions in the vicinity of the trap boundary ($\bar{z} \approx 0.7$) are presented in (c). Light curve corresponds to initial condition (0.1, 0) and dark curve to initial condition (0.25, 0). 61

4.1 Nonlinear resonance lines in Mathieu stability plot 66

4.2 Poincaré sections in the z and r direction at $a_z = -0.23131$ and $q_z = 0.91919$ for 10% hexapole and 10% octopole superposition corresponding to point A in Fig. 4.1. 70

4.3 Poincaré sections in the z and r direction at $a_z = -0.0365$ and $q_z = 0.8226$ for 10% hexapole, 10% octopole, 10% decapole and 10% dodecapole superposition corresponding to point B in Fig. 4.1. 72

4.4 Poincaré sections in the z and r direction at $a_z = -0.0119$ and $q_z = 0.6556$ for 10% hexapole, 10% decapole and 10% dodecapole superposition corresponding to point C in Fig. 4.1. 72

4.5 Poincaré sections in the z and r direction at ($a_z = -0.1079$, $q_z = 0.6423$) for 10% decapole and 10% dodecapole superposition corresponding to point D in Fig. 4.1. 73

4.6 Poincaré sections in the z and r direction at $a_z = -0.1531$ and $q_z = 0.7582$ for 10% decapole superposition corresponding to point E in Fig. 4.1. 73

4.7 Poincaré sections in the z and r direction at $a_z = -0.1088$ and $q_z = 0.7792$ for 10% hexapole, 10% decapole and 10% dodecapole superposition corresponding to point F in Fig. 4.1. 74

4.8 Poincaré sections of the uncoupled solutions in r direction and z direction at $a_z = -0.23131$ and $q_z = 0.91919$ for 10% hexapole and 10% octopole superposition. 76

5.1 Poincaré sections of the uncoupled solutions for two different sets of initial conditions at $a_z = -0.23131$, $q_z = 0.91919$ and for $h = f = 0.1$. (a) z-direction, obtained by setting $\bar{r} \equiv 0$, and (b) r-direction, obtained by setting $\bar{z} \equiv 0$. 79

5.2 Poincaré sections of the coupled solutions at $a_z = -0.23131$, $q_z = 0.91919$ and for $h = f = 0.1$. Initial conditions for $(\bar{z}, \dot{\bar{z}}, \bar{r}, \dot{\bar{r}}) = (0.05, 0, 0.05, 0)$. (a) z-direction motion (b) r- direction motion. 80

5.3 (a) A_{zeval} (from original equations) and A_z (modified equations) versus time (b) A_{reval} (from original equations) and A_r (modified equations) versus time for $\epsilon = 0.02$, $\bar{h} = \bar{f} = 1$, $\bar{a}_z = -0.3$, $\bar{q}_z = 0.1$. 83

5.4 (a) A_{zeval} (from original equations) and A_z (averaged equations) versus time and (b) A_{reval} (from original equations) and A_r (averaged equations) versus time for $\epsilon = 0.02$, $\bar{h} = \bar{f} = 1$, $\bar{a}_z = -0.3$, $\bar{q}_z = 0.1$. 86

5.5 Phase portraits generated for the invariant manifolds (a) $(A_r = 0, B_r = 0)$ and (b) $(A_z = 0, B_z = 0)$ for $\epsilon = 0.02$, $\bar{h} = \bar{f} = 1$, $\bar{a}_z = -0.3$, $\bar{q}_z = 0.1$. 88

5.6 Stability of invariant manifolds (a) ($A_z = 0$, $B_z = 0$) (b) ($A_r = 0$, $B_r = 0$). See text for details. 89

5.7 Zoomed portion of the plot of A_z (-), B_z (..), A_r (- -) and B_r (- . -) for (a) $A_r(0) = 0.2215$ and $B_r(0) = 0.1609$ (b) $A_r(0) = 0.1369$ and $B_r(0) = 0.2371$. . . . 91

5.8 Probability of escape versus R for $\bar{\tau} < 3000$ (A), $\bar{\tau} < 6000$ (B), $\bar{\tau} < 12000$ (C). . 93

5.9 Normalized values of k, and hence $\theta/(2\pi)$, for which no escape occurs within $\bar{\tau} = 12000$. 93

5.10 (a) Trajectories and (b) Poincaré section for $k = 27$. 94

5.11 (a) Trajectories and (b) Poincaré section for $k = 63$. 94

5.12 (a) Trajectories and (b) Poincaré section for $k = 197$. 95

5.13 (a) Trajectories and (b) Poincaré section for $k = 422$. 95

5.14 Plot of A_z, B_z, A_r, B_r versus τ for $k = 28.7050$. 96

5.15 Trajectory and Poincaré section for $k = 28.7050$. 96

5.16 Plot of A_z, B_z, A_r, B_r versus τ for $k = 28.7055$. 97

5.17 Trajectory and Poincaré section for $k = 28.7055$. 97

5.18 Plot of A_z, B_z, A_r, B_r versus τ for $k = 28.7060$. 98

5.19 Trajectory and Poincaré section for $k = 28.7060$. 98

List of Tables

2.1 Values of a_k's and b_k's. 20

2.2 q_z at different values of Δ, for $\epsilon = 0.001$. 26

4.1 Nonlinearities and resonance curves. 65

4.2 a_z^* and q_z^* at the intersection of nonlinear resonance curves. 69

4.3 Stability of ion motion for different combinations of higher order superpositions in the neighborhood of point A ($a_z = -0.23131$ and $q_z = 0.91919$). All nonzero superpositions were arbitrarily taken to be $\pm 10\%$, to exaggerate their influence. 71

Chapter 1
Introduction

Paul trap mass spectrometers are versatile analytical instruments which carry out fragment analysis of unknown compounds to elucidate their composition and structure. This instrument relies on trapping and storing ions in an oscillatory electric field and, subsequently, mass selectively destabilizing the ions to provide the mass spectrum of the unknown analyte. The Paul trap is one amongst a broad class of instruments referred to as ion traps that are used by researchers for trapping and storing ions. For this invention, Wolfgang Paul[1] shared half the 1989 Nobel prize for physics with Hans G. Dehmelt (who received the prize for the Penning trap technique).

The Paul trap mass spectrometer consists of a three-electrode geometry mass analyzer (March and Hughes, 1989), with two end cap electrodes and a central ring electrode, all electrodes machined to have hyperboloid geometry. Ion confinement is achieved within the central cavity by application of dc/rf or rf only potential(s) across the ring and the (electrically shorted) end cap electrodes. In an ideal machine, the trapping field is designed to be linear and the equations of motion of ions in the axial and radial directions are represented by two uncoupled Mathieu equations.

In practical traps, however, geometric misalignment and experimental constraints introduces weak multipole superpositions in the field. Although the contributions of the superpositions are small, they are known to have important consequences on trap operations. Some of these include alterations in the stability diagram in non linear Paul traps (Fischer, 1959; Dawson, 1976; Fulford et al., 1980), mass shifts (Cox et al. (1995)), perturbation in secular frequencies (Sugiyama and Yoda, 1990, Luo et al., 1996), coupled secular oscillations and nonlinear resonances (Vedel, 1990, Wang et al., 1993, Alheit et al., 1995, Chu et al., 1998), and altered resolution in mass spectra in forward and reverse scan resonance ejection experiments (Williams et al., 1994).

In spite of a large number of experimental studies reported in the literature that have linked field inhomogeneity to altered ion dynamics, the number of analytical studies to understand their role are relatively few. A reason for this is that in practical traps the equations of motions of ions are nonlinear and do not have closed form solutions. Consequently, researchers have relied primarily on numerical simulations to probe trapped ion dynamics. While such simulations provide useful insights, it would be more satisfactory

[1]The other half of the prize was awarded to Norman F. Ramsey for his work on atomic clocks.

academically and practically to have analytical expressions which describe ion dynamics in these weakly nonlinear fields. The present thesis is an attempt in this direction.

All chapters in this thesis have been written in a stand-alone form. Consequently all relevant literature, theory and methodology, for each problem are discussed in the relevant chapters. In this chapter we present a few background details for completeness of this thesis. We begin with a description of the Paul trap mass spectrometer. We next present the Mathieu equation which describes the motion of ions in an *ideal* Paul trap and this is followed by the description of the methods used for computing ion *secular* frequencies. Following this, we present the nonlinear Mathieu equation and the Duffing equation which are used in our studies. A brief description of two modes of operation of the Paul trap which are investigated in this thesis follows. Finally, the last section of this chapter presents the scope of this thesis.

1.1 The Paul trap mass spectrometer

The three electrodes of a Paul trap mass spectrometer (Paul and Steinwedel, 1953, 1960; Dawson and Whetten, 1968a, 1968b) have hyperboloid geometry and the electrode sur-

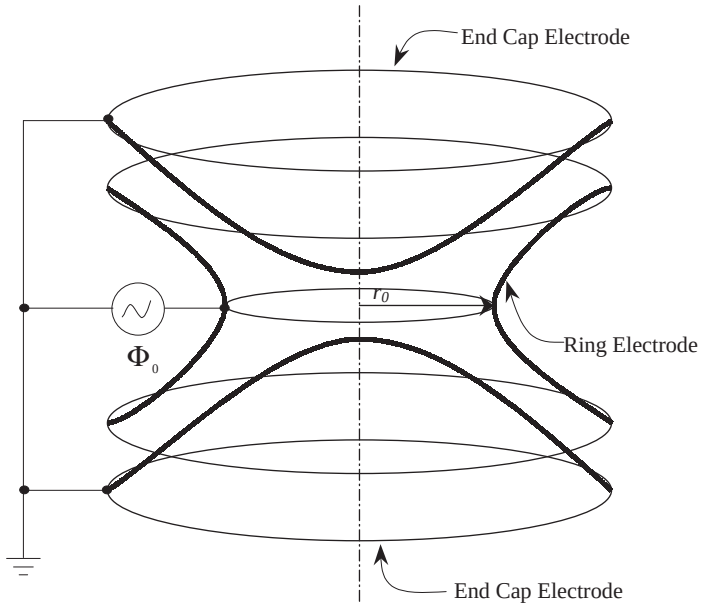

Figure 1.1: Paul trap mass analyzer

faces (r, z) are described by the expressions (Knight, 1983)

$$\begin{aligned} \frac{r^2}{r_0^2} - \frac{2z^2}{r_0^2} &= 1 \,(\text{ring electrode}) \\ \frac{r^2}{2z_0^2} - \frac{z^2}{z_0^2} &= -1 \,(\text{end cap electrode}) \end{aligned} \tag{1.1}$$

where r_0 is the radius of the ring electrode and z_0 is half the distance between the two end cap electrodes.

The electrodes of the mass analyzer are isolated electrically and they are mechanically mounted on a flange for easy insertion into a vacuum chamber. One of the end cap electrodes houses an electron gun (consisting of a tungsten or rhenium filament and associated extraction and gating electrodes) and has, typically, a 1 mm hole at its tip to permit entry of electrons. The tip of the other end cap electrode either has a larger hole which is covered by a fine stainless steel mesh or it may have multiple small holes for collection of the destabilized ions on to an electron multiplier.

The entire mass analyzer assembly is inserted into a vacuum chamber and trap operation is carried out in high vacuum conditions. Trap operation, which involves gating electrons for ionization of the analyte gas, cooling of ions and finally detection of the destabilized ions, is controlled by a personal computer. Each scan of an experiment takes place over a few tens of milliseconds of time and several such scans are averaged to obtain the mass spectrum of the analyte compound. In Paul trap mass spectrometers, helium is often used as a bath gas at a pressure slightly above the background low-pressure, to provide damping of ion motion during the cooling time.

A detailed description of the Paul trap mass spectrometer and its operation is available in March and Hughes (1989).

1.2 Motion of ions in a Paul trap

1.2.1 The Mathieu equation

The equation of motion of an ion of mass m under the influence of an electric potential is given by (Landau and Lifshitz, 1976)

$$\frac{d^2u}{dt^2} = -\frac{e}{m}\nabla_u\phi \tag{1.2}$$

where u corresponds to the axial (z) or radial (r) direction of motion and e/m corresponds to the charge to mass ratio. In an ideal trap, the potential ϕ at any point within the field

may be expressed in cylindrical co-ordinates as (March and Hughes, 1989)

$$\phi(r,z) = \frac{\phi_0}{r_0^2}(r^2 - 2z^2) \tag{1.3}$$

where ϕ_0 is the applied potential which is a combination of a dc and rf potential, given by

$$\phi_0 = U + V\cos\Omega t \tag{1.4}$$

where Ω ($= 2\pi f$, where f is the frequency in Hz) and V are the angular frequency and zero-to-peak amplitude of the rf potential, respectively, and U is the dc voltage. Inserting Eqs. (1.3) and (1.4) into Eq. (1.2), we obtain

$$\frac{d^2u}{dt^2} = -\frac{e}{m}(U + V\cos\Omega t)\frac{\partial}{\partial u}\left(\frac{1}{r_0^2}(z^2 - \frac{r^2}{2})\right) \tag{1.5}$$

which may be simplified to

$$\frac{d^2u}{dt^2} = -\frac{\kappa e u}{m r_0^2}(U + V\cos\Omega t) \tag{1.6}$$

where $\kappa = 2$ for the z-direction and $\kappa = -1$ for the r-direction. Further, nondimensionalizing time by defining $\tau = \Omega t/2$, we get

$$\frac{d^2u}{d\tau^2} + (a_u + 2q_u\cos 2\tau)u = 0 \tag{1.7}$$

where

$$a_z = -2a_r = \frac{8eU}{mr_0^2\Omega^2};\quad q_z = -2q_r = \frac{4eV}{mr_0^2\Omega^2} \tag{1.8}$$

Equation (1.7) is the canonical form of the Mathieu equation. Also, it may be readily observed from Eq. (1.8) that the Mathieu parameters a_u and q_u are related to experimental parameters U, V, r_0, Ω as well as the ion mass m. The Mathieu equation has a general solution of the form (McLachlan, 1947, 1958; Abromowitz and Stegun, 1970)

$$u = A_u\sum_{n=-\infty}^{\infty} C_{2n,u}\cos(\beta_u + 2n)\tau + B_u\sum_{n=-\infty}^{\infty} C_{2n,u}\sin(\beta_u + 2n)\tau \tag{1.9}$$

where $C_{2n,u}$ are the amplitudes of the various harmonics, A_u and B_u are arbitrary constants and β_u is a parameter with values between 0 and 1.

1.2.2 Mathieu stability plot

In the ideal trap the equation of motion (Eq. (1.7)) in the radial and axial directions are uncoupled and stability of ions within the trap cavity can be evaluated independently in

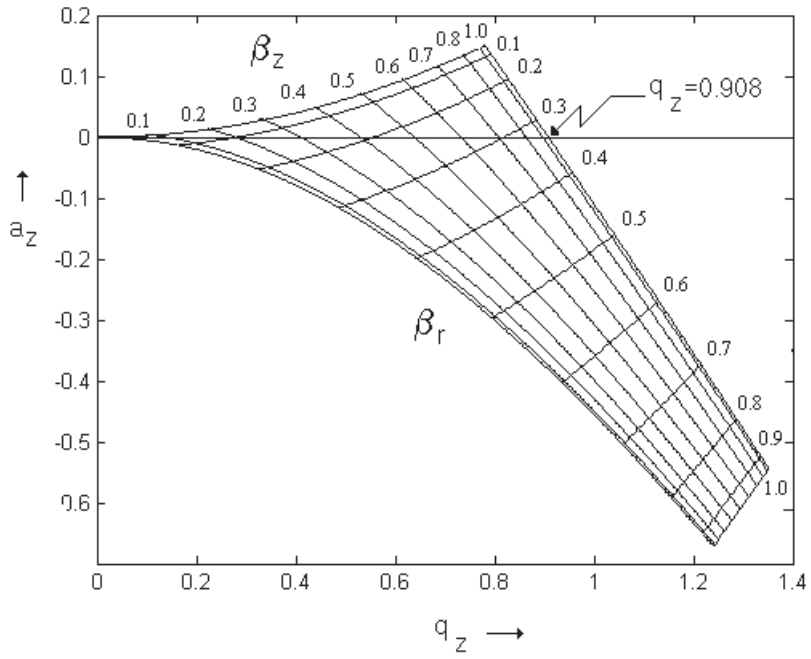

Figure 1.2: Mathieu stability plot

these two directions. Ions will be trapped within the cavity of the mass analyzer only when their motion is simultaneously stable in the radial and axial directions. The Mathieu stability plot provided in Fig. 1.2 shows region in the a_z-q_z plane where the ion motion is simultaneously stable in r and z directions (Dawson, 1976; March and Todd, 1995). For a given mass analyzer the radius of the central ring electrode and the angular frequency of the rf drive are fixed. Consequently, the stability of ions of mass m will be determined only by the dc (U) and rf (V) potential applied to the electrodes.

1.2.3 Secular frequency

From Eq. (1.9) the angular frequency of ion motion of order n is given by

$$\omega_{u,n} = (n + \frac{1}{2}\beta_u)\Omega \tag{1.10}$$

$\omega_{u,n}$ is referred to as the *secular* frequency of the ion of order n. When $n = 0$, the secular frequency of the ion, ω_u, in either r or z direction, in the stable region closest to the origin of the Mathieu stability plot, is given by

$$\omega_u = \frac{1}{2}\beta_u\Omega. \tag{1.11}$$

β_u is a parameter which is related to the Mathieu parameters a_u and q_u by the continuous fraction relation (March and Hughes, 1989) which has the form

$$\begin{aligned}\beta_u^2 &= a_u + \cfrac{q_u^2}{(\beta_u+2)^2 - a_u - \cfrac{q_u^2}{(\beta_u+4)^2 - a_u - \cfrac{q_u^2}{(\beta_u+6)^2 - a_u - \ldots}}} \\ &\quad + \cfrac{q_u^2}{(\beta_u-2)^2 - a_u - \cfrac{q_u^2}{(\beta_u-4)^2 - a_u - \cfrac{q_u^2}{(\beta_u-6)^2 - a_u - \ldots}}}.\end{aligned} \tag{1.12}$$

Within the pseudopotential well approximation region which is valid up to $q_z < 0.4$, β_u can be approximated as (as will be seen later in Eq. (1.33)) by the expression

$$\beta_u^2 = a_u + \frac{q_u^2}{2}. \tag{1.13}$$

Equation (1.13) is referred to as adiabatic or Dehmelt approximation in mass spectrometry literature.

It needs to be pointed out that since β_u is related to a_u and q_u, for a given trap (with fixed r_0 and Ω), β_u for a given mass m is determined only by the dc and rf potentials applied to the electrodes.

1.2.4 Nonlinear Mathieu equation

The field within a practical Paul trap is weakly nonlinear on account of geometric misalignments and experimental constraints. The presence of asymmetric holes in the two end cap electrodes (March and Hughes, 1989), misalignments in geometry (Louris et al., 1992), space charge due to trapped ions (Cox et al., 1996), truncation of electrodes to finite size, and stretched geometry will introduce higher order multipole contributions to the potential in an experimental trap (Franzen et al., 1995).

The potential within a nonlinear Paul trap is modelled using Legendre polynomials (Brown and Gabrielse, 1986; Beaty, 1986). If P_n is the Legendre polynomial of order n, then the potential distribution inside the trap in terms of spherical coordinates is given by

$$\phi(\rho,\theta,\varphi) = \phi_0 \sum_{n=0}^{\infty} A_n \frac{\rho^n}{r_0^n} P_n(\cos\theta) \tag{1.14}$$

where A_n is the dimensionless weight factors for different multipole terms, ρ is the position vector.

In the studies presented in this thesis, we consider higher order multipoles hexapole, octopole, decapole and dodecapole superpositions corresponding to $n = 3$, 4, 5 and 6 in Eq. (1.14), respectively, along with the quadrupole ($n = 2$). The corresponding Legendre polynomials in cylindrical coordinates can be written as (Beaty, 1986)

$$\text{quadrupole:} \quad P_2(\cos\theta) = \frac{(2z^2 - r^2)}{2\rho^2} \tag{1.15}$$

$$\text{hexapole:} \quad P_3(\cos\theta) = \frac{(2z^3 - 3zr^2)}{2\rho^3} \tag{1.16}$$

$$\text{octopole:} \quad P_4(\cos\theta) = \frac{(8z^4 - 24z^2r^2 + 3r^4)}{8\rho^4} \tag{1.17}$$

$$\text{decapole:} \quad P_5(\cos\theta) = \frac{(8z^5 - 40z^3r^2 + 15zr^4)}{8\rho^5} \tag{1.18}$$

$$\text{dodecapole:} \quad P_6(\cos\theta) = \frac{(16z^6 - 120z^4r^2 + 90z^2r^2 - 5r^6)}{16\rho^6} \tag{1.19}$$

where $\rho^2 = z^2 + r^2$.

Substituting Eq. (1.4) and Eqs. (1.16) through (1.19) into Eq. (1.14), we get the potential in cylindrical co-ordinates as

$$\begin{aligned}\Phi(r,z,t) &= (U + V\cos\Omega t)\left[\frac{A_2}{r_0^2}\left(z^2 - \frac{r^2}{2}\right) + \frac{A_3}{r_0^3}\left(z^3 - \frac{3}{2}zr^2\right) + \frac{A_4}{r_0^4}\left(z^4 - 3z^2r^2 + \frac{3}{8}r^4\right) + \right. \\ &\left. \frac{A_5}{r_0^5}\left(z^5 - 5z^3r^2 + \frac{15}{8}zr^4\right) + \frac{A_6}{r_0^6}\left(z^6 - \frac{15}{2}z^4r^2 + \frac{45}{8}z^2r^4 - \frac{5}{16}r^6\right)\right] \end{aligned} \tag{1.20}$$

where A_2, A_3, A_4, A_5 and A_6 are the weights of the quadrupole, hexapole, octopole, decapole and dodecapole superpositions, respectively. Substituting Equation (1.20) into Equation (1.2), and introducing the transformations $\tau = \Omega t/2$, $\bar{r} = r/r_0$ and $\bar{z} = z/r_0$, the equation of motion of ion in the z-direction can be derived in the form of a nonlinear Mathieu equation as (Sevugarajan and Menon, 2002; Abraham et al., 2003)

$$\begin{aligned}\frac{d^2\bar{z}}{d\tau^2} + (a_z + 2q_z\cos 2\tau)\left[\bar{z} + \frac{3}{2}h\left(\bar{z}^2 - \frac{1}{2}\bar{r}^2\right) + 2f\left(\bar{z}^3 - \frac{3}{2}\bar{z}\bar{r}^2\right) + \right. \\ \left. \frac{5}{2}d\left(\bar{z}^4 - 3\bar{z}^2\bar{r}^2 + \frac{3}{8}\bar{r}^4\right) + 3k\left(\bar{z}^5 - 5\bar{z}^3\bar{r}^2 + \frac{15}{8}\bar{z}\bar{r}^4\right)\right] = 0 \end{aligned} \tag{1.21}$$

where $h = A_3/A_2$, $f = A_4/A_2$, $d = A_5/A_2$ and $k = A_6/A_2$ represent the ratio of the weights of the hexapole, octopole, decapole and dodecapole superpositions with respect to the weight of the quadrupole contribution and

$$a_z = \frac{8eA_2U}{mr_0^2\Omega^2} \tag{1.22}$$

$$q_z = \frac{4eA_2V}{mr_0^2\Omega^2}. \tag{1.23}$$

Similarly, the equation of motion of ion in the r-direction can be derived as

$$\frac{d^2\bar{r}}{d\tau^2} + (a_r + 2q_r\cos 2\tau)\left[\bar{r} + 3h\bar{z}\bar{r} + 3f\left(2\bar{z}^2\bar{r} - \frac{1}{2}\bar{r}^3\right) + 5d\left(2\bar{z}^3\bar{r} - \frac{3}{2}\bar{z}\bar{r}^3\right) + 15k\left(\bar{z}^4\bar{r} - \frac{3}{2}5\bar{z}^2\bar{r}^3 + \frac{3}{8}\bar{r}^5\right)\right] = 0 \tag{1.24}$$

where

$$a_r = -\frac{4eA_2U}{mr_0^2\Omega^2} \tag{1.25}$$

$$q_r = -\frac{2eA_2V}{mr_0^2\Omega^2}. \tag{1.26}$$

1.2.5 Forced, damped Duffing equation

In nonlinear traps with only octopole superposition, the uncoupled equation of motion of an ion in the axial (z) direction is a nonlinear Mathieu equation with only cubic nonlinearity and can be obtained by putting r, h, d, k to zero in Eq. (1.21). The equation of motion takes the form

$$\frac{d^2\bar{z}}{d\tau^2} + (a_z + 2q_z\cos 2\tau)\left(\bar{z} + 2f\bar{z}^3\right) = 0. \tag{1.27}$$

In order to obtain the equation of motion of ion in a nonlinear trap in the presence of dipolar excitation (excitation potential applied across the end cap electrodes), within the pseudopotential well approximation region (Landau and Lifshitz, 1976), we consider ion motion in spherical co-ordinates as

$$m\frac{d^2\rho}{dt^2} + e\nabla U_{eff}(r,z) = -e\nabla U_{exc} \tag{1.28}$$

where ρ is the position vector and

$$U_{exc} = A_1V_s\sin(\omega t)(\frac{z}{r_0}) \tag{1.29}$$

where A_1 is the weight of the dipole superposition (Beaty, 1986), V_s and ω are the zero-to-peak amplitude and the angular frequency, respectively, of the auxiliary ac excitation signal applied to the end caps and

$$U_{eff}(r,z) = \frac{1}{2}\frac{e}{m}\left\langle |\int_t \nabla\Phi dt|^2\right\rangle. \tag{1.30}$$

In the presence of only octopole superposition, U_{eff} can be evaluated from Eq. (1.20) as (Sevugarajan and Menon, 1999)

$$U_{eff}(r,z) = \frac{q_z^2\Omega^2 m}{64e}(4z^2 + \frac{16f}{r_0^2}z^4). \tag{1.31}$$

Substituting Equations (1.29) and (1.31) into Equation (1.28) and introducing damping (caused by presence of He buffer gas), we get the equation for ion motion in the axial direction in the form of a damped, forced Duffing equation as

$$\frac{d^2z}{dt^2} + c\frac{dz}{dt} + \omega_{0z}^2 z + \frac{8f}{r_0^2}\omega_{0z}^2 z^3 = -F_s\cos\omega t \tag{1.32}$$

where ω_{0z} is the secular frequency of ion motion and F_s, the amplitude of the force term, are given by

$$\omega_{0z} = (a_z + \frac{q_z^2}{2})\frac{\Omega^2}{4} \tag{1.33}$$

and

$$F_s = \frac{eA_1V_s}{mr_0}. \tag{1.34}$$

The damping coefficient, c, in Eq. (1.32) is given by (Goeringer et al., 1992)

$$c = \frac{m_n}{m+m_n}\frac{p}{kT_b}\frac{e}{2\varepsilon_0}\sqrt{\alpha\frac{m+m_n}{mm_n}} \tag{1.35}$$

where m_n is the mass of the bath gas, $\alpha = 0.22 \times 10^{-40}$ Fm^2 is the polarizability of the bath gas, $\varepsilon_0 = 8.854 \times 10^{-12}$ F/m is the permittivity of the free space, T_b is the temperature and p is the pressure in Pascal of the bath gas.

1.3 Modes of operation

In this thesis we consider two modes of operation of the Paul trap which are briefly described below.

1.3.1 Mass selective boundary ejection

In the mass selective boundary ejection experiments (Stafford et al., 1984) the end cap electrodes are grounded and dc potential is set to zero. Ion destabilization is made to occur at the boundary of the Mathieu stability plot (along $a_z = 0$ axis) at $q_z = 0.908$ (Fig. 2). At the start of the experiment, ions of an analyte gas are formed *in situ* within the trap cavity by a gated beam of electrons. At the time of ion formation an initial rf potential is applied between the ring and end cap electrodes. Within this trapping field,

ions of different masses will be trapped with different q_z values, the lowest mass having the largest q_z and all higher masses having progressively lower q_z values.

In the experiment, the amplitude of the rf potential is increased (generally) linearly at a predetermined rate (in commercial instruments this is of the order of 1 Th per 180 μsec, 1 Thomson (Th) = 1 u/e, where u is the atomic mass unit and e is the elementary charge (Cooks and Rockwood, 1991)) resulting in the q_z values of ions of all masses progressively increasing. When the q_z value of an ion of specific mass crosses $q_z = 0.908$ (corresponding to $\beta_z = 1$ boundary on the Mathieu stability plot), they get destabilized from the trap and, those ions exiting the trap through the end cap electrodes which houses the electron multiplier, will be detected and its intensity recorded. The ion intensity versus rf potential histogram provides the mass spectrum of the analyte gas.

1.3.2 Resonance excitation

The other mode of operation which has been investigated in this thesis is referred to as resonance ejection (Fulford and March 1978; March, 1992). Here, a dipolar auxiliary excitation, having a fixed frequency, is applied across the end cap electrodes (as shown in Figure 1.3). This arrangement is different from the configuration in mass selective boundary ejection experiments in which the two end caps electrodes are grounded. In these experiments the property of the resonance of ion secular frequency with the dipolar auxiliary excitation frequency is used to cause destabilization of ions from the trap.

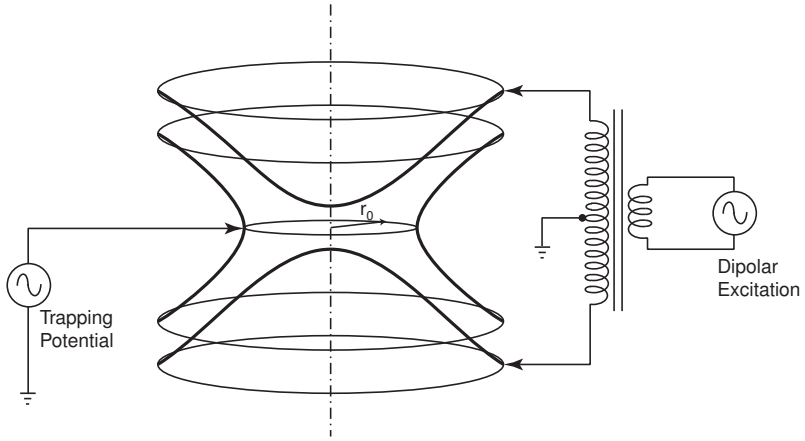

Figure 1.3: Experimental set up for resonance ejection experiment

Like the mass selective instability experiment described earlier, here too a gated beam of electrons is used to cause ionization of the analyte gas within a trapping field created by an initial rf potential applied between the ring and the end cap electrodes. In these experiments also, dc voltage is set to zero and trap operation is carried out along the

$a_z = 0$ axis of the Mathieu stability plot. Ions of each mass which are trapped at different q_z value, oscillate at their secular frequency which is determined by the initial rf potential (since rf potential determines the ion's q_z which in turn determines the secular frequency, as seen in Section 1.2.3). In these experiments the motivation is to bring axial secular frequency into resonance with the auxiliary excitation.

Resonance can be brought about in one of two ways which depends on the relative magnitudes of ion axial secular frequency and the frequency of the applied auxiliary excitation. When ion secular frequency is smaller than the dipolar excitation frequency at the start of the experiment, the amplitude of the rf potential is increased to cause an increase in q_z which in turn causes ion secular frequency of a specific mass to increase. Experiments involving an increase in amplitude of rf potential (which results in an increase in ion secular frequency) is referred to as the *forward* scan experiment. Conversely, if the ion secular frequency is larger than the frequency of the dipolar excitation at the start of the experiment, the amplitude of the rf potential is ramped down. This experiment is referred to as the *reverse* scan experiment. In resonance ejection experiments too, the ion intensity versus rf potential histogram provides the mass spectrum of the analyte compound.

1.4 Scope of the thesis

Analytical studies of three experimental observations in practical Paul traps have been carried out in this thesis. The first is a study to understand the role of field inhomogeneities in influencing early/delayed ejection at the stability boundary. The other two studies are related to resonances experienced by ions in nonlinear fields in practical traps.

Specifically, the three problems taken up for study include:

1. A study to understand the role of field inhomogeneities in causing early/delayed ejection in practical Paul traps operated in the mass selective ejection mode. Here the governing equation is an uncoupled nonlinear Mathieu equation in which terms corresponding to hexapole, octopole, decapole and dodecapole superpositions have been included.

2. A study of the altered resolution observed in resonance ejection experiments in the forward and reverse scan directions. In this study we will include only octopole field superposition in the governing equation. The equation of motion in this study will be a damped forced Duffing oscillator which has validity in the Dehmelt approximation regime.

3. The final problem is concerned with coupled resonances which have been reported in practical Paul traps. In this study we will use the coupled nonlinear Mathieu equations with multipole superpositions up to dodecapole to first identify and subsequently select

a specific coupled resonance point within the Mathieu stability plot for further detailed investigation.

Investigation of early/delayed ejection of ions (Chapter 2) was a collaborative effort with Mr. Amol Marathe, Research Scholar, Department of Mechanical Engineering, Indian Institute of Science, Bangalore. His important contribution lies in the development of the slow flow equations which have been used in this study. At the time of writing this thesis two investigations, reported in Chapters 2 and 3, have been accepted for publication in International Journal of Mass Spectrometry.

References in the text have been given by quoting author name and year of publication. Full references have been listed in alphabetical order at the end of the thesis.

Chapter 2

Multiple scales analysis of early and delayed boundary ejection in Paul traps

2.1 Introduction

In this chapter we study dynamics associated with early and delayed ejection observed in Paul traps operated in mass selective ejection mode. In particular, we study differences in the dynamics arising from higher order field superpositions of small magnitudes. The method of multiple scales is used to derive an approximate analytical expression which captures the slow variation in the amplitude of ion motion near the stability boundary.

Paul trap mass spectrometers consist of a three electrode mass analyzer with two end cap electrodes and a central ring electrode, all having hyperboloid geometry (Dawson, 1976; Knight, 1983). Ions of analyte gas, formed *in situ* by electron impact ionization, are trapped within the cavity by a trapping field formed by dc and rf potentials applied between the ring and end cap electrodes (Dawson, 1976; March and Hughes, 1989). The motion of ions within an *ideal* trap is governed by two uncoupled, linear Mathieu equations (Dawson, 1976; McLachlan, 1947) given by

$$\frac{d^2u}{d\tau^2} + (a_u + 2q_u \cos 2\tau)u = 0, \tag{2.1}$$

where u represents either the r (radial) or z (axial) direction of motion, $\tau = \Omega t/2$, where in turn Ω is the angular frequency of the rf drive applied to the central ring electrode, and t is time. In Eq. (2.1), a_u and q_u are Mathieu parameters which determine ion stability within the trap.

In mass selective ejection experiments, the trap is operated along the $a_z = 0$ axis (by setting the dc potential to zero) (Stafford et al., 1984) of the Mathieu stability plot (March and Hughes, 1989) and ions are destabilized from the trap by ramping the rf amplitude to cause the ion's q_z value to cross the stability boundary at or near $q_z^* = 0.908046$. In practical traps it is known that small field inhomogeneities, which arise due to geometric imperfections and experimental constraints, cause ions to get ejected at smaller or larger q_z values (compared to $q_z^* = 0.908046$) resulting in the observation of early or delayed ejection, respectively. On account of this, it was observed very early during commercialization of the Paul trap mass spectrometer that traps were prone to errors in mass assignments (Syka et al., 1995), a problem that was subsequently overcome

by increasing the distance between the two end cap electrodes. Wells et al. (1999) showed that these mass shifts arise on account of the interplay of two primary factors which include (1) presence of nonlinear fields (caused by holes in the end caps as well as truncation of the electrodes) within the trap cavity which tends to delay ion ejection and (2) elastic and inelastic collisions of the ions with the bath gas which tend to shorten this delay. A recent report by Plass et al. (2003) has provided further understanding on mass shifts through a study of its dependence on trap geometry, buffer gas, rf amplitude scan rate, ion mass and the chemical structure of the ion. In the context of the influence of field inhomogeneities causing delayed ion ejection Franzen and coworkers (Wang and Franzen, 1994; Franzen, 1993; Wang et al., 1993; Franzen, 1994), in a series of numerical studies, showed that positive octopole and dodecapole superpositions cause ions to come out early (at $q_z < q_z^*$) and the presence of negative octopole and dodecapole superpositions or hexapole and decapole superpositions of either sign cause delayed ejection of ions (at $q_z > q_z^*$).

Understanding the dynamics associated with early and delayed ejection caused by field nonlinearities (inhomogeneities) is important in the context of newer trap geometries being investigated for their use as mass spectrometers. The 2D (linear) Paul trap, which consists of a four-rod assembly mass analyzer, has been used in both mass selective instability mode (Schwartz et al., 2002) as well as for resonance excitation experiments (Collings et al., 2003). Modified geometries of 2D Paul traps with added octopole fields have also been investigated by Michaud et al. (2004) and Collings (2005). Another direction of investigation concerns traps that have greatly simplified geometries compared to the hyperboloid geometry of the 3D Paul trap. An example of this is the cylindrical trap (Lanmuir et al., 1962; Bonner et al., 1977) which consists of a cylindrical ring electrode and two flat end cap electrodes, and has scope for MEMS scale fabrication (Blain et al., 2004; Austin et al., 2006). Currently these instruments are being used as fieldable instruments (Wu et al., 2005) but we hope that better appreciation of the effects of multipole superpositions on boundary ejection of ions will help in developing miniaturized mass analyzers even for high performance applications. The common feature for all these mass analyzers is that the governing equations of ion motion within the trap cavity are Mathieu equations. Further, in these traps, on account of non-ideal geometries and experimental constraints, higher order multipole fields get superposed on the predominantly linear field. This results in the equations of motion taking the form of (weakly) nonlinear and coupled Mathieu equations. In this chapter, however, we consider a single, weakly nonlinear Mathieu equation.

The main problem in studying ion behavior in the neighborhood of the Mathieu stability boundary is that it is not possible to derive a closed form solution for ion motion when field inhomogeneities are present. Sudakov (2001) has presented an insightful analysis of the slow variation in amplitude of the ion motion, which he calls the "beat" envelope, near

the stability boundary. He showed that in case of positive octopole superposition, there exists an effective potential well in the stable region. The width and depth of this well decreases as q_z approaches the stability boundary. In case of negative octopole superposition and hexapole superposition of either sign, the existence of a double well potential in the unstable region of the Mathieu stability plot causes delayed ejection of ions from the trap.

In this chapter we present a detailed and systematic analytical study of ion ejection near the nominal stability boundary ($q_z^* = 0.908046$) for practical Paul traps. We go beyond the work of Sudakov (2001) in three ways. First, we adopt a formal perturbation method, the method of multiple scales (MMS), which has enabled us to proceed up to the fourth order (Section 2.6.1). This may be useful when the weights of multipole superpositions are relatively larger. However, we use only the second order slow flow for obtaining the phase portraits in this chapter, since we have assumed weak multipole superpositions. Secondly, we have incorporated higher order multipoles (hexapole, octopole, decapole and dodecapole superpositions) in the governing equation. With this, we obtain new insights into the dynamics associated with these multipole superpositions within the trapping field. Finally, we use phase portraits to provide an alternative view of the slow modulation dynamics as the ions approach the stability boundary, to understand early and delayed ejection of ions. Our results match Sudakov (2001) up to second order, except for an apparent error in one of his terms, which we have corrected.

As a technical matter, we mention that the application of the MMS at the stability boundary involves somewhat greater complications than the application of the MMS, or the related method of averaging (Abraham and Chatterjee, 2003), to resonant points inside the nominal stability region because in the latter case the unperturbed equation has two linearly independent periodic solutions.

2.2 Equation of motion

In the literature, the potential distribution inside a trap with field inhomogeneities in terms of spherical coordinates (ρ, θ, φ) is given by (Beaty, 1986)

$$\phi(\rho, \theta, \varphi) = \phi_0 \sum_{n=0}^{\infty} A_n \frac{\rho^n}{r_0^n} P_n(\cos\theta), \tag{2.2}$$

where P_n is the Legendre polynomial of order n, A_n is the dimensionless weight factor for the n^{th} multipole term, ρ is the radial position and r_0 is chosen to be the radius of the central ring electrode in our study. ϕ_0 is given by

$$\phi_0 = U + V\cos\Omega t, \tag{2.3}$$

where U is the applied dc potential, and V is the amplitude of the applied rf potential. In this study we consider four higher order multipoles which include A_3, A_4, A_5 and A_6, corresponding to hexapole, octopole, decapole and dodecapole, respectively, in Eq. (2.2). We use the notation and sign convention of Beaty (1986) for representing the higher order multipoles. Since our focus is on axial (z) instability, we set $r \equiv 0$. Following the procedure adopted by Sevugarajan and Menon (2002) and Abraham et al. (2004), the uncoupled equation of motion of trapped ions in the axial (z) direction in an experimental trap reduces to a nonlinear Mathieu equation,

$$\frac{d^2\bar{z}}{d\tau^2} + (a_z + 2q_z \cos 2\tau)\left(\bar{z} + \frac{3h}{2}\bar{z}^2 + 2f\bar{z}^3 + \frac{5d}{2}\,\bar{z}^4 + 3k\,\bar{z}^5\right) = 0, \tag{2.4}$$

where $\bar{z} = z/r_0$ is the axial position of the ion normalized with respect to r_0, $\tau = \Omega t/2$, and $h(= A_3/A_2)$, $f(= A_4/A_2)$, $d(= A_5/A_2)$ and $k(= A_6/A_2)$ are the proportion of hexapole, octopole, decapole and dodecapole nonlinearity, respectively, to the quadrupole superposition, A_2. Also, a_z and q_z are Mathieu parameters for the nonlinear trap and are given by

$$a_z = \frac{8eA_2U}{mr_0^2\Omega^2}; \quad q_z = \frac{4eA_2V}{mr_0^2\Omega^2}, \tag{2.5}$$

where e/m is the charge to mass ratio of the ion.

A point that needs mention is related to the usage of the descriptors "positive" and "negative" for multipole superpositions. In the mass spectrometry literature, the sign is implicitly attributed to the specific multipole by assuming that the sign of the quadrupole superposition is positive. In actual practice, when the end cap electrodes of the ion trap are grounded as is usually done in mass selective boundary ejection experiments, the weight of the quadrupole superposition, A_2 is negative. Consequently, "positive" multipole superposition implies that A_n and A_2 have the *same* sign and "negative" multipole superposition implies A_n and A_2 have *opposite* signs.

In mass selective ejection experiments, where only the rf voltage is applied, the equation of motion (Eq. (2.4)) takes the form

$$\frac{d^2\bar{z}}{d\tau^2} + 2q_z \cos 2\tau\left(\bar{z} + \frac{3h}{2}\bar{z}^2 + 2f\bar{z}^3 + \frac{5d}{2}\,\bar{z}^4 + 3k\,\bar{z}^5\right) = 0, \tag{2.6}$$

since a_z is set to zero. Ion destabilization occurs at the stability boundary (corresponding to $\beta_z = 1$, where β_z is related to the Mathieu parameters a_z and q_z) in the Mathieu stability plot (March and Londry, 1995). In our discussion the q_z value at the nominal point of destabilization in *ideal* traps will be referred to as q_z^*, which happens to be 0.908046, as shown below.

In the method of multiple scales adopted here, we need to order the nonlinearities.

The following ordering scheme has been adopted,

$$h = \frac{2\sqrt{\epsilon}\,\bar{h}}{3}\,, \quad f = \frac{\epsilon \bar{f}}{2}, \quad d = \frac{2\sqrt{\epsilon}\,\bar{d}}{5}, \quad k = \frac{\epsilon \bar{k}}{3}, \tag{2.7}$$

where $\bar{h}$, $\bar{f}$, $\bar{d}$, $\bar{k}$ and ϵ will determine the strengths of the nonlinearities. Note that all even superpositions have been ordered as ϵ and odd superpositions as $\sqrt{\epsilon}$. Moreover, $\bar{h}$, $\bar{f}$, $\bar{d}$ and $\bar{k}$ are of $\mathcal{O}(1)$, with the "smallness" of these terms governed by $0 < \epsilon \ll 1$. Further, to study the dynamics near q_z^*, we introduce a detuning parameter Δ and write

$$q_z = q_z^* + \epsilon\Delta. \tag{2.8}$$

Thus by assigning negative and positive values to Δ, we can study the dynamics associated with early and delayed ejection, respectively.

Substituting Eqs. (2.7) and (2.8) into Eq. (2.6), the governing equation of our system takes the form

$$\frac{d^2\bar{z}}{d\tau^2} + 2(q_z^* + \epsilon\Delta)\cos 2\tau\left(\bar{z} + \sqrt{\epsilon}\,\bar{h}\bar{z}^2 + \epsilon\bar{f}\bar{z}^3 + \sqrt{\epsilon}\,\bar{d}\bar{z}^4 + \epsilon\bar{k}\bar{z}^5\right) = 0. \tag{2.9}$$

2.3 Analysis using multiple scales

In the method of multiple scales (Nayfeh, 1973; Hinch, 1991; Kevorkian and Cole, 1996), we assume that the solution to the original equation can be represented as a function of multiple time scales. Here, we choose $T_0 = \tau$, $T_1 = \sqrt{\epsilon}\tau$, $T_2 = \epsilon\tau$, $\cdots$. T_0 is the fast (usual) time and T_1, T_2, $\cdots$ are the *slow* times. This particular choice is justified in Section 2.6.2. The solution $\bar{z}(\tau)$ to Eq. (2.9) is sought in the form

$$\bar{z}(\tau) = X(T_0, T_1, T_2, \cdots). \tag{2.10}$$

Further, X is expanded as

$$\begin{aligned} X(T_0, T_1, T_2, \cdots) \;=\; & X_0(T_0, T_1, T_2, \cdots) + \sqrt{\epsilon}\,X_1(T_0, T_1, T_2, \cdots) \\ & + \epsilon\,X_2(T_0, T_1, T_2, \cdots) + \epsilon\sqrt{\epsilon}\,X_3(T_0, T_1, T_2, \cdots) + \mathcal{O}(\epsilon^2). \end{aligned} \tag{2.11}$$

The derivatives with respect to τ are

$$\frac{d(.)}{d\tau} = \frac{\partial(.)}{\partial T_0} + \sqrt{\epsilon}\frac{\partial(.)}{\partial T_1} + \epsilon\frac{\partial(.)}{\partial T_2} + \mathcal{O}(\epsilon\sqrt{\epsilon}), \tag{2.12}$$

$$\frac{d^2(.)}{d\tau^2} = \frac{\partial^2(.)}{\partial T_0^2} + 2\sqrt{\epsilon}\frac{\partial^2(.)}{\partial T_0 \partial T_1} + \epsilon\left(\frac{\partial^2(.)}{\partial T_1^2} + 2\frac{\partial^2(.)}{\partial T_0 \partial T_2}\right) + \mathcal{O}(\epsilon\sqrt{\epsilon}). \tag{2.13}$$

Substituting Eqs. (2.11) through (3.18) in Eq. (2.9), expanding and collecting terms using a symbolic algebra package (MAPLE), we obtain

$$\begin{aligned}
&\frac{\partial^2 X_0}{\partial T_0^2} + 2q_z^* \cos(2T_0) X_0 \\
&+\sqrt{\epsilon}\left[\frac{\partial^2 X_1}{\partial T_0^2} + 2q_z^* \cos(2T_0)\left(X_1 + \bar{h}X_0^2 + \bar{d}X_0^4\right) + 2\frac{\partial^2 X_0}{\partial T_0 \partial T_1}\right] \\
&+\epsilon\left[\frac{\partial^2 X_2}{\partial T_0^2} + \frac{\partial^2 X_0}{\partial T_1^2} + 2\frac{\partial^2 X_0}{\partial T_0 \partial T_2} + 2\frac{\partial^2 X_1}{\partial T_0 \partial T_1} + 2\cos(2T_0)\left(q_z^* X_2\right.\right. \\
&\left.\left. +2q_z^* \bar{h} X_0 X_1 + q_z^* \bar{f} X_0^3 + 2q_z^* \bar{d} X_0^3 X_1 + q_z^* \bar{k} X_0^5 + \Delta X_0\right)\right] + \mathcal{O}(\epsilon\sqrt{\epsilon}) = 0. \qquad (2.14)
\end{aligned}$$

As is usual for the MMS, we will solve the above sequentially for different orders (powers of ϵ). Indeterminacy in the solution at each stage, as usual, will be eliminated by insisting on a bounded solution at the next stage (a process called removal of secular terms). However, the form of the secular terms, and our process of identifying them, is somewhat unusual and described in detail below. Note that, for our higher order calculations, we retained more terms in the above expansion, these are not presented here for the sake of brevity.

2.3.1 Solution at $\mathcal{O}(1)$

From Eq. (2.14) at $\mathcal{O}(1)$, we have the linear Mathieu equation

$$\frac{\partial^2 X_0}{\partial T_0^2} + 2\, q_z^* \cos(2T_0) X_0 = 0. \qquad (2.15)$$

Since this equation corresponds to the ion motion at the boundary ($q_z = q_z^*$), the solution consists of a 2π-periodic function and a linearly growing function (Stoker, 1950).

Let the periodic function be ξ_1. It can be written as a cosine series given by

$$\xi_1 = \sum_{k=0}^{M} a_k \cos\Big((2k+1)\, T_0\Big), \qquad (2.16)$$

where $M = \infty$ for the exact solution, but we will truncate the series at a suitably large value of M. In our computation, we set $M = 12$.

To obtain (or rather, verify) the numerical value of q_z^*, we substitute the truncated cosine series into Eq. (2.15). Collecting the coefficients of the harmonics retained in the approximation (Eq. (2.16)) and equating them to zero, we get $M + 1$ simultaneous linear equations in unknown a_k's. For nontrivial solutions to exist, the determinant of

the coefficient matrix, which is a polynomial in q_z^*, must be zero. When this equation is solved, the smallest root gives $q_z^* = 0.908046$. In what follows, we take[1] $q_z^* = 0.908046$.

In order to obtain the a_k's (and thus ξ_1), we substitute $q_z^* = 0.908046$ into the $M+1$ linear equations obtained earlier. Since the $M+1$ equations are linearly dependent, we choose $a_0 = 1$ for convenience, drop the equation corresponding to the coefficient of $\cos(T_0)$, and use the remaining M equations to find the remaining a_k's (see Table 2.1).

The linearly growing part of the solution of Eq. (2.15) has the form $\xi_2 + T_0\,\xi_1$ (Stoker, 1950), where ξ_2 is 2π-periodic. When this form is inserted into Eq. (2.15), we get the differential equation for ξ_2 as

$$\ddot{\xi}_2 + 2\,q_z^*\,\cos(2T_0)\,\xi_2 = -2\,\dot{\xi}_1. \tag{2.17}$$

ξ_2 can be approximated by a truncated Fourier series as

$$\xi_2 = \sum_{k=0}^{M} b_k \sin\Big((2k+1)\,T_0\Big), \tag{2.18}$$

where, again, we use $M = 12$. Substituting this into the differential equation for ξ_2 and collecting terms, we get $M+1$ linear simultaneous equations which can be directly solved to obtain the b_k's (Table 2.1). The a_k's and b_k's progressively decrease in magnitude and their numerical values for $k > 6$ are not presented here, although $M = 12$ and many digits of precision were used in our MAPLE calculation. It is clear that choosing $M = 12$ is more than enough for practical purposes.

The general solution to Eq. (2.15) can then be written as

$$X_0 = A(T_1, T_2)\,\xi_1(T_0) + B(T_1, T_2)\Big(\xi_2(T_0) + T_0\,\xi_1(T_0)\Big), \tag{2.19}$$

where A and B are arbitrary functions of T_1 and T_2.

We now set $B \equiv 0$ which eliminates the rapidly growing part in Eq. (2.19). This may initially seem somewhat arbitrary. Note, however, that by choosing $B \equiv 0$, we can obtain *one* solution and numerics will show that the solution so obtained is useful. For a similar example of setting the coefficient of a rapidly increasing term to zero and some relevant discussion, see Chatterjee and Chatterjee (2006). Thus the solution to the $\mathcal{O}(1)$ equation is taken as

$$X_0 = A(T_1, T_2)\,\xi_1(T_0). \tag{2.20}$$

It may be noted that ξ_2 does not appear in X_0 in Eq. (2.20). However, ξ_2 will be required in the subsequent analysis.

[1] More digits were retained in our calculations using MAPLE. For verification by interested readers, $q_z^* = 0.9080463337...$

Table 2.1: Values of a_k's and b_k's.

k	a_k	b_k
0	$1.00000000\cdots$	$-1.13521939\cdots$
1	$0.10126539\cdots$	$-0.18286643\cdots$
2	$0.00368062\cdots$	$-0.00812047\cdots$
3	$0.00006822\cdots$	$-0.00017002\cdots$
4	$0.00000076\cdots$	$-0.00000208\cdots$
5	0.57401517×10^{-8}	-0.16624533×10^{-7}
6	0.30842821×10^{-10}	$-0.94071713\times10^{-10}$

2.3.2 Solution at $\mathcal{O}(\sqrt{\epsilon})$

Before we go to $\mathcal{O}(\sqrt{\epsilon})$, consider

$$\ddot{x} + P(t)\dot{x} + Q(t)x = R(t), \tag{2.21}$$

where $P(t), Q(t), R(t)$ are bounded, periodic functions with period T. Assume that the complementary solution to Eq. (2.21) is a linear combination of h_1 and $h_2 + \alpha\, t\, h_1$ where h_1 and h_2 are T-periodic and α is some nonzero constant. Das and Chatterjee (2003) show that secular terms in the solution to Eq. (2.21) do not grow in amplitude faster than t^2. Moreover, under arbitrary but periodic forcing, secular terms in the particular solution are a linear combination of $t\,(2h_2 + \alpha\, t\, h_1)$ and $t\, h_1$. We will use these results below.

We now return to Eq. (2.14) at $\mathcal{O}(\sqrt{\epsilon})$, and we have

$$\frac{\partial^2 X_1}{\partial T_0^2} + 2\, q_z^* \cos(2T_0) X_1 = -2\, \frac{\partial^2 X_0}{\partial T_0 \partial T_1} - 2\, q_z^* \cos(2T_0) \left(\bar{h} X_0^2 + \bar{d} X_0^4 \right). \tag{2.22}$$

We note the similarity between Eq. (2.22) and Eq. (2.21) by identifying

$$x \equiv X_1,\ P(t) \equiv 0,\ Q(t) \equiv 2q_z^*\cos(2T_0),\ R(t) \equiv -2\, \frac{\partial^2 X_0}{\partial T_0 \partial T_1} - 2\, q_z^* \cos(2T_0) \left(\bar{h} X_0^2 + \bar{d} X_0^4 \right).$$

The complementary solution to Eq. (2.22) is a linear combination of ξ_1 and $\xi_2 + T_0\, \xi_1$ where ξ_1 and ξ_2 are given by Eqs. (2.16) and (2.18) and are 2π-periodic. Therefore, secular terms in the particular solution are a linear combination of $T_0\,(2\xi_2 + T_0\, \xi_1)$ ($\alpha = 1$ in our case) and $T_0\, \xi_1$. The general solution to Eq. (2.22) can be written as (Das and Chatterjee, 2003)

$$X_1 = c_1\xi_1 + c_2(\xi_2 + T_0\xi_1) + c_3 T_0\, \xi_1 + c_4 T_0\, (2\xi_2 + T_0\, \xi_1) + \Psi(T_0), \tag{2.23}$$

where c_1 through c_4 are constants and Ψ is 2π-periodic in T_0. Moreover, c_1 and c_2 are arbitrary, being part of the complementary solution. One linearly growing part of the particular solution can be nullified by a linearly growing part of the complementary solution (by choosing $c_2 = -c_3$). Although c_2 is thereby fixed, c_1 is still arbitrary. We now choose c_1 such that it nullifies the coefficient of $\cos(T_0)$ in $\Psi(T_0)$. By these arguments and simplifications,

$$X_1 = c_4 T_0 \, (2\,\xi_2 + T_0\,\xi_1) + \Psi(T_0), \tag{2.24}$$

where $\Psi(T_0)$ is 2π-periodic, has absorbed $c_1\,\xi_1 - c_3\,\xi_2$ and has no $\cos(T_0)$ term. That is,

$$X_1 = C_{2N+1} + \sum_{k=2}^{N} C_k \cos(kT_0) + \sum_{k=1}^{N} C_{k+N} \sin(kT_0) + C_{2N+2}\, T_0\, (2\xi_2 + T_0\xi_1), \tag{2.25}$$

where N is some positive integer (here we have taken $N = 12$) and the C_k's are coefficients to be determined. Note that $\cos(T_0)$ has been left out above.

Since ξ_1 and ξ_2 are approximate and the periodic part of X_1 is also approximate, the form of X_1 satisfies Eq. (2.22) only approximately. Therefore, after substituting Eq. (2.25) into Eq. (2.22), the left hand side will not be exactly equal to the right hand side. Bringing all terms to the left hand side, we obtain a nonzero residual. The unknown C_k's are determined by carrying out the Galerkin projection procedure used in a related context by Das and Chatterjee (2003). In this procedure the residual is separately multiplied by each basis function in the assumed form of the general solution (right hand side of Eq. (2.25)), namely

$$1,\ T_0\,(2\xi_2 + T_0\xi_1),\ \sin(T_0),\ \sin(2T_0),\ \cos(2T_0), \cdots,$$

and then each such product is integrated over one period (from 0 to 2π). Setting the integrals thus obtained to zero, we obtain $2N+1$ linear equations in the unknown coefficients C_k's. We solve for these coefficients and substitute them in Eq. (2.25) to obtain X_1.

A key point is that coefficient C_{2N+2} must be set to zero to avoid the secular terms and this, as is usual in the MMS, enables us to obtain the slow flow. From MAPLE we obtain, at $\mathcal{O}(\sqrt{\epsilon})$:

$$C_{2N+2} = 0.12873832\times10^{-9}\,\bar{h}\,A^2 - 0.30186541\times10^{-7}\,\bar{d}\,A^4 - 0.39256924\times10^{-9}\,\frac{\partial A}{\partial T_1}. \tag{2.26}$$

We note that the numerical coefficients are very small. We need to determine if they are actually numerically corrupted versions of exactly zero, i.e., if they should be set to zero. Noting that, from the Galerkin procedure, we have simultaneously obtained

$$C_2 = -0.67189535\,\bar{d}\,A^4 - 0.60163836\,\bar{h}\,A^2, \tag{2.27}$$

and

$$C_4 = 0.0045506\,\bar{d}\,A^4 - 0.006558\,\bar{h}\,A^2, \tag{2.28}$$

which involve much larger numerical coefficients, we conclude that C_{2N+2} is actually zero. Thus, we take $C_{2N+2} = 0$, and obtain no useful information at this order. We must proceed to a higher order calculation.

There are some technical issues in doing such higher order calculations, regarding the *asymptotic* validity of the method, but good approximations will nevertheless be obtained. The technical issues related to asymptotic validity are identical to those discussed in Nandakumar and Chatterjee (2005b) for averaging, and are not discussed here. The solution X_1 is given in Section 2.6.3.

2.3.3 Solution at $\mathcal{O}(\epsilon)$

We now proceed to $\mathcal{O}(\epsilon)$ which will provide useful information about the evolution of the amplitude A of the solution. From Eq. (2.14), at $\mathcal{O}(\epsilon)$, we have

$$\begin{aligned}\frac{\partial^2 X_2}{\partial T_0^2} + 2\,q_z^*\cos(2T_0)X_2 \;=\; & -\frac{\partial^2 X_0}{\partial T_1^2} - 2\,\frac{\partial^2 X_0}{\partial T_0 \partial T_2} - 2\,\frac{\partial^2 X_1}{\partial T_0 \partial T_1} \\ & -2\,\cos(2T_0)X_0 - 2\,\cos(2T_0)\,q_z^*\Big(2\bar{h}\,X_0X_1 + \bar{f}\,X_0^3 \\ & +2q_z^*\bar{d}X_0^3X_1 + q_z^*\bar{k}X_0^5\Big).\end{aligned} \tag{2.29}$$

Equation (2.29) also fits the form of Eq. (2.21). As was done for X_1 at $\mathcal{O}(\sqrt{\epsilon})$, here we take

$$X_2 = D_{2N+1} + \sum_{k=2}^{N} D_k\cos(kT_0) + \sum_{k=1}^{N} D_{k+N}\sin(kT_0) + D_{2N+2}\,T_0\,(2\xi_2 + T_0\xi_1), \tag{2.30}$$

where $N = 12$ as earlier, and D_k's are coefficients to be determined. We follow the Galerkin projection procedure again (as described earlier) to solve for the unknown D_k's. Setting D_{2N+2} equal to zero, we obtain

$$\begin{aligned}-1.9438\,\bar{h}^2A^3 + 0.44483\,\bar{f}\,A^3 - 4.7213\,\bar{d}^2A^7 + 0.48561\,\bar{k}A^5 \\ -6.4286\,\bar{h}\bar{d}\,A^5 + 0.43865\,\Delta\,A - 0.50000\,\frac{\partial^2 A}{\partial {T_1}^2} = 0.\end{aligned} \tag{2.31}$$

From Eq. (3.18), we have

$$\ddot{A} = \frac{d^2A}{d\tau^2} = \frac{\partial^2 A}{\partial T_0^2} + 2\sqrt{\epsilon}\frac{\partial^2 A}{\partial T_0 \partial T_1} + \epsilon\left(\frac{\partial^2 A}{\partial T_1^2} + 2\frac{\partial^2 A}{\partial T_0 \partial T_2}\right) + \mathcal{O}(\epsilon\sqrt{\epsilon}). \tag{2.32}$$

Since amplitude A is not a function of the fast variable T_0, we have

$$\ddot{A} = \epsilon \frac{\partial^2 A}{\partial T_1^2} + \mathcal{O}(\epsilon\sqrt{\epsilon}), \tag{2.33}$$

giving the required slow flow as

$$\begin{aligned} \ddot{A} &= \epsilon \Big(0.8773\,\Delta A - 3.8877\,\bar{h}^2 A^3 + 0.8897\,\bar{f}\,A^3 - 12.8564\,\bar{h}\,\bar{d}\,A^5 \\ &\quad + 0.9712\,\bar{k}\,A^5 - 9.4429\,\bar{d}^2 A^7 \Big) + \mathcal{O}(\epsilon\sqrt{\epsilon}). \end{aligned} \tag{2.34}$$

Note that, after setting $D_{2N+2} = 0$, we also have X_2. The solution X_2 is provided in Section 2.6.3 and is needed for higher order calculations.

Equation (2.34) is the second order slow flow for ion motion in the presence of hexapole, octopole, decapole and dodecapole superpositions. The presence of ϵ and Δ in the equation enables us to visualize ion dynamics at different values of detuning from q_z^*. In order to compare these results with the beat envelope equations of Sudakov (2001) (where separate equations were presented for hexapole and octopole superpositions), we plot the time trajectories predicted by these equations. To do this we transform the coefficients of Eq. (2.34) to the form of the beat envelope equations. Details of this comparative study are presented in Section 2.6.4, where agreement is observed with Sudakov's results except for one erroneous numerical coefficient which we correct here.

Using this systematic approach we have actually carried out calculations up to the fourth order, and the final fourth order slow flow equation is given, for completeness, in Section 2.6.1 (details are available in Marathe (2006)). This equation may be of use in the presence of somewhat larger weights of multipole superpositions. However, in the present study, we will use only the second order slow flow (Eq. (2.34)) for generating relevant phase portraits below.

2.3.4 Numerical verification

We next check the correctness of the slow flow we have obtained. We do this by first integrating Eq. (2.9) numerically, using the built-in routine ODE45 from MATLAB, with some chosen initial conditions. Numerical tolerances of 10^{-8} are specified for the integration routine.

Figures 2.1, 2.2 and 2.3 show comparisons between numerically obtained solutions of Eq. (2.9) and the amplitude obtained by solving the slow flow (Eq. (2.34)). In these plots we have selected $\epsilon = 0.001$, and the initial conditions for integration of Eq. (2.9) were taken as $\bar{z}(0) = 0.01$ and $\dot{\bar{z}}(0) = 0$. We obtain the corresponding initial conditions for the

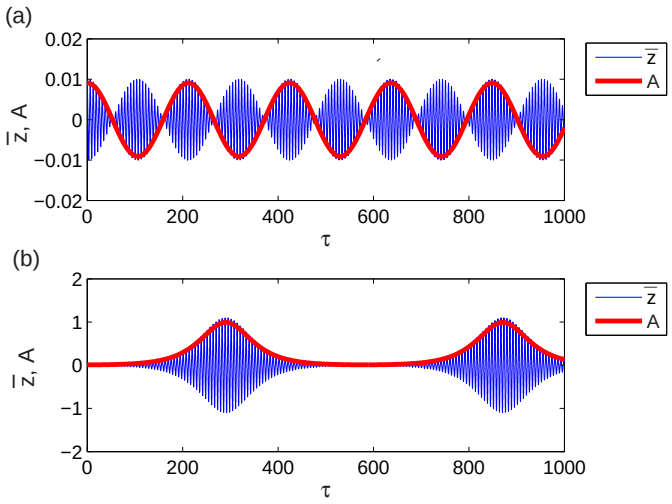

Figure 2.1: Comparison of amplitude (A) determined by solving the slow flow with the original Mathieu equation ($\bar{z}$) for positive and negative octopole. In both plots, $\epsilon = 0.001$, $\bar{z}(0) = 0.01$, $\dot{\bar{z}}(0) = 0$, $A(0) = 0.0091$, $\dot{A}(0) = 0$ and $\bar{h} = \bar{d} = \bar{k} = 0$. Further, we use for (a) $\bar{f} = 1$, $\Delta = -1$; and for (b) $\bar{f} = -1$, $\Delta = 1$.

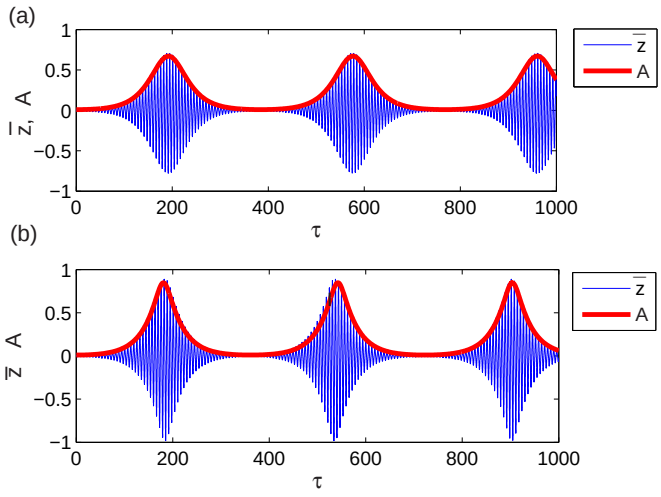

Figure 2.2: Comparison of amplitude (A) determined by solving the slow flow with the original Mathieu equation ($\bar{z}$) for hexapole and decapole. In both plots, $\epsilon = 0.001$, $\Delta = 1$, $\bar{z}(0) = 0.01$, $\dot{\bar{z}}(0) = 0$ and $\bar{f} = \bar{k} = 0$. Further, we use for (a) $\bar{h} = 1$, $\bar{d} = 0$, $A(0) = 0.0091$, $\dot{A}(0) = 0$; and for (b) $\bar{d} = 1$, $\bar{h} = 0$, $A(0) = 0.0101$, $\dot{A}(0) = 0$.

slow flow (Eq. (2.34)) by a method described in Section 2.6.5. The values of parameters used are given in the respective figure captions. For the purpose of comparison of the

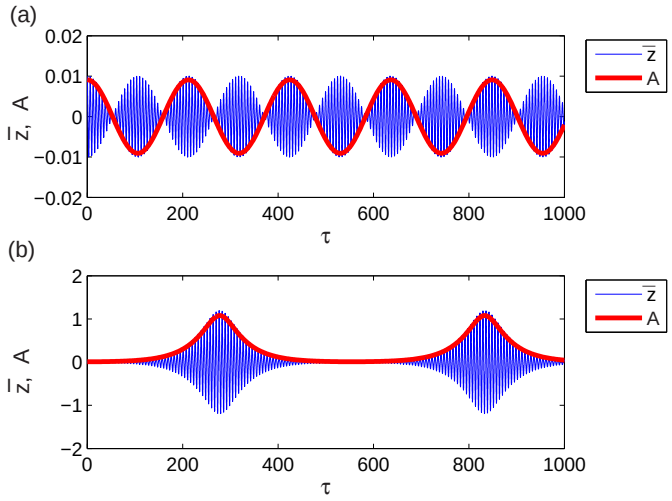

Figure 2.3: Comparison of amplitude (A) determined by solving the slow flow with the original Mathieu equation ($\bar{z}$) for positive and negative dodecapole. In both plots, $\epsilon = 0.001$, $\bar{z}(0) = 0.01$, $\dot{\bar{z}}(0) = 0$, $A(0) = 0.0091$, $\dot{A}(0) = 0$ and $\bar{h} = \bar{f} = \bar{d} = 0$. Further, we use for (a) $\bar{k} = 1$, $\Delta = -1$; and for (b) $\bar{k} = -1$, $\Delta = 1$.

two equations for a specific nonlinearity, the weights of the other superpositions are set to zero in both Eqs. (2.9) and (2.34).

Figure 2.1(a) presents the results for positive octopole and Fig. 2.1(b) for negative octopole. From the figure, a good match can be seen between the full numerical solution and MMS approximation. Figures 2.2(a) and 2.2(b) show results for hexapole and decapole superpositions where the effect of nonlinearity is sign independent. Figure 2.3(a) shows the comparison for positive dodecapole while Fig. 2.3(b) is for negative dodecapole. From these plots, it can be observed that the slow flow adequately represents the slow temporal variation in amplitude of the system in the neighborhood of the stability boundary.

2.4 Results and discussion

Equation (2.34) is the second order slow flow which describes variation in amplitude of ion motion in the presence of hexapole, octopole, decapole and dodecapole multipole superpositions. While the octopole ($\bar{f}$) and decapole ($\bar{k}$) appear as linear terms, the hexapole ($\bar{h}$) and decapole ($\bar{d}$) appear independently as quadratic terms as well as in combination in one of the terms. This last observation, namely that of $\bar{h}$ and $\bar{d}$ appearing

as a combination, has two interesting consequences. First, the sign of the hexapole will affect dynamics only if decapole superposition is *also* present. Second, for the sign of hexapole superposition to affect ion dynamics its sign change must be independent of decapole superposition. These consequences are also borne out by the fourth order slow flow which includes a larger number of terms (see Section 2.6.1 and the caveats therein).

We now return to our original problem of understanding ion dynamics in the presence of field inhomogeneities. The nonlinearities considered here are hexapole, octopole, decapole and dodecapole. This study will rely on interpreting numerically generated phase portraits, obtained from the slow flow (Eq. (2.34)), at different values of Δ. In the

Table 2.2: q_z at different values of Δ, for $\epsilon = 0.001$.

Δ	q_z
-2.0	0.9060463
-1.0	0.9070463
-0.5	0.9075463
-0.1	0.9079463
-0.001	0.9080453
0.25	0.9082963
0.6	0.9086463
1.0	0.9090463
2.0	0.9100463
8.0	0.9160463

phase portraits presented, we have varied Δ from -2 to $+8$, and the corresponding q_z values are presented in Table 2.2 for ready reference. These q_z values are calculated by substituting $q_z^* = 0.908046$ and $\epsilon = 0.001$ in Eq. (2.8). All the phase portraits are generated keeping the value of ϵ at 0.001. The slow flow equations are integrated repeatedly for a large number of initial conditions and the phase portraits are obtained by plotting the derivative of the amplitude ($\dot{A}$) on the y-axis and amplitude (A) on the x-axis.

Although in real traps the field has more than one higher order multipole superposition, for the sake of clarity of the discussion we study the effect of each multipole superposition individually. The effect of combinations of multipoles may be evaluated by a suitable choice of terms in the slow flow equation (Eq.(2.34)) and will not be explicitly discussed in this chapter.

2.4.1 Positive octopole

We set $\bar{h} = \bar{d} = \bar{k} = 0$ in Eq. (2.34) to study the effect of octopole superpositions. The right hand side of Eq. (2.34) is a cubic polynomial in amplitude A. The roots of this polynomial are

$$(-0.9940\sqrt{-\Delta/\,\bar{f}}\,,\ 0),\quad (0,0)\ \text{ and }\ (0.9940\sqrt{-\Delta/\,\bar{f}}\,,\ 0).$$

These, if real, are also the fixed points of the slow flow. Since $\bar{f}$ is positive, for positive values of Δ, there exists only one fixed point at $(0,0)$ and this is a saddle, indicating that the ion is unstable. For negative Δ values, however, there are three fixed points. For instance, for $f = 0.01$ (i.e., $\bar{f} = 20$ for $\epsilon = 0.001$) and $\Delta = -2$, these fixed points occur at $A = 0$, $A = \pm 0.3143$. The two nonzero fixed points are now saddles and consequently ions will be stable only near the origin (a center) where the solution is bounded. As we vary Δ from -2 towards 0 (that is, towards the stability boundary), the non-zero fixed points move towards each other. This can be observed from Figs. 2.4(a) to 2.4(d) which show the phase portraits generated by numerically integrating Eq. (2.34). For $\Delta = -0.5, -0.1$, and -0.001, the nonzero fixed points are ± 0.1572, ± 0.0703, and ± 0.00703 respectively.

From Figs. 2.4(a) through 2.4(d), it can also be observed that the area of the region around the center where the solution is bounded diminishes as Δ is varied from -2 to -0.001, and ions with initial conditions which would earlier have been stable now are unstable and escape to infinity. For Δ values very close to 0, but less than 0, the area in the phase space where the solution is bounded is so small that all ions with significant energies escape. The phase portraits present qualitatively a similar picture to Sudakov's (Sudakov, 2001) observation that for positive octopole there is a potential well within the stable region and the width and depth of this well decreases as q_z approaches the boundary. In the context of our study, the central region in the phase portrait (with closed curves) corresponds to the potential well discussed by Sudakov (2001).

2.4.2 Negative octopole

We now consider the ion dynamics in the neighborhood of the stability boundary with 1% negative octopole nonlinearity. Since $\bar{f}$ is negative, for negative values of Δ, Eq. (2.34) will have only one fixed point. This will be a center and hence the ion will be stable. For positive values of Δ (i.e., beyond the nominal stability boundary), there exist 3 fixed points consisting of a saddle and two centers (one on each side of the saddle). As Δ is increased to values greater than 0, these centers move away from each other. The centers for $\Delta = 2$ are at $A = \pm 0.3143$ and for $\Delta = 8$ are at $A = \pm 0.6287$.

Figures 2.5(a) through 2.5(d) show the phase portraits generated by numerically in-

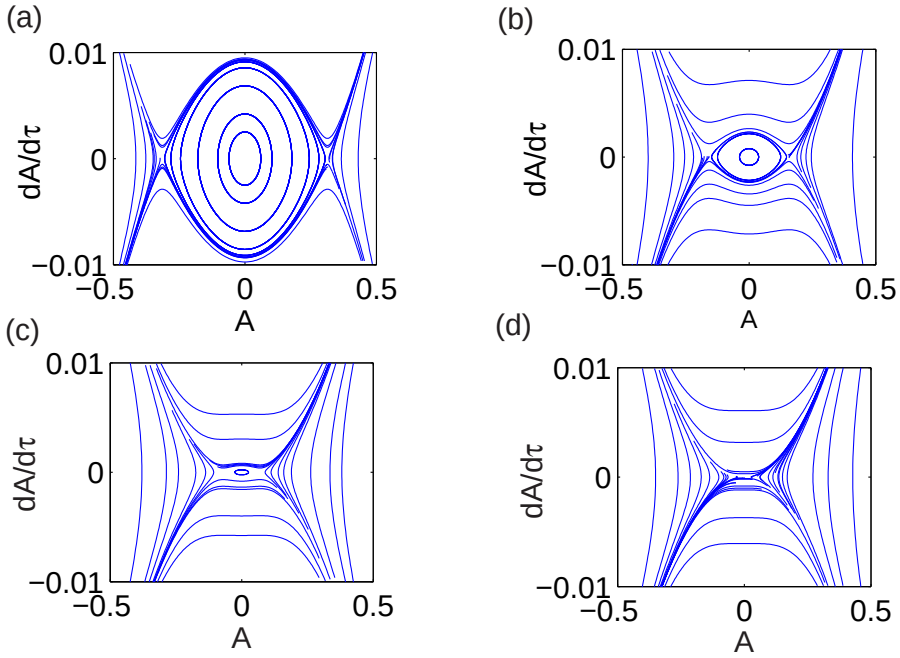

Figure 2.4: Phase portrait for 1% octopole ($f = 0.01$, $\bar{f} = 20$, $\epsilon = 0.001$) for Δ values of (a) -2, (b) -0.5, (c) -0.1 and (d) -0.001.

tegrating Eq. (2.34) for Δ values corresponding to -1, 0, 2 and 8, respectively, for 1% negative octopole nonlinearity. Referring to Figs. 2.5(a) and 2.5(b), there exists only one fixed point and this is a center. All ions which were originally located near the trap center will continue to execute stable oscillations and will not escape from the trap. When the q_z value of the ion is increased beyond q_z^* (where Δ is positive), the phase portrait qualitatively changes its nature. As can be seen from Figs. 2.5(c) and 2.5(d), the origin which was earlier a center now becomes a saddle and two new centers are created. Thus an ion will oscillate in a path (in averaged or slow phase space) that encircle either one of the centers, or both centers. For very small positive values of Δ, ion amplitude does not exceed the trap boundary and ions are therefore confined within the trap cavity. Increasing the detuning parameter Δ increases the maximum amplitude that an ion oscillation encircling a center can have. Eventually, for large enough Δ, ion motion amplitudes exceed the trap dimensions, and so the ion gets ejected (also see numerical simulation of this phenomenon in Sudakov (2001)). Thus, in the presence of negative octopole superposition, ion oscillations continue to be inherently stable well beyond q_z^* and ion escapes from the trap only when amplitude reaches the trap boundary.

Here too, our results are consistent with Sudakov's (Sudakov, 2001) observation of a double well potential function for negative octopole superposition. The regions around the two centers (with closed curves) on either side of the saddle, observed for positive

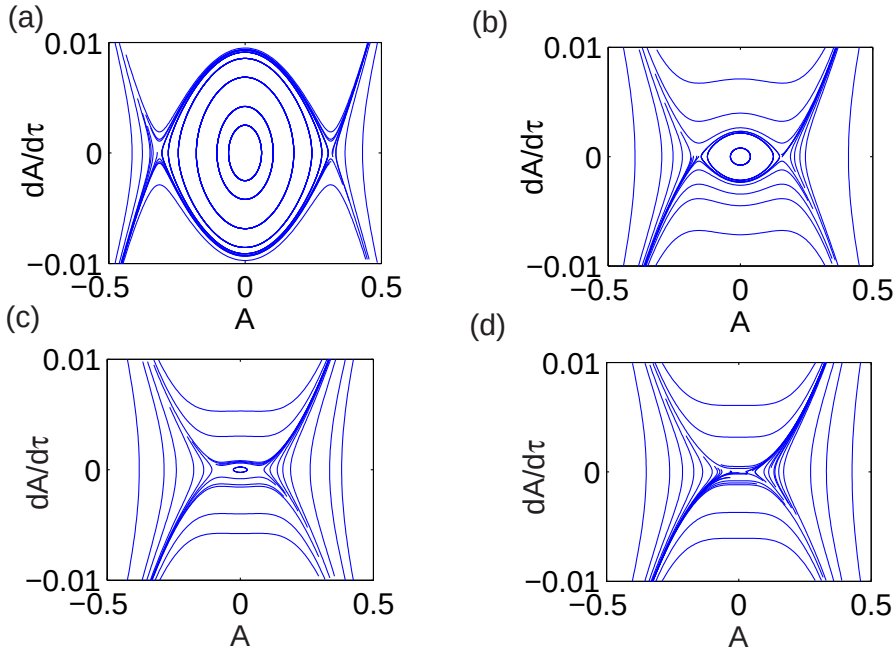

Figure 2.5: Phase portrait for −1% octopole ($f = 0.01$, $\bar{f} = 20$, $\epsilon = 0.001$) for Δ values of (a) −1, (b) 0, (c) 2 and (d) 8.

values of Δ, correspond to the double well potential shown in that study.

2.4.3 Hexapole

The effect of hexapole superposition can be studied by setting $\bar{f} = \bar{d} = \bar{k} = 0$ in Eq. (2.34). It is observed that the hexapole nonlinearity parameter $\bar{h}$ appears in squared form which implies that the sign of hexapole nonlinearity will not affect the slow flow. This is in agreement with the simulation studies of Franzen et al. (1995).

The roots of the polynomial obtained by equating the right hand side of Eq. (2.34) to zero are

$$(-0.4750\sqrt{\Delta/\bar{h}^2}, 0), \quad (0,0) \quad \text{and} \quad (0.4750\sqrt{\Delta/\bar{h}^2}, 0).$$

For negative values of Δ there will be only one fixed point at (0, 0) and this will be a center. When Δ takes positive values, similar to the case of negative octopole nonlinearity, two centers and a saddle will appear.

Figures 2.6(a) through 2.6(d) show the phase portraits for 1% positive hexapole superposition (i.e., $\bar{h} = 0.47$ for $\epsilon = 0.001$) for Δ values −1, 0, 0.25 and 0.6, respectively. As can be seen from these figures, we get the same qualitative behavior as we obtained in case

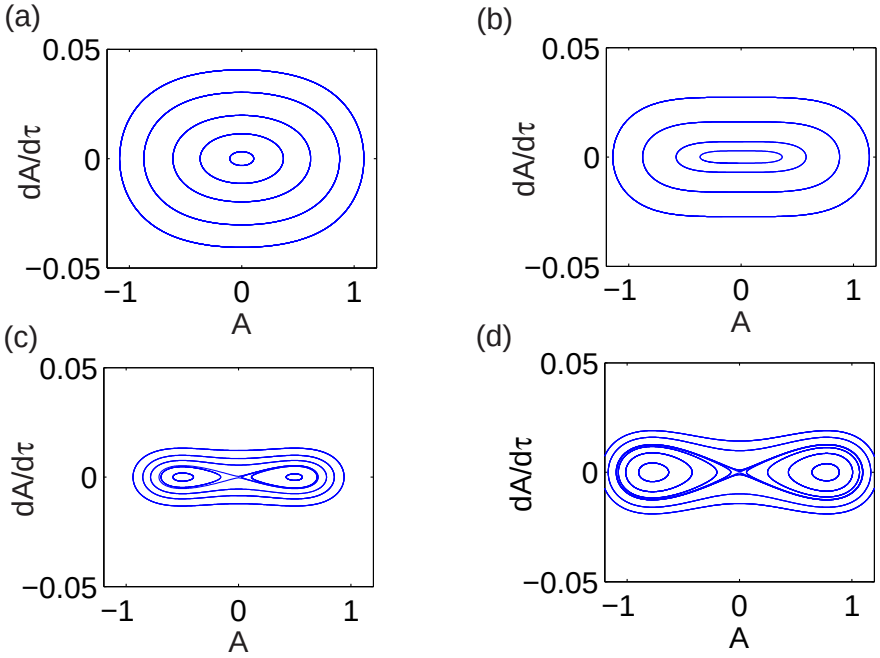

Figure 2.6: Phase portrait for 1% hexapole ($h = 0.01$, $\bar{h} = 0.47$, $\epsilon = 0.001$) for Δ values of (a) -1, (b) 0, (c) 0.25 and (d) 0.6.

of the negative octopole nonlinearity, for both negative and positive values of Δ. This observation can also be understood from Eq. (2.34) where the qualitative behavior of the slow flow for the hexapole nonlinearity (in the absence of all others) will become similar to the slow flow for the *negative* octopole nonlinearity (in the absence of all others).

Notice, however that $\bar{h}\,\bar{d}$ appears in the slow flow, so sign independence is violated when multiple multipoles are present. Moreover, at the fourth order (see Section 2.6.1) this symmetry is further lost due to the simultaneous presence of $\bar{h}\,\bar{d}$ as well as $\bar{h}^2\,\bar{d}$ (but see the caveats presented therein).

2.4.4 Decapole

To study the effect of decapole superposition we set $\bar{h} = \bar{f} = \bar{k} = 0$ in Eq. (2.34). The slow flow equation reduces to

$$0.8773\,\Delta A - 9.4429\,\bar{d}^2 A^7 = 0. \tag{2.35}$$

Figures 2.7(a) to 2.7(d) show the phase portraits for 1% decapole superposition (i.e., $\bar{d} = 0.79$ for $\epsilon = 0.001$). The phase portraits are qualitatively similar to the phase portraits obtained for hexapole superposition. As in the case of hexapole, delayed ejection

is suggested by these phase portraits. The fixed point of the system when Δ is negative is (0,0). In this case the system exhibits stable oscillations. For positive values of Δ there will be three fixed points. For $\Delta = 0.25$ these are $(-0.5778, 0)$, $(0, 0)$ and $(0.5778, 0)$. From the phase portraits it can be observed that origin of the A-$\dot{A}$ plane is a saddle and the nonzero fixed points are centers. As Δ is increased to 2, the two nonzero fixed points move further apart to $(\pm 0.7857, 0)$. Ions are ejected from the trap when their amplitudes reach the trap boundary.

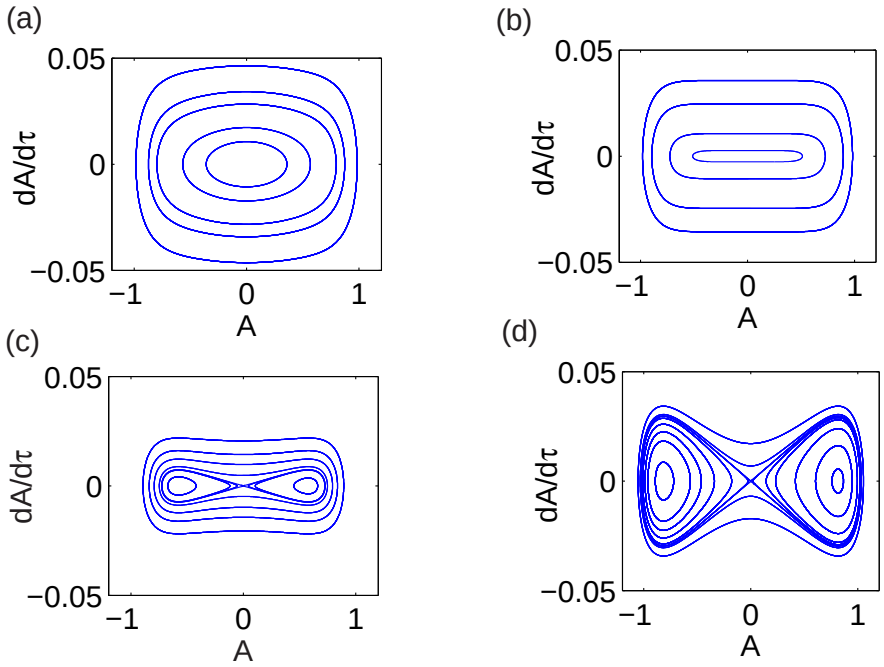

Figure 2.7: Phase portrait for 1% decapole ($d = 0.01$, $\bar{d} = 0.79$, $\epsilon = 0.001$) for Δ values (a) -1, (b) 0, (c) 0.25 and (d) 2.

2.4.5 Positive dodecapole

The influence of dodecapole nonlinearity may be investigated by setting $\bar{h} = \bar{f} = \bar{d} = 0$ in Eq. (2.34). The slow flow reduces to

$$0.8773\,\Delta A - 0.9712\,\bar{k}A^5 = 0. \tag{2.36}$$

The system represented by this equation has three fixed points when Δ is negative and $\bar{k}$ is positive. The phase portraits for 1% dodecapole superposition (i.e., $\bar{k} = 30$ for $\epsilon = 0.001$) are shown in Figs. 2.8(a) to 2.8(d). When $\Delta = -0.5$ the fixed points are $(-0.3503, 0)$, $(0, 0)$ and $(0.3503, 0)$. The two nonzero fixed points are saddles and the origin is a center.

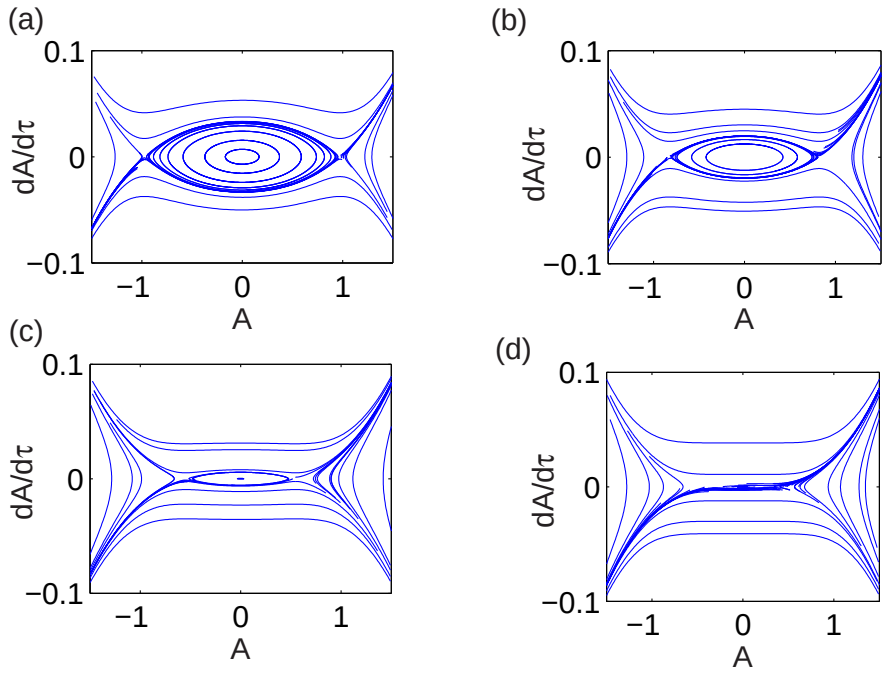

Figure 2.8: Phase portrait for 1% dodecapole ($k = 0.01$, $\bar{k} = 30$, $\epsilon = 0.001$) for Δ values of (a) -0.5, (b) -0.1, (c) -0.01 and (d) -0.001.

As Δ is increased (that is, when q_z approaches q_z^*) the two nonzero fixed points move closer to the origin. From Fig. 2.8(d) corresponding to $\Delta = -0.001$, the center is almost gone and almost all initial conditions lead to unbounded solutions (ejection).

2.4.6 Negative dodecapole

When $\bar{k}$ is negative there exists only one fixed point at (0,0) for negative values of Δ. From Fig. 2.9(a), which is plotted for -1% dodecapole superposition at $\Delta = -1$, it can be seen that the system exhibits stable oscillations. However, for positive values of Δ there are three fixed points. Figures 2.9(c) and 2.9(d) corresponding to $\Delta = 1$ and $\Delta = 8$, respectively, show that the nonzero fixed points are centers and the origin is a saddle. Ions are ejected from the trap when the ion oscillation amplitude reaches the trap boundary.

2.5 Concluding remarks

The motivation of this chapter was to understand the dynamics associated with early and delayed ejection of ions in Paul traps operated in the mass selective ejection mode. The studies reported in this chapter will be of use in understanding dynamics at the

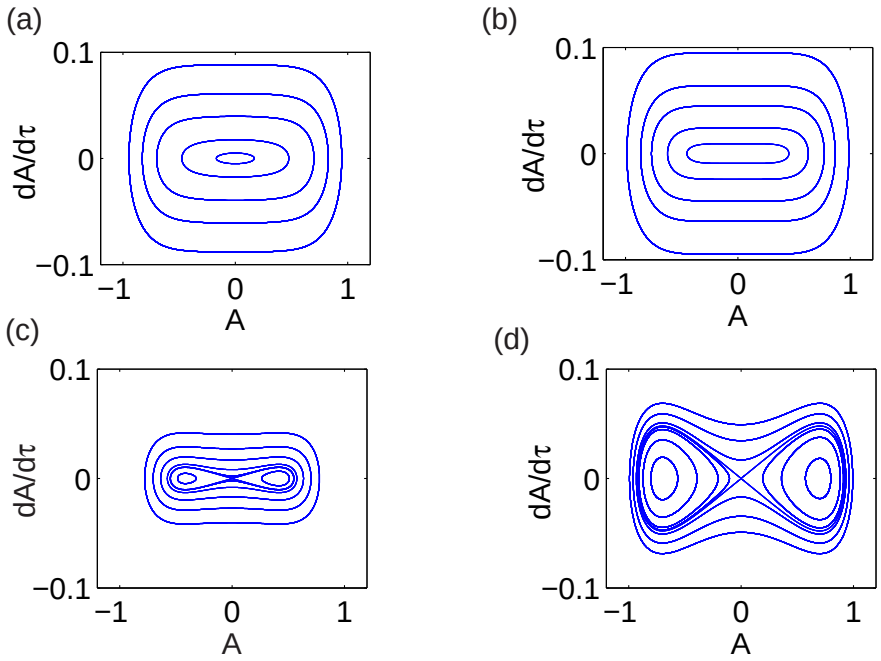

Figure 2.9: Phase portrait for -1% dodecapole ($k = 0.01$, $\bar{k} = 30$, $\epsilon = 0.001$) for Δ values of (a) -1, (b) 0, (c) 1 and (d) 8.

stability boundary in all traps where the nonlinear Mathieu equation determines ion stability. Examples of mass analyzer configurations which are attracting considerable interest include the 2D (linear) Paul trap and the cylindrical trap, in addition to the hyperboloid geometry Paul trap.

The equation of motion of ions in the axial direction of the trap with hexapole, octopole, decapole and dodecapole superpositions was studied using the method of multiple scales. The ordering scheme used has allowed a systematic inclusion of higher order multipoles. Details of the analysis have been provided and our results are compared with those of Sudakov (2001). Although a fourth order slow flow equation has been computed and reported for potential future use in traps with larger weights of multipole superpositions, in our present study we have used the second order slow flow (Eq. (2.34)) for generating phase portraits. Phase portraits generated by numerical integration of the slow flow have been used to predict the qualitative behavior of ion motion near the stability boundary in the presence of nonlinearities. The presence of positive even multipoles was seen to cause early ejection and negative even multipoles to cause delayed ejection of ions. Independently present odd multipoles of either sign have the same effect as negative even multipoles in causing delayed ejection.

While our present study has served to reinforce conclusions arrived at by earlier workers

who focussed on the influence of field inhomogeneities causing delayed ejection in mass selective boundary ejection experiments, it offers a few new insights.

First, we now have a better understanding on the role of hexapole superposition, specifically to the way in which its sign is important in discussion of ion dynamics at the boundary. To re-iterate our observation, the common perception is that the dynamics is unaffected if $\bar{h}$ changes sign. We report that the dynamics is unaffected if $\bar{h}$ and $\bar{d}$ change sign *simultaneously* but not otherwise (assuming both $\bar{h}$ and $\bar{d}$ are nonzero). Furthermore, when $\bar{d} = 0$, the sign-independence of the dynamics on $\bar{h}$ holds up to even the next order in the analysis (going beyond Franzen et al. (1995)).

A second important contribution that the present study makes is to trap designers. As mentioned in our introductory remarks in this chapter, newer trap geometries are under current investigation and their design optimization is performed either empirically or through numerical simulations. These techniques do not lend themselves to easily summarizing the effects of a large number of possible parameter variations. Considering that calculation of multipole contribution to the field within the trap cavity for a specified trap geometry is fairly routine and straightforward, inserting the weights of multipole superpositions for these geometries in the slow flow will enable easy visualization of ion dynamics at different q_z values in the neighborhood of the nominal stability boundary. This will help designers in understanding the effects of specific combinations of multipole superpositions in mass analyzers being investigated by them for use in mass selective boundary ejection experiments.

2.6 Appendix

2.6.1 Fourth order MMS slow flow

The slow flow equation after carrying out the fourth order multiple scales analysis will be in the form

$$\begin{aligned}
\ddot{A} \;=\; & \epsilon\,(-12.8564\,\bar{h}\,\bar{d}A^5 - 9.44304\,\bar{d}^2A^7 - 3.88769\,\bar{h}^2A^3 + 0.97124\,\bar{k}\,A^5 \\
& +0.87729\,\Delta\,A + 0.88965\,\bar{f}\,A^3 + 39.31546\,\bar{h}^2\dot{A}^2A - 5.50581\,\bar{f}\,\dot{A}^2A \\
& +657.373\,\bar{d}^2\dot{A}^2A^5 - 20.2091\,\bar{k}\,\dot{A}^2A^3 + 411.774\,\bar{h}\bar{d}\,\dot{A}^2\,A^3) \\
& +\epsilon^2\,(-0.18369\,\Delta^2A - 125.986\,\bar{h}^4A^5 - 1892.91\,\bar{d}^4A^{13} + 290.186\,\bar{h}\,\bar{f}\,\bar{d}A^7 \\
& +493.157\,\bar{h}\,\bar{d}\bar{k}\,A^9 + 389.577\,\bar{d}^2\bar{k}A^{11} - 1176.36\,\bar{h}^3\bar{d}A^7 - 3572.55\,\bar{h}^2\bar{d}^2A^9 \\
& +151.374\,\bar{h}^2\bar{k}A^7 - 7.64328\,\bar{d}\bar{k}\,A^7 + 23.3241\,\Delta\bar{h}^2A^3 + 78.6875\,\bar{h}^2\bar{d}A^5 \\
& +251.73\,\bar{f}\,\bar{d}^2A^9 + 133.2125\,\Delta\,\bar{d}^2A^7 - 1.76775\,\Delta\,\bar{d}A^3 - 4394.78\,\bar{h}\,\bar{d}^3A^{11} \\
& -3.843405\,\Delta\bar{k}\,A^5 + 121.976\,\Delta\,\bar{h}\,\bar{d}A^5 - 2.60912\,\bar{d}^2A^5 - 5.22277\,\bar{k}^2A^9) \quad (2.37)
\end{aligned}$$

Note that higher order MMS gives non-unique results (due to arbitrariness in the choice of X_1 in Eq. (2.23)). Moreover, due to harmonic balance approximations, the numerical coefficients above are not exact. However, the spirit of the calculation is correct in principle and a useful approximation is obtained, and so these terms are reported here for record.

2.6.2 Choice of time scales in MMS

Time scales chosen in the MMS when applied to Eq. (2.9) are $T_0 = \tau$, $T_1 = \sqrt{\epsilon}\,\tau$, $T_2 = \epsilon\tau$, $\cdots$. Our choice is based on the following.

We consider

$$\frac{d^2x}{d\tau^2} + 2(q_z^* + \epsilon\Delta)\,\cos(2\tau)(x + \epsilon\,x^3) = 0, \tag{2.38}$$

which can be rewritten as

$$\frac{d^2x}{d\tau^2} + 2q_z^*\cos(2\tau)\,x + 2\epsilon\,\cos(2\tau)(q_z^*\,x^3 + \Delta x) + \mathcal{O}(\epsilon^2) = 0. \tag{2.39}$$

We numerically integrate Eq. (2.39), neglecting $\mathcal{O}(\epsilon^2)$ terms, with initial conditions $x(0) = 0.01$ and $\dot{x}(0) = 0$ for a fixed value of $\epsilon = 0.001$. We observe the period of the slowly varying amplitude to be $T = 433.25$ (Fig. 10(a)). With the same initial conditions, we integrate Eq. (2.39) again, but now for $\epsilon = 0.002$. This time period of the solution is observed to be $T = 306.35$. Note that $433.25/306.35 \approx 1.414.. \approx \sqrt{2}$. The solution for $\epsilon = 0.002$ is therefore plotted against $\sqrt{2}\,\tau$ instead of τ and we get approximately the same period i.e. $T \approx 433.25$ (Fig. 10(b)). This observation suggests that the $\sqrt{\epsilon}\,\tau$ time scale is present in the solution. We support our observation further using an analogy. The unperturbed equation in case of Eq. (2.9) is

$$\frac{d^2x}{d\tau^2} + 2\,q_z^*\cos(2\tau)\,x = 0. \tag{2.40}$$

This equation is a linear Mathieu equation with q_z^* value corresponding to q at the stability boundary. Eq. (2.40) has two linearly independent solutions, one periodic with constant amplitude and the other with amplitude growing linearly with time.

Now consider

$$\frac{d^2x}{d\tau^2} = 0. \tag{2.41}$$

It is a second order, linear homogeneous ordinary differential equation. It has two linearly independent solutions, one constant and the other linearly growing with respect to time, similar at an abstract level to the behavior of the amplitude for the linear Mathieu

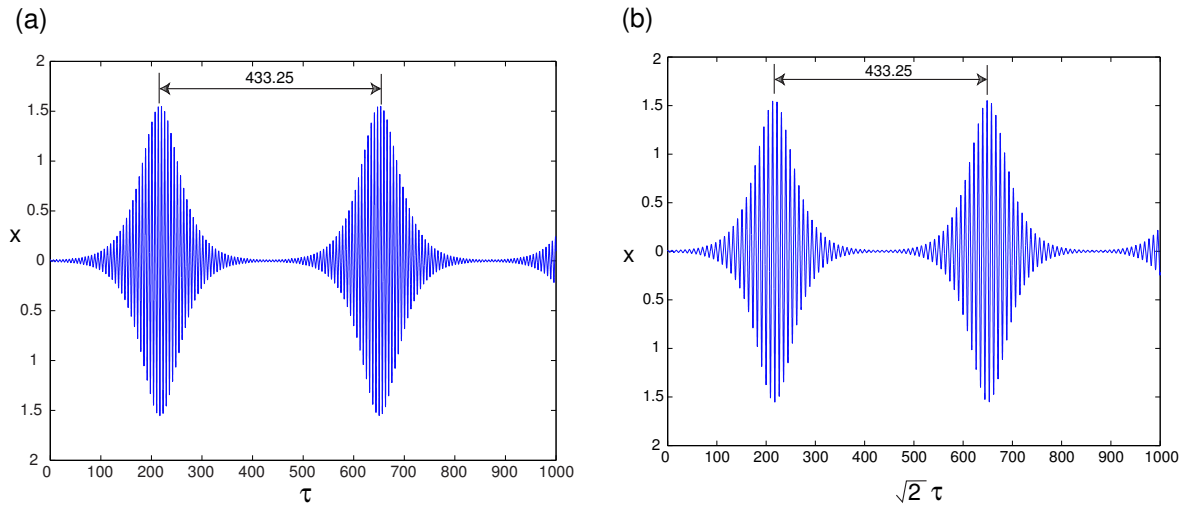

Figure 2.10: Time period of the amplitude for (a) $\epsilon = 0.001$ and (b) $\epsilon = 0.002$.

equation. If we perturb Eq. (2.41) as

$$\frac{d^2x}{d\tau^2} + \epsilon x = 0, \tag{2.42}$$

the solution becomes

$$x = A\cos(\sqrt{\epsilon}\,\tau) + B\sin(\sqrt{\epsilon}\,\tau), \tag{2.43}$$

where A and B depend upon the initial conditions. We see that time scale $\sqrt{\epsilon}\,\tau$ is present in the solution.

Equation (2.9) is a perturbation to Eq. (2.40). So we expect time scales τ, $\sqrt{\epsilon}\tau$, $\epsilon\tau$, $\cdots$ to be present in the solution. The final MMS approximation, of course, is amply supported by full numerical checks.

2.6.3 Expressions for X_1 and X_2

The solution for X_1 (not displaying the coefficients which are less than 10^{-5}) is

$$\begin{aligned} X_1 \approx\ & -1.13522\,\frac{\partial A}{\partial T_1}\sin(T_0) - 0.18287\,\frac{\partial A}{\partial T_1}\sin(3\,T_0) - 0.00812\,\frac{\partial A}{\partial T_1}\sin(5\,T_0) \\ & -0.00017\,\frac{\partial A}{\partial T_1}\sin(7\,T_0) - 0.60164\,\bar{h}\,A^2\cos(2\,T_0) - 0.6719\,\bar{d}\,A^4\cos(2\,T_0) \\ & +0.00066\,\bar{h}\,A^2\cos(4\,T_0) + 0.00455\,\bar{d}\,A^4\cos(4\,T_0) + 0.00268\,\bar{h}\,A^2\cos(6\,T_0) \\ & +0.0078\,\bar{d}\,A^4\cos(6\,T_0) + 0.00016,\bar{h}\,A^2\cos(8\,T_0) + 0.00116\,\bar{d}\,A^4\cos(8\,T_0) \\ & +0.00011\,\bar{d}A^4\cos(10\,T_0) - 2.07004\,\bar{d}A^4 - 1.88307\,\bar{h}A^2 \end{aligned} \tag{2.44}$$

The solution for X_2 (not displaying the coefficients which are less than 10^{-5}) is

$$\begin{aligned}
X_2 \;\approx\; & 1.1332\,\bar{h}\,A\frac{\partial A}{\partial T_1}\sin(2\,T_0) + 2.46062\,\bar{d}\,A^3\frac{\partial A}{\partial T_1}\sin(2\,T_0) - 0.00693\,\bar{h}\,A\frac{\partial A}{\partial T_1}\sin(4\,T_0) \\
& +0.03699\,\bar{d}\,A^3\frac{\partial A}{\partial T_1}\sin(4\,T_0) - 0.00963\,\bar{h}\,A\frac{\partial A}{\partial T_1}\sin(6\,T_0) - 0.03737\,\bar{d}\,A^3\frac{\partial A}{\partial T_1}\sin(6\,T_0) \\
& -0.00066\,\bar{h}\,A\frac{\partial A}{\partial T_1}\sin(8\,T_0) - 0.00662\,\bar{d}\,A^3\frac{\partial A}{\partial T_1}\sin(8\,T_0) - 0.00002\,\bar{h}\,A\frac{\partial A}{\partial T_1}\sin(10\,T_0) \\
& -0.00073\,\bar{d}\,A^3\frac{\partial A}{\partial T_1}\sin(10T_0) - 0.00006\,\bar{d}\,A^3\frac{\partial A}{\partial T_1}\sin(12\,T_0) \\
& +0.14628\,\Delta\,A\,\cos(3T_0) - 0.02631\,\bar{h}^2\,A^3\,\cos(3T_0) - 0.00325\,\bar{f}\,A^3\,\cos(3T_0) \\
& -0.00009\,\bar{f}\,A^5\,\cos(3T_0) - 0.00195\,\bar{h}\,\bar{d}\,A^5\,\cos(3T_0) + 0.02946\,\bar{d}^2\,A^7\,\cos(3T_0) \\
& +0.00187\,\Delta\,A\,\cos(5T_0) - 0.02469\,\bar{h}^2\,A^3\,\cos(5T_0) + 0.01234\,\bar{f}\,A^3\,\cos(5T_0) \\
& -0.15887\,\bar{h}\,\bar{d}\,A^5\,\cos(5T_0) + 0.01857\,\bar{f}\,A^5\,\cos(5T_0) - 0.1447\,\bar{d}^2\,A^7\,\cos(5T_0) \\
& +0.00007\,\Delta\,A\,\cos(7T_0) - 0.00159\,\bar{h}^2\,A^3\,\cos(7T_0) + 0.00186\,\bar{f}\,A^3\,\cos(7T_0) \\
& -0.02564\,\bar{h}\,\bar{d}\,A^5\,\cos(7T_0) + 0.00456\,\bar{f}\,A^5\,\cos(7T_0) - 0.02621,\bar{d}^2\,A^7\,\cos(7T_0) \\
& -0.00001\,\bar{h}^2\,A^3\,\cos(9T_0) + 0.00015\,\bar{f}\,A^3\,\cos(9T_0) - 0.00231\,\bar{h}\,\bar{d}\,A^5\,\cos(9T_0) \\
& -0.000728\,\bar{f}\,A^5\,\cos(9T_0) - 0.00246\,\bar{d}^2\,A^7\,\cos(9T_0) - 0.00013\,\bar{h}\,\bar{d}\,A^5\,\cos(11T_0) \\
& +0.00009\,\bar{f}\,A^5\,\cos(11T_0) - 0.00011\,\bar{d}^2\,A^7\,\cos(11T_0) \qquad (2.45)
\end{aligned}$$

X_1 and X_2 are provided here with numerical coefficients of their terms truncated to 5 decimal places. In our calculations using MAPLE, more digits were retained.

2.6.4 Comparison of second order slow flow with beat envelope equation of Sudakov (2001)

We reproduce Sudakov's equation of ion motion (Eq. (9) in Sudakov (2001)) below,

$$\frac{d^2u}{d\xi^2} + 2q_0\cos(2\xi)u = 2\,(q_0 - q)\cos(2\xi)\,u - q\cos(2\xi)\,4\,\alpha_4\,u^3, \qquad (2.46)$$

where $u = \dfrac{z}{z_0}$, $\xi = \dfrac{\Omega\,t}{2}$ $(= \tau$, in our study), $q_0 = q_z^*$ (in our study), $\alpha_4 = f\,\dfrac{z_0^2}{r_0^2}$ $(= \epsilon\dfrac{\bar{f}}{2}\,\dfrac{z_0^2}{r_0^2}$, in our study). The solution to Eq. (2.46) is assumed to be of the form (Eq. (A1) in Sudakov (2001))

$$\begin{aligned}
u(\xi) \;=\; & \epsilon Z\,u_1(\xi) + \epsilon^2\Big(h_1\sin(\xi) + h_3\sin(3\xi) + \cdots\Big) + \\
& \epsilon^3\Big(g_3\cos(3\xi) + g_5\cos(5\xi) + \cdots\Big), \qquad (2.47)
\end{aligned}$$

where Z is the beat envelope (our "amplitude") and u_1 is the periodic solution of the linear Mathieu equation at the stability boundary and h_k's and g_k's are slowly varying amplitudes of the harmonics.

The beat envelope equation has been found by Sudakov (2001) to be

$$\frac{d^2Z}{d\xi^2} + 0.8873\,(q_0 - q)Z - 1.4572\,\alpha_4 Z^3 = 0. \tag{2.48}$$

However, the slow flow equation (Eq. (2.34)) derived by us, when there is only octopole nonlinearity, has the form

$$\ddot{A} = \epsilon\,(0.8773\,\Delta A + 0.8897\,\bar{f}A^3). \tag{2.49}$$

We must now transform our equation, Eq. (2.49), to the form presented by Sudakov (2001). This will require transforming different parameters in our equation to conform to Eq. (2.48). This is described below.

We nondimensionalized the axial position variable z as $\bar{z} = \dfrac{z}{r_0}$; since $u = \dfrac{z}{z_0}$, we have $\bar{z} = \dfrac{z_0}{r_0}\,u$. Since $\bar{z} = X_0 + \mathcal{O}(\sqrt{\epsilon}) = A\,\xi_1 + \mathcal{O}(\sqrt{\epsilon})$, we write $\bar{z} \approx A\,\xi_1$ i.e., $\dfrac{z_0}{r_0}\,u \approx A\,\xi_1$. Sudakov shows in Appendix A of Sudakov (2001) that his h_k's and g_k's are of the first and second orders, respectively. Since ϵ is a book-keeping parameter in that study (the correspondence between Sudakov's ϵ and ours is therefore not direct, and is avoided in this discussion), we can write $u \approx Z\,u_1$, and therefore $A \approx \left(\dfrac{z_0}{r_0}\right)\left(\dfrac{u_1}{\xi_1}\right)Z$. Finally, substituting $\bar{f} = \dfrac{2}{\epsilon}\,\dfrac{r_0^2}{z_0^2}\,\alpha_4$, $\Delta = -\dfrac{q_0 - q}{\epsilon}$ and $A \approx \dfrac{z_0}{r_0}\dfrac{u_1}{\xi_1}Z$ into Eq. (2.49), we obtain

$$\frac{d^2Z}{d\xi^2} + 0.8873\,(q_0 - q)\,Z - 1.7794\left(\frac{u_1}{\xi_1}\right)^2\alpha_4\,Z^3 = 0. \tag{2.50}$$

From Eq. (10) of Sudakov (2001), it can be seen that u_1 is scaled such that all coefficients in the solution add to 1. In our study, we have not imposed this condition on ξ_1 and we have obtained, instead, $u_1/\xi_1 = 0.90495$. Substituting this, Eq. (2.50) then becomes

$$\frac{d^2Z}{d\xi^2} + 0.8873\,(q_0 - q)\,Z - 1.4572\alpha_4\,Z^3 = 0 \tag{2.51}$$

Comparing Eq. (2.48) and Eq. (2.51) indicates that, for octopole superposition, the beat envelope equation and the slow flow are identical.

We next investigate the two equations (ours, and Sudakov's) for the case of hexapole superposition. Eq. (B7) in Sudakov (2001) which represents the beat envelope for hexapole superposition is

$$\frac{d^2Z}{d\xi^2} + 0.8873\,(q_0 - q)Z + 12.692\,\alpha_3^2 Z^3 = 0. \tag{2.52}$$

Following the procedure adopted for octopole nonlinearity and substituting $\bar{h} = \frac{3}{2\sqrt{\epsilon}}\left(\frac{r_0}{z_0}\right)$ in the slow flow, Eq. (2.34) with only hexapole superposition can be transformed to

$$\frac{d^2Z}{d\xi^2} + 0.8873\,(q_0 - q)\,Z + 7.1693\alpha_3^2\,Z^3 = 0. \tag{2.53}$$

It is observed that the coefficient of $\alpha_3^2\,Z^3$ in Eqs. (2.52) and (2.53) differ significantly. We now verify the correctness of the coefficients by comparing the solutions of the two equations with the solution of the original equation (Eq. (B1)) in Sudakov (2001) with hexapole superposition, which is

$$\frac{d^2u}{d\xi^2} + 2q\cos(2\xi)u = -q\cos(2\xi)\,3\,\alpha_3\,u^2. \tag{2.54}$$

These equations are integrated using the ODE45 routine of MATLAB with tolerance values of 10^{-10}. The amplitude obtained from the transformed slow flow (Eq. (2.53)), shown as a heavy line in Fig. 2.11, follows the solution of Eq. (2.46) very closely, while the amplitude from the beat envelope equation of Sudakov (2001), Eq. (2.52), shown as a dash line in Fig. 2.11, shows an error in the numerical term reported in Sudakov (2001).

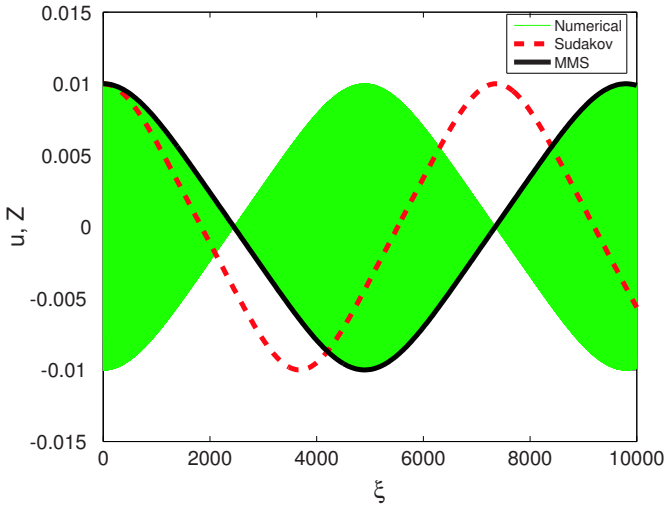

Figure 2.11: Comparison between amplitude obtained by (Eq. (2.53)) and Eq. (2.52) for $\alpha_3 = 0.02828$ (4% hexapole), $q = q_0 = 0.908046$, $u(0) = 0.01, \dot{u}(0) = 0, Z(0) = 0.01, \dot{Z}(0) = 0$.

2.6.5 Initial condition calculation

We describe a procedure to obtain initial conditions for Eq. (2.34), correct up to $\mathcal{O}(\sqrt{\epsilon})$, from the initial conditions used to integrate Eq. (2.9).

We assume $X(0) = X_0(0)$. Since $X_0 = A(T_1)\,\xi_1(T_0)$, we have

$$X_0(0) = A(T_1)\,\xi_1(0).$$

From the expression for X_0 obtained from MAPLE, we have $\xi_1(0) = 1.105$. Therefore, the initial condition for A is

$$A(0) = \frac{X_0(0)}{1.105} + \mathcal{O}(\sqrt{\epsilon}) = \frac{X(0)}{1.105} + \mathcal{O}(\sqrt{\epsilon}).$$

We also have

$$\begin{aligned} \dot{X}(0) &= \dot{X}_0(0) + \sqrt{\epsilon}\,\dot{X}_1(0) + \mathcal{O}(\epsilon) \\ &= \xi_1(0)\,\dot{A}(0) + \sqrt{\epsilon}\,\frac{\partial X_1}{\partial T_0} + \mathcal{O}(\epsilon). \end{aligned} \tag{2.55}$$

From our solution (MAPLE), we have

$$\frac{\partial X_1}{\partial T_0} = -1.7244\frac{\partial A}{\partial T_1}.$$

Substituting the above in Eq. (2.34), we get

$$\dot{A}(0) = \frac{\dot{X}(0)}{-0.6193} + \mathcal{O}(\epsilon).$$

Note that some small errors remain for nonzero ϵ, in light of which some small adjustments in initial conditions are allowed to obtain better fits.

Chapter 3

Motional coherence during resonance ejection of ions from Paul traps

3.1 Introduction

In this chapter we study the dependence of resolution on the scan direction in resonance ejection experiments in Paul traps with stretched geometry and in the presence of a buffer gas. In particular, we show how a forward scan direction *constrains* the pre-ejection dynamical states of the ion so as to yield a coherent motion which in turn leads to good resolution, and how a lack of this constraint results in poor resolution spectra in the reverse scan.

Ions of an analyte gas which are confined within the cavity of the three electrode geometry Paul trap mass analyzer (consisting of a ring electrode and two end cap electrodes) oscillate at their secular frequencies, ω_{0u}, in the axial and radial directions. The secular frequencies can be computed by the expression (March and Hughes, 1989; March, 1992)

$$\omega_{0u} = \frac{\beta_u \Omega}{2} \tag{3.1}$$

where u refers to the axial (z) or radial (r) directions, Ω is the angular frequency of the rf drive (applied across the central ring and the two grounded end cap electrodes) and β_u is a parameter related to the Mathieu parameters a_u and q_u. β_u can be obtained using an implicit continuous fraction relationship (March and Hughes, 1989) or more simply, when $q_u < 0.4$, by the expression (Dawson, 1976)

$$\beta_u^2 = a_u + \frac{q_u^2}{2} \tag{3.2}$$

within the pseudopotential well approximation.

In resonance ejection experiments, a fixed frequency ac excitation having sufficient amplitude is applied across the end cap electrodes (Fulford et al., 1980; March et al., 1990a; March et al., 1990b). To resonantly eject the ions from the trap, the secular frequency of the ions is brought into resonance with the fixed frequency excitation by varying the amplitude of the rf drive. In the mass spectrometry literature, increasing the rf amplitude to bring ion secular frequency into resonance with the ac excitation is

referred to as the *forward* scan experiment, and decreasing the rf amplitude is referred to as the *reverse* scan experiment (Goeringer et al., 1992; Williams et al., 1994).

Mass spectra obtained by resonance ejection in stretched geometry traps, in the presence of buffer gas, are known to have high resolution in forward scan experiments and relatively poor resolution in reverse scan experiments (Williams et al., 1994). A few theoretical studies in the literature have focussed on understanding the dependence of resolution on experimental parameters. Goeringer et al. (1992) developed relations for line width as a function of mass, scan rate and bath gas pressure. They modelled the system as a driven harmonic oscillator with damping. Arnold et al. (1994), using a similar expression, derived a relationship for the maximum possible resolution at high ion mass-to-charge ratio. Finally, Makarov (1996) used a forced, damped Duffing oscillator with positive cubic nonlinearity (corresponding to the stretched trap geometry) and he utilized Mitropol'skii's asymptotic technique (Mitropol'skii, 1965) to obtain slow flow equations. The fixed points of these equations were used to generate a resonance curve, and a study of that curve, along with detailed numerical simulations, was used to understand resolution and to obtain expressions for the same.

It is at this point that the study in this Chapter hopes to contribute. Like Makarov (1996), we too model the system to consist of positive octopole nonlinearity, damping and forcing and we consider ion motion to be within the pseudopotential well approximation regime where $q_z < 0.4$. We have taken up for investigation the dependence of resolution on the scan direction through a study of ion dynamics in the neighborhood of resonance. We will demonstrate that the observed resolution in the two directions can be attributed to the constraints on the pre-ejection initial conditions that ions can possess in the forward and reverse scan. It will be seen that coherence of ion motion in the forward scan and the absence of coherence in the reverse scan results in the observation of differing resolutions in the two directions.

In comparison to Makarov's work, ours may be viewed as addressing the following questions. How and when are studies based on the resonance curve valid in the presence of transient motion? How do damping, scan rate and scan direction affect this validity? What are the *mechanisms* responsible for the differential resolutions observed in the forward and reverse scan experiments? In particular, we use phase portraits of the slow flow to investigate these questions, thereby obtaining a qualitative understanding that continues beyond Makarov's treatment. Finally, full, numerical simulations will bear out the validity of the insight obtained from our phase portraits.

3.2 Equation of motion

The equation of motion of ions in the axial direction in a Paul trap with positive octopole field superposition, damping and dipolar excitation, within the psuedopotential well approximation, is given by (Sevugarajan and Menon, 2001)

$$\frac{d^2z}{dt^2} + c\frac{dz}{dt} + \omega_{0z}^2 z + \frac{8f}{r_0^2}\omega_{0z}^2 z^3 = -F_s \cos\omega t \tag{3.3}$$

where z is the motion of the ion in the axial direction, t is the time, c is the damping coefficient (which arises on account of helium bath gas), f is the ratio of the weight of octopole superposition with that of quadrupole superposition, r_0 is the radius of the trap, ω_{0z} is the secular frequency of the ion in the axial direction, ω is the frequency of the dipolar excitation and

$$F_s = \frac{eA_1V_s}{mr_0} \tag{3.4}$$

where e is the charge of electron, m is the mass of the ion, A_1 is the weight of the dipole component in the field and V_s is the amplitude of the ac dipolar excitation.

In Eq. (3.4) we have used the viscous drag model for damping proposed by Goeringer et al. (1992) which has the form

$$c = \frac{m_n}{m+m_n}\frac{p}{kT_b}\frac{e}{2\varepsilon_0}\sqrt{\alpha\frac{m+m_n}{mm_n}}$$

where m_n is the mass of the bath gas, $\alpha = 0.22 \times 10^{-40}$ Fm^2 is the polarizability of the bath gas, $\varepsilon_0 = 8.854 \times 10^{-12}$ F/m is the permittivity of free space, T_b is the temperature, p is the pressure of the bath gas in Pascal and k is the Boltzmann constant.

Use of this model is supported by the observation of Major and Dehmelt (1968) where it has been recommended that the viscous drag model could be used when the mass of the ion is much larger than that of the neutral gas. However, a recent study by Plass et al. (2003) has questioned the validity of this model in the context of typical commercial ion traps and has instead suggested that an elastic collision model would be more appropriate for predicting ion behavior. While, for the purpose of individually accurate predictions, we appreciate the practical point made by Plass et al. (2003), we note that analytically incorporating the effect of random infrequent collisions poses a challenge beyond the scope of this investigation.

It needs to be emphasized that in traditional resonance ejection experiments ω in Eq. (3.3) is in fact kept constant, and what varies when the rf amplitude is ramped is ω_{0z}. In order to modify Eq. (3.3) to the conventional form (in which the frequency of the forcing function is varied) we introduce dimensionless parameters $\tau = \omega_{0z}t$ and $\bar{z} = (z/r_0)$ and

we obtain

$$\frac{d^2\bar{z}}{d\tau^2} + 2\mu\frac{d\bar{z}}{d\tau} + \bar{z} + \alpha_3\bar{z}^3 = F\cos\nu\tau \tag{3.5}$$

where

$$\mu = \frac{c}{2\omega_{0z}} \tag{3.6}$$

$$\alpha_3 = 8f \tag{3.7}$$

$$F = \frac{F_s}{\omega_{0z}^2 r_0} \tag{3.8}$$

$$\nu = \frac{\omega}{\omega_{0z}}. \tag{3.9}$$

In Eq. (3.5) the frequency of the forcing function, ν, is the ratio of the excitation frequency to the secular frequency. Thus, since ω (the forcing frequency in Eq. (3.3)) is held constant, *forward* scan experiments will result in *decreasing* ν and reverse scan experiments will cause ν to increase. α_3 is the coefficient of the cubic nonlinearity and its sign will determine the nature of the nonlinearity. In our study α_3 is always positive. From Eqs. (3.6) and (3.8), we note that the damping coefficient, μ, and the amplitude of the forcing term, F, will vary with the secular frequency, ω_{0z}.

The equation of motion of the ions in a Paul trap is described by the Mathieu equation (Dawson, 1976). In this study, however, we will be using the Duffing equation (Eq. (3.3)) which is valid in the Dehmelt approximation region corresponding to $q_z < 0.4$. As an aside, it will be instructive to understand how the original Mathieu equation responds to dipolar excitation within the Dehmelt approximation region. We will do this by examining escape velocity of ions at an arbitrarily chosen q_z by a method outlined in Abraham et al. (2004). This study will also give a flavor for the altered stability conditions experienced by the ions in the presence of dipolar excitation.

Figure 3.1 is a plot of the escape velocity versus q_z. The escape velocity plots have been generated by assuming an ideal Mathieu equation with an additional force term, the equation having the form

$$\frac{d^2z}{d\tau^2} + (a_z + 2q_z\cos 2\tau)z = F\cos\frac{2\omega}{\Omega}\tau. \tag{3.10}$$

The plots have been made along the $a_z = 0$ axis for an ion trap in which the central ring electrode has a radius of 7 mm. The drive frequency, Ω, has been assumed to be 1 MHz and dipolar excitation frequency, ω, has been fixed at 100 kHz corresponding to a q_z value of 0.2829. The initial position and velocity of the ions, in our simulations, have been chosen as 0 m and 0.0001 m/s, respectively. This initial velocity is sequentially incremented in our computations and maximum ion amplitude, for a specified integration time, is estimated. The velocity that causes ion amplitude to just reach the trap boundary

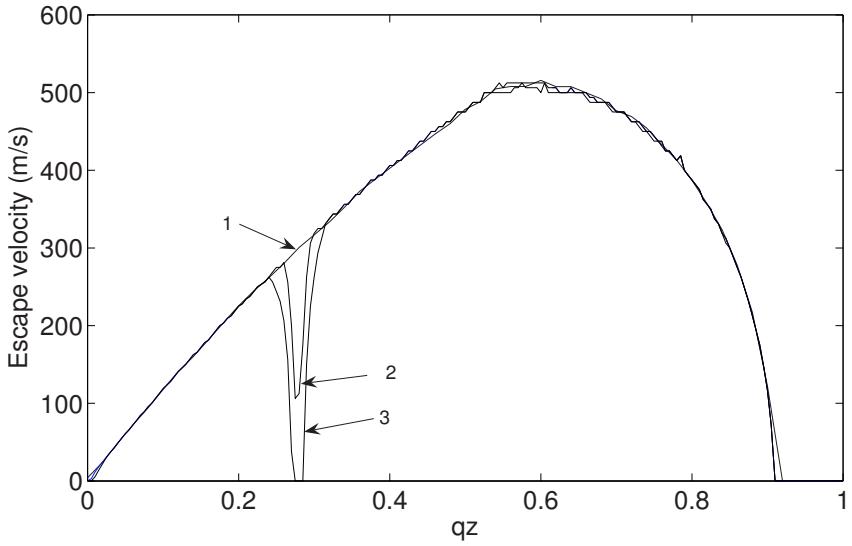

Figure 3.1: Escape velocity versus q_z. (1) unforced equation, (2) $V_s = 100$ mV, (3) $V_s = 200$ mV.

is taken to be the escape velocity of the ion at the chosen q_z (Abraham et al., 2004). The escape velocity plots in the absence of dipolar excitation (i.e., when $F = 0$), as well as in the presence of force, F, corresponding to dipolar excitation amplitude, V_s, of 100 mV and 200 mV, are presented in this figure. From Fig. 3.1 (curve 2), it can be noted that when an excitation voltage of 100mV is applied, there is a decrease in the escape velocity compared to the escape velocity in the absence of dipolar excitation (curve 1) at the selected q_z. When the excitation voltage is increased to 200 mV the escape velocity reduces to zero, implying that any ion encountering this condition will be unstable and will escape from the trap. Curve 2 corresponds to the condition generally used in collision induced dissociation studies and curve 3 is the condition maintained in resonance ejection experiments.

3.3 Analytical treatment

We now return to the Duffing equation (Eq. (3.5)). In order to study the response of the system to variations in damping, nonlinearity, forcing amplitude and frequency we need to derive an analytical expression which captures the dynamics of the system. In the context of the Duffing oscillator, several perturbation techniques have been explored in the mathematical literature. The Lindstedt - Poincaré method and the method of harmonic balance yield only steady state solutions and in our context will not provide an insight into ion dynamics. Two other techniques which can provide us both the transient

as well as steady state response are the method of averaging and method of multiple scales. In our study we have used the method of multiple scales (Nayfeh and Mook, 1979; Nayfeh, 1973; Hinch, 1991; Holmes, 1991) to derive the relevant slow flow equations. We assume that the coefficients μ, α_3, and F are small. To characterize the smallness of these coefficients, Eq. (3.5) may be modified as (Nayfeh and Mook, 1979)

$$\frac{d^2\bar{z}}{d\tau^2} + \bar{z} = \epsilon\left(-2\mu\frac{d\bar{z}}{d\tau} - \alpha_3\bar{z}^3 + F\cos\nu\tau\right) \tag{3.11}$$

where ϵ is a book keeping parameter. It is also assumed here that the perturbed frequency is close to the natural frequency of the ideal system (in our case $\nu = 1$) and can be represented as

$$\nu^2 = 1 + \epsilon\delta \tag{3.12}$$

where δ is a detuning parameter. In resonance ejection experiments when the rf amplitude is ramped, we may consider δ to be a function of slow time, T_1, and write

$$\delta = \delta(T_1) \tag{3.13}$$

where $T_1 = \epsilon\tau$ (discussed below).

Substituting Eq. (3.12) in Eq. (3.11) we get

$$\frac{d^2\bar{z}}{d\tau^2} + \nu^2\bar{z} = \epsilon\left(\delta\bar{z} - 2\mu\frac{d\bar{z}}{d\tau} - \alpha_3\bar{z}^3 + F\cos\nu\tau\right). \tag{3.14}$$

In the method of multiple scales we define

$$T_0 = \tau,\ T_1 = \epsilon\tau,\ \cdots$$

where T_0 is the fast time scale and $T_1,\ \cdots$ are slow time scales. We assume the solution to Eq. (3.14) to have the form

$$\bar{z}(\tau) = X(T_0, T_1, \cdots) \tag{3.15}$$

where X is assumed to have a form

$$X(T_0, T_1, \cdots) = X_0(T_0, T_1, \cdots) + \epsilon X_1(T_0, T_1, \cdots) + \cdots \tag{3.16}$$

The derivatives with respect to τ will become

$$\frac{d(.)}{d\tau} = \frac{\partial(.)}{\partial T_0} + \epsilon\frac{\partial(.)}{\partial T_1} + \mathcal{O}(\epsilon^2) \tag{3.17}$$

$$\frac{d^2(.)}{d\tau^2} = \frac{\partial^2(.)}{\partial T_0^2} + 2\epsilon\frac{\partial^2(.)}{\partial T_0\partial T_1} + \mathcal{O}(\epsilon^2). \tag{3.18}$$

Substituting Equations (3.16), (3.17), (3.18) in Equation (3.14) and expanding the cubic term, we obtain

$$\frac{\partial^2 X_0}{\partial T_0^2} + \nu^2 X_0 + \epsilon\Big[\frac{\partial^2 X_1}{\partial T_0^2} + \nu^2 X_1 + 2\frac{\partial^2 X_0}{\partial T_0 \partial T_1} - \delta\, X_0 + 2\mu\frac{\partial X_0}{\partial T_0} + \alpha_3\, X_0^3 - F\cos(\nu T_0)\Big] + \mathcal{O}(\epsilon^2) = 0. \tag{3.19}$$

Collecting the coefficients of ϵ^0, ϵ in Equation (3.19) we have

$$\frac{\partial^2 X_0}{\partial T_0^2} + \nu^2\, X_0 = 0. \tag{3.20}$$

$$\frac{\partial^2 X_1}{\partial T_0^2} + \nu^2 X_1 = -2\frac{\partial^2 X_0}{\partial T_0 \partial T_1} + \delta\, X_0 - 2\mu\frac{\partial X_0}{\partial T_0} - \alpha_3\, X_0^3 + F\cos(\nu T_0) \tag{3.21}$$

We consider the general solution to Equation (3.20) in the form

$$x_0 = A(T_1)\cos\nu\, T_0 + B(T_1)\sin\nu\, T_0 \tag{3.22}$$

where A and B are arbitrary functions of slow time, T_1. Substituting Equation (3.22) into Equation (3.21) we get

$$\begin{aligned}
\frac{\partial^2 X_1}{\partial {T_0}^2} + \nu^2 X_1 - 2\frac{dA}{dT_1}\sin(\nu\, T_0) + 2\frac{dB}{dT_1}\cos(\nu\, T_0) \\
-\delta\, A\, \cos(\nu\, T_0) - \delta\, B\, \sin(\nu\, T_0) - 2\mu\, A\, \sin(\nu T_0)\nu \\
+2\mu\, B\, \cos(\nu T_0)\nu + \frac{1}{4}\alpha_3 A^3\cos(3\nu T_0) - \frac{1}{4}\alpha_3 B^3\sin(3\nu T_0) \\
+\frac{3}{4}\alpha_3 A^3\cos(\nu T_0) + \frac{3}{4}\alpha_3 B^3\sin(\nu T_0) + \frac{3}{4}\alpha_3 A^2 B\sin(3\nu T_0) \\
-\frac{3}{4}\alpha_3 A B^2\cos(3\nu T_0) + \frac{3}{4}\alpha_3 A^2 B\sin(\nu T_0) \\
+\frac{3}{4}\alpha_3 A B^2\cos(\nu T_0) - F\cos(\nu T_0) \;=\; 0.
\end{aligned} \tag{3.23}$$

Equation (3.23) is a nonhomogeneous equation in X_1. The terms involving $\sin(\nu T_0)$ and $\cos(\nu T_0)$ will lead to secular terms (terms whose amplitude grows with time) in the particular solution. In order to eliminate the secular terms from the solution we set the coefficients of $\sin(\nu T_0)$ and $\cos(\nu T_0)$ to zero. When we do so we get the following equations which are the slow flow equations at $\mathcal{O}(\epsilon)$ as

$$\frac{dA}{dT_1} = \frac{1}{8\nu}(-8\mu A\nu - 4\delta(T_1)B + 3\alpha_3 A^2 B + 3\alpha_3 B^3) \tag{3.24}$$

$$\frac{dB}{dT_1} = \frac{1}{8\nu}(-8\mu B\nu + 4\delta(T_1)A - 3\alpha_3 AB^2 - 3\alpha_3 A^3 + 4F). \tag{3.25}$$

From Equation (3.17), we have

$$\dot{A} = \frac{dA}{d\tau} = \frac{\partial A}{\partial T_0} + \epsilon\frac{\partial A}{\partial T_1} + \mathcal{O}(\epsilon^2) \tag{3.26}$$

and

$$\dot{B} = \frac{dB}{d\tau} = \frac{\partial B}{\partial T_0} + \epsilon\frac{\partial B}{\partial T_1} + \mathcal{O}(\epsilon^2). \tag{3.27}$$

Since the A and B are not functions of T_0, and by putting $\epsilon = 1$ we get

$$\dot{A} = \frac{1}{8\nu}(-8\mu A\nu - 4\delta(\tau)B + 3\alpha_3 A^2 B + 3\alpha_3 B^3) \tag{3.28}$$

$$\dot{B} = \frac{1}{8\nu}(-8\mu B\nu + 4\delta(\tau)A - 3\alpha_3 AB^2 - 3\alpha_3 A^3 + 4F) \tag{3.29}$$

and

$$x \approx A\cos\nu\,\tau + B\sin\nu\,\tau. \tag{3.30}$$

Eqs. (3.28) and (3.29) are the slow flow equations from which we can determine the fixed points of the system. It can be observed that $\dot{A}$ and $\dot{B}$ are dependent on the damping (μ), nonlinearity (α_3) and forcing (F) as well as the detuning (δ). We will be using these equations to generate phase portraits to understand the mechanism of destabilization in resonance ejection experiments.

3.3.1 Numerical verification

The validity of the slow flow equations obtained above (Eqs. (3.28) and (3.29)) to describe the behavior of the original system will be verified by two calculations. In the first, for a given point on the phase portrait, slow changes in the amplitude predicted by the slow flow will be compared with the variation in the amplitude obtained by the integration of the original equation (Eq. (3.5)). In the second, we compare amplitude response curves obtained from the slow flow equations and the original equation.

The slow flow equations (Eqs. (3.28) and (3.29)) are two first order differential equations in the state variables A and B. The time evolution of the solution of the slow flow equations (which is related to the motion of ions) from any initial point can be plotted as a curve on the A-B phase plane and is called a trajectory. A number of such trajectories plotted together is called a phase portrait (Strogatz, 1994; Hilborn, 1994). To generate phase portraits we integrate the slow flow equations for a large number of arbitrarily chosen initial conditions and plot B against A in each case on the same graph.

Figure 3.2(a) presents the phase portrait obtained from the slow flow at $\nu = 1.2$ ($\delta = 0.44$) for an undamped condition for an ion of mass 78 Th, an excitation voltage

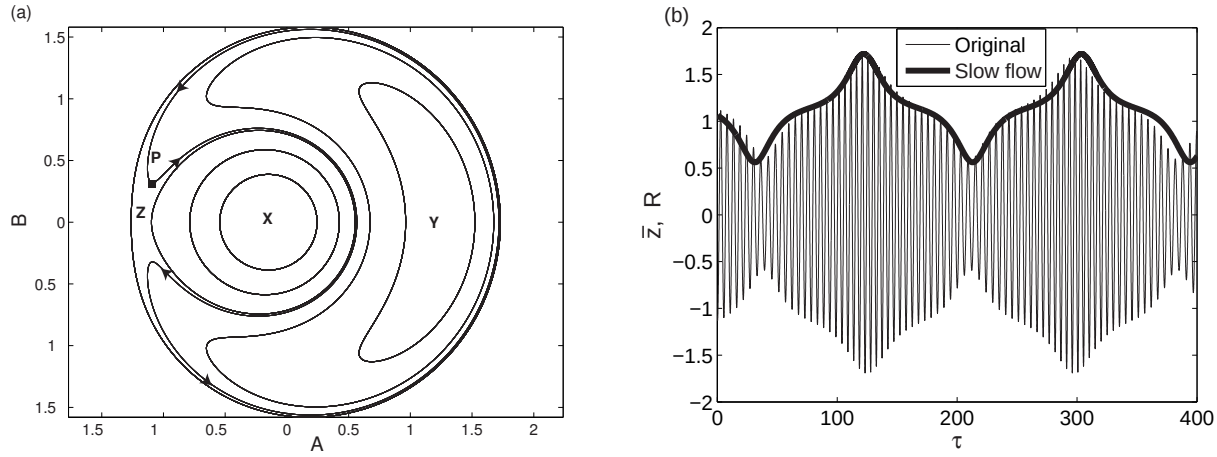

Figure 3.2: (a) Phase portrait of the system ((Eqs. (3.28) and (3.29)) at $\nu = 1.2$ ($\delta = 0.44$), $V_s = 500$ mV, $\alpha_3 = 0.4$, $\mu = 0$. (b) The time response from the original equation and amplitude from the slow flow for the initial condition corresponding to point P on the phase portrait.

amplitude of 500 mV and for +5% octopole (f) superposition. The slow flow equations are integrated repeatedly for several different initial conditions and phase portraits are generated by plotting A on the $x-$axis and B on the $y-$axis. We present this phase portrait in Fig. 3.2(a) which displays two stable equilibria (centers) marked X and Y, and an unstable equilibrium (saddle) marked Z.

For generating the time response plot (Fig. 3.2(b)) we choose initial conditions $A = -1.091$ and $B = 0.3146$ corresponding to the point P close to the saddle in Fig. 3.2(a). For plotting the time response of the original equation we use Eq. (3.30) to obtain the corresponding initial conditions as $\bar{z}(0) = -1.091$ and $\dot{\bar{z}}(0) = 0.3775$. From the phase portrait it can be seen that the trajectory first goes around the low amplitude solution before it swings around the larger amplitude solution. This behavior is reflected in the time response plots in Fig. 3.2(b). In Fig. 3.2(b) we also superimpose the variation in amplitude, $R = \sqrt{A^2 + B^2}$, obtained by integrating the slow flow equations, as a heavy line. This comparison bears out the validity of the slow flow in approximating the behavior of the original equation.

Note that although the analysis is formally valid for very small δ and α_3, the final match is good even for somewhat large values like $\delta = 0.44$, $\alpha_3 = 0.4$. For smaller values of these parameters, the match will be better.

The phase portrait generated in Fig. 3.2(a) was for an undamped system and consequently the stable solutions appear as centers in the $A - B$ phase space of Eqs. (3.28) and (3.29). In the presence of a buffer gas (damping), when $\mu > 0$, the trajectories in the

$A - B$ phase space will eventually settle to one of the fixed points, as shown in Fig. 3.3.

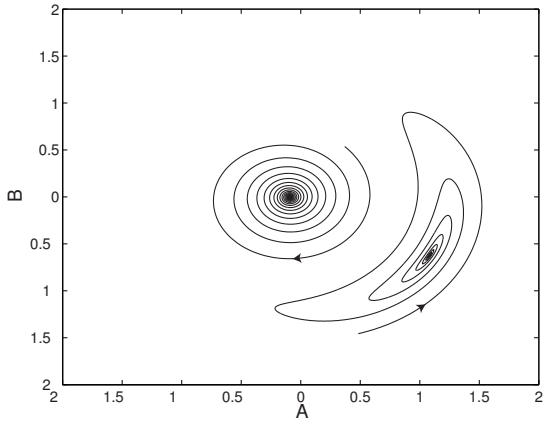

Figure 3.3: Phase trajectories of slow flow equations generated for mass 78 Th, $V_s = 500$ mV, pressure = 1 Pascal and +5% octopole superposition at $\nu = 1.2$.

A second verification of the accuracy of the slow flow to describe our original system is studied through amplitude-response curves. An amplitude-response curve obtained from the original nonlinear equation (Eq. (3.5)) is compared with the curve obtained from the slow flow (Eqs. (3.28) and (3.29)) in Fig. 3.4. These curves are generated for an ion of mass 78 Th, pressure of 0.1 Pascal, an excitation voltage amplitude of 500 mV and for +5% octopole superposition. The amplitude-response curve of the original equation is generated by a simple numerical arc-length based continuation method used by Nandakumar and Chatterjee (2005a) and is shown by the continuous curve. For obtaining the amplitudes from the slow flow we use $R = \sqrt{A^2 + B^2}$, where A and B are equilibrium values of the first order slow flow equations for different values of ν. The values obtained are indicated by '$\star$'. The trap boundary is indicated by a horizontal line at $R \approx 0.71$ corresponding to z_0/r_0. The amplitudes determined from the slow flow equations closely match those obtained from the original equation, validating the slow flow.

These curves also display the well known jump event observed in systems with cubic nonlinearities (McLachlan, 1954; Landau and Lifshitz, 1976; Nayfeh and Mook, 1979). Jumps are known to occur at the vertical tangents to these curves. In the context of resonance ejection experiments, in the forward scan, at the vertical tangent in the neighborhood of M (Fig. 3.4), the solution jumps from the lower curve towards the amplitude determined by the upper curve (this has also been pointed out by Makarov (1996)) and ions get detected at the trap boundary at this jump point. In reverse scan experiments, however, ion detection occurs when the ion amplitude corresponding to the upper curve reaches the trap boundary and here there is no sudden change in ion amplitude as it happens in the forward scan experiment.

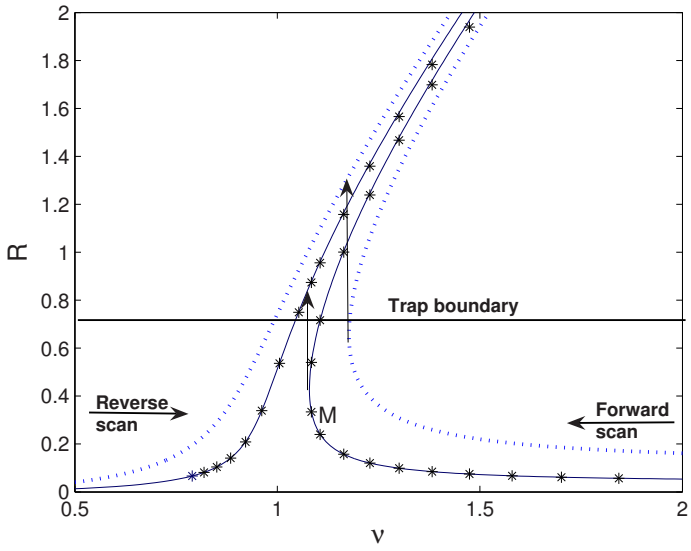

Figure 3.4: Amplitude-response curve of an ion of mass 78 Th with pressure= 0.1 Pascal and +5% octopole superposition. (—) for V_s = 500 mV, (....) for V_s = 1.5 V. (*) denotes the amplitude obtained from the slow flow equations.

Also shown in Fig. 3.4 is the amplitude response curve for larger V_s, to demonstrate that the magnitude of the jump depends on the applied excitation voltage V_s. A larger V_s results in a larger jump (see dotted curve in Fig. 3.4, made for $V_s = 1.5$ V). Since very small V_s will not make the ion amplitude jump across the trap boundary, a minimum V_s is required for obtaining a spectrum in the forward scan.

3.4 Results and discussion

It needs to be pointed out that Eq. (3.5), the Duffing equation, was developed using the pseudopotential well approximation which is valid only for $q_z < 0.4$. In that sense the results we present below are useful only within this range. However, since the discussion we present is *qualitative* in nature we hope this may provide an insight into resonant ion dynamics even at higher q_z values.

As an aside, we point out that the Duffing equation has on occasion been seen to provide useful *quantitative* information at values of q_z greater than 0.4. An example of this is the study of Makarov (1996) who used a Duffing equation to develop expressions for line width and resolution which provided very good matches with experimental results at $q_z = 0.86$.

3.4.1 Phase portraits

We now turn to investigate coherence. For this, we first present the phase portraits derived from the slow flow equations in the region close to resonance. Figure 5 presents the phase portraits at two different values of ν on the amplitude response curve. These plots have been made for a mass of 78 Th, excitation voltage amplitude of 500 mV and for +5% octopole superposition in the absence of damping.

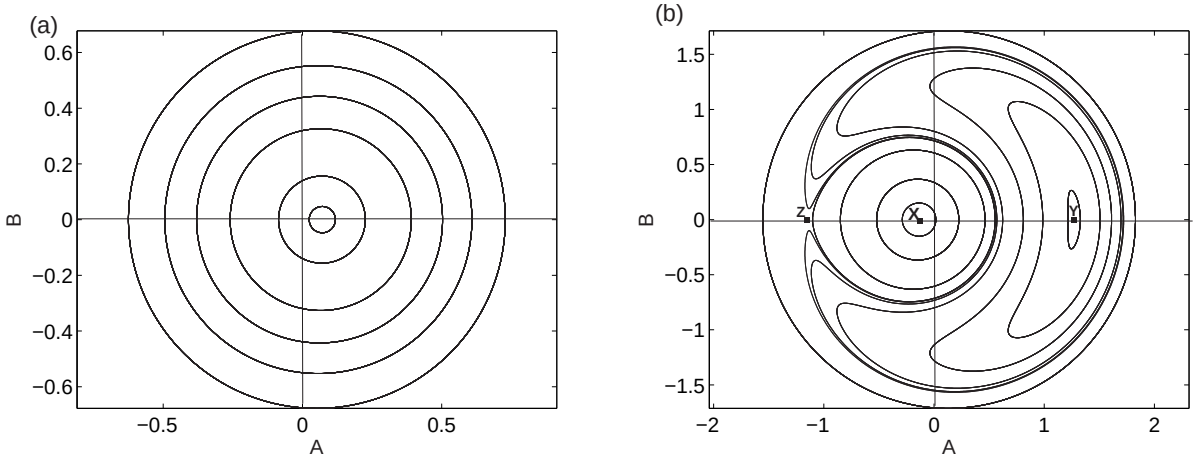

Figure 3.5: Phase portraits of the system ((Eqs. (3.28) and (3.29)) for $V_s = 500$ mV, $\alpha_3 = 0.4$, $\mu = 0$ (no damping) at (a) $\nu = 0.8$ ($\delta = -0.36$) (b) $\nu = 1.2$ ($\delta = 0.44$).

Figure 3.5(a) has been plotted for $\nu = 0.8$ corresponding to $\delta = -0.36$. At this detuning, there exists only one (stable) equilibrium point[1] corresponding to the upper curve of the amplitude response plot. Figure 3.5(b) has been plotted for $\nu = 1.2$ corresponding to $\delta = 0.44$. At this detuning, three equilibrium points exist, of which two are stable and the third is unstable. The phase portraits for better understanding, cover amplitudes much larger than the trap dimension. Actually, for Fig. 3.5(b), the trap physically restricts ion motion amplitudes and so all ion motions are close to the point X. Similarly for Fig. 3.5(a), ion motion is close to the unique periodic solution. In the presence of damping, moreover, all solutions will settle on to the respective equilibrium points (periodic solutions in terms of the original variable $\bar{z}$).

Six more thumb-nail phase portraits are presented in Fig. 3.6 corresponding to different ν values. Of these, (a) and (b) correspond to regions where the value of ν is smaller than the ν value at the jump point; (c) corresponds to ν value at the jump point and (d), (e) and (f) are the plots for higher ν values. We emphasize that these phase portraits are for zero damping as well as six independently fixed values of δ.

[1] An equilibrium of the slow flow represents a periodic solution in the original z variable.

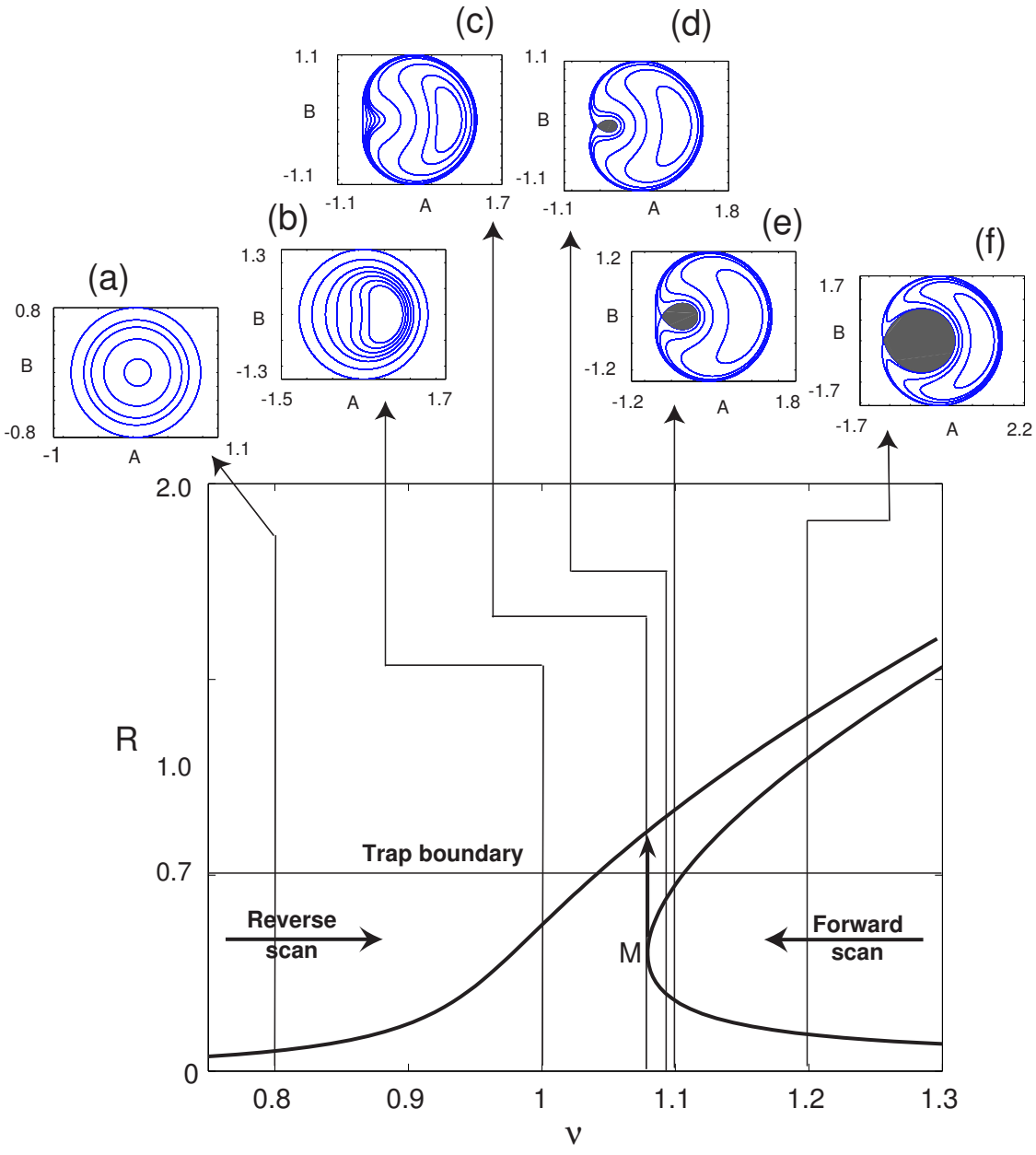

Figure 3.6: Amplitude-response plots and phase portraits plotted at (a) $\nu = 0.8$, (b) $\nu = 1.0$, (c) $\nu = 1.08$, (d) $\nu = 1.09$, (e) $\nu = 1.1$, (f) $\nu = 1.2$.

In the phase portraits, at large ν there are three equilibrium points. We have shaded an area of the phase space enclosed by a homoclinic orbit. All trajectories in this area are closed curves representing periodic solutions in A and B (and periodically modulated solutions in the original variable z). In the presence of damping, essentially all of these solutions will settle to equilibrium solution in the middle of the shaded region (amplitude corresponding to the lower curve of the amplitude response plot). As δ varies quasistatically, from a high value to lower values (implying ν varies from higher values to lower values), the area of the shaded region decreases. At the jump point, the area of the shaded region has gone to zero and for an infinitesimally smaller δ the phase portrait displays a single periodic solution with an amplitude corresponding to the upper curve of the amplitude response plot.

In contrast, phase portraits (a) and (b) in Fig. 3.6 do not display any qualitative change in structure.

3.4.2 Mass resolution

There are some interesting characteristics associated with the jump point which provide an insight into the improved resolution observed in forward scan experiments. One feature has been presented in the discussion above in relation to Fig. 6, namely, at the jump point ions of the same mass, having different initial conditions at the start of the experiment, have the same amplitude and these ions eject from the trap simultaneously. Another feature of this curve can be seen in Fig. 3.7 which has been plotted for identical experimental conditions for two different masses, 78 Th and 79 Th. In Fig. 3.7(a) the frequency response curves appear to be indistinguishable but the clear separation of the curves is evident in Fig. 3.7(b) which shows a magnified view of a portion near the jump point of Fig. 3.7(a). Here, the jump points corresponding to the two masses are labelled J_{78} and J_{79}. This separation determines the ultimate resolution achievable by the mass analyzer. In practice, however, the resolution will be determined by the actual spread in amplitude of the two adjacent masses at the time of jump and, this in turn, will be influenced for a given pressure of the bath gas, by the scan rate.

3.4.3 Damping, scan rate, and coherence

So far, we have studied the phase portrait with δ = constant (no scan rate) and in the absence of damping. Consider, now, the effect of some damping: it merely causes trajectories within the shaded regions drawn in Fig. 3.6 to collapse on to the equilibrium point (we ignore delicate issues in resolving what happens to trajectories very close to the original homoclininc orbit, as borderline cases will at most involve a few ions only). As

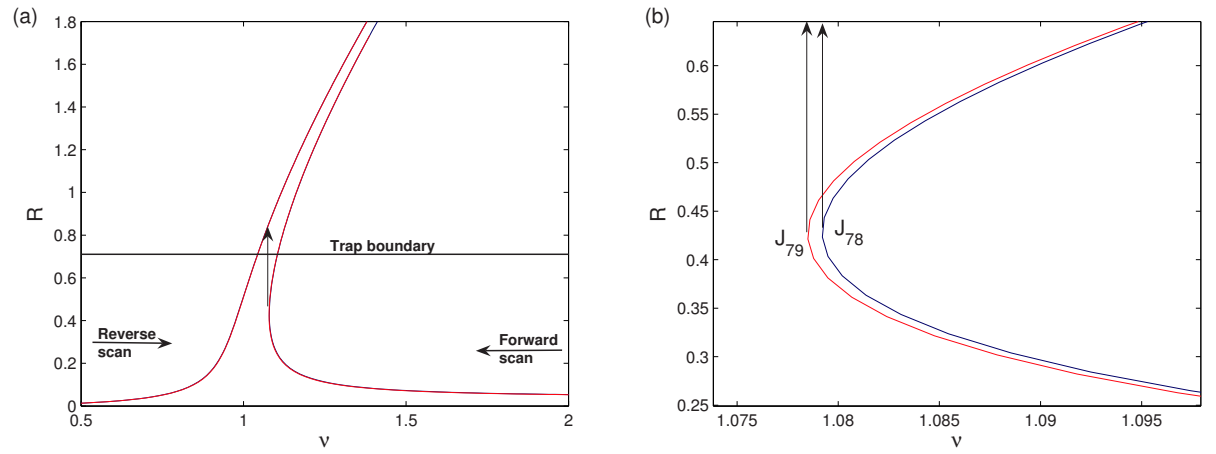

Figure 3.7: (a) Amplitude-response curves of ions of mass 78 Th and 79 Th with pressure= 0.1 Pascal and +5% octopole superposition and $V_s = 500$ mV. (b) Magnified region close to the jump point

will be seen in the numerical simulations below, the magnitude of damping will determine this rate of collapse and thus will influence resolution in both the forward as well as reverse directions.

Let us now turn to scan rate. Suppose, in addition to damping, there is a very slow but nonzero scan rate. The damped trajectories still have enough time to collapse on to the equilibrium point and then quasistatically follow the equilibrium point as it moves along the appropriate branch of the amplitude response curve (upper or lower, depending on whether it is a reverse or forward scan, respectively). These trajectories therefore remain effectively phase locked with the forcing; all of them have effectively the same amplitude and phase, i.e., the ion motions will be *coherent*; and all are ejected and detected virtually at the same instant, giving good resolution in the spectrum in both directions. However, in traditional resonance ejection experiments such extremely slow scan rates have not been used since very slow scan rates will result in large time delays before detection of high mass ions and this will lead to deterioration of the quality of the spectrum.

Imagine, therefore, we increase the scan rate. There is now a more complex dynamics associated with the ion trajectories (as may be seen by studying the slow flow with a time-varying δ, something we avoid here to maintain focus on the issue of primary interest). Analytically elucidating this complex dynamics would require sophisticated analysis not attempted here; rather, we will use direct numerical integration to elucidate these phenomena in the next Section. Here, we present a simple linearized analysis near the periodic solutions which shows that the approach towards the coherent motion is faster during forward scan compared to reverse scan.

Defining $\Theta = \begin{pmatrix} A \\ B \end{pmatrix}$, Eqs. (3.28) and (3.29) can be written as

$$\dot{\Theta} = f(\Theta) \tag{3.31}$$

where

$$f(\Theta) = \begin{pmatrix} f_1 \\ f_2 \end{pmatrix} = \begin{pmatrix} \frac{1}{8\nu}(-8\mu A\nu - 4\delta(\tau)B + 3\alpha_3 A^2 B + 3\alpha_3 B^3) \\ \\ \frac{1}{8\nu}(-8\mu B\nu + 4\delta(\tau)A - 3\alpha_3 AB^2 - 3\alpha_3 A^3 + 4F) \end{pmatrix} \tag{3.32}$$

Let $\Theta^* = \begin{pmatrix} A^* \\ B^* \end{pmatrix}$ be a fixed point (with δ held constant) of the above system, i.e., $f(\Theta^*) = 0$. For any perturbation about the fixed point Θ^*, $\Theta = \Theta^* + \xi$, we have (Guckenheimer and Holmes, 1983)

$$\dot{\xi} \approx J\xi \tag{3.33}$$

where J is the Jacobian of $f(\Theta)$ given by

$$J = \begin{pmatrix} \frac{\partial f_1}{\partial A} & \frac{\partial f_1}{\partial B} \\ \\ \frac{\partial f_2}{\partial A} & \frac{\partial f_2}{\partial B} \end{pmatrix} \tag{3.34}$$

From Eq. (3.32) we get the Jacobian at Θ^* as

$$J = \frac{1}{8\nu}\begin{pmatrix} -8\mu\nu + 6\alpha_3 A^* B^* & -4\delta + 9\alpha_3 B^{*2} + 3\alpha_3 A^{*2} \\ \\ 4\delta - 3\alpha_3 B^{*2} - 9\alpha_3 A^{*2} & -8\mu\nu - 6\alpha_3 A^* B^* \end{pmatrix} \tag{3.35}$$

The real part of the eigenvalues of the Jacobian will determine the rate of approach of (A, B) to the fixed point (A^*, B^*). The characteristic equation of J is

$$\lambda^2 - tr(J)\lambda + det(J) = 0 \tag{3.36}$$

and so

$$\lambda = \frac{tr(J) \pm \sqrt{(tr(J))^2 - 4det(J)}}{2}. \tag{3.37}$$

Assuming low damping, solutions will spiral into (A^*, B^*), therefore λ is complex. The real part of λ is given by

$$\frac{tr(J)}{2} = -\frac{16\mu\nu}{16\nu} = -\mu \tag{3.38}$$

But

$$\mu = \frac{c}{2\omega_{0z}} = \frac{c\nu}{\omega} \tag{3.39}$$

Since c and ω are constants in Eq. (3.39), the rate of approach of amplitude of ion motion to the fixed point (A^*, B^*), is proportional to ν. In the forward and reverse scan experiments, the ν values are close to each other, with ν being larger for the forward scan case. However, the small difference in ν values is amplified by the larger times involved (many cycles of forcing). Therefore, damping-induced coherence is greater for the forward scan.

Finally, consider the case where the scan rate is high enough to be dynamically far more relevant than the damping. The quasistatic behavior referred to earlier eventually disappears. In such cases, phase locking cannot be expected even in an approximate sense and even in the forward scan direction there will be loss of coherence in ion motion. This occurs primarily due to rate of decrease of amplitude due to damping being much smaller than the scan rate thus resulting in ions not having sufficient time to settle to the stable solution. This, too, will be numerically studied below.

3.4.4 Numerical simulations

The numerical integration of the original equation (Eq. (3.5)) has been carried out to study the effect that damping and scan rate have on the resolution in the two scan directions. This study will investigate the response of our system for two initial conditions, viz., $(\bar{z}(0), \dot{\bar{z}}(0))$ corresponding to (0.1, 0) and (0.25, 0). In all the plots the y-axis corresponds to the nondimensionalized amplitude. Ejection will occur at $\bar{z} \approx 0.71$ on this scale. Three damping conditions have been considered and the scan rate is introduced by expressing ν as

$$\nu = \nu_0 + \gamma\tau \tag{3.40}$$

where ν_0 is the starting value of ν, γ is a dimensionless number akin to the scan rate and τ is dimensionless time. For forward scan the sign of γ is negative and we fix ν_0 as 3 and for reverse scan γ is positive and ν_0 is chosen as 0.1.

The abscissa in these plots correspond to $\nu_0 + 2\gamma\tau$. We briefly explain this choice since in the amplitude response plots in Figs. 3.4 and 3.6, the abscissa is ν. To justify this change of independent variable we think of the forcing term $F\cos(\nu\tau)$ in Eq. (3.5) as $F\cos(\theta)$. Then the abscissa of the amplitude response curve should really be $\dot{\theta}$, i.e., the rate of change of phase in the forcing itself. During a scan, we have

$$\nu = \nu_0 + \gamma\tau; \quad \dot{\nu} = \gamma, \tag{3.41}$$

and so

$$\dot{\theta} = \nu + \dot{\nu}\tau = \nu_0 + 2\gamma\tau. \tag{3.42}$$

We have, therefore, plotted $\nu_0 + 2\gamma\tau$ on the abscissa of the time response plots.

We first investigate the effect of damping. For this we fix γ at 0.0005. Figures 3.8 and 3.9 are plots for forward and reverse scan, respectively, for no damping. Figures 3.10 and 3.11 and Figs. 11 and 12 are the plots for damping corresponding to He bath gas pressure of 0.1 Pascal and 1 Pascal, respectively. In all these figures subplot (a) corresponds to initial condition (0.1, 0), subplot (b) corresponds to initial condition (0.25, 0) and in subplot (c) we have provided the magnified portion of the plots in (a) and (b) where the amplitude of ion motion crosses the trap boundary. The traces shown in Figs. 3.9, 3.11 and 3.12 for large initial conditions are similar to those presented by Franzen (1993) to explain ejection delays caused by multipole superposition in mass selective ejection at the $\beta_z = 1$ stability boundary.

In the absence of damping, trajectories in Fig. 3.8 and 3.9 display no coherence in both forward as well as reverse scan. Ions with two different initial conditions, at the start of the experiment, encounter the trap boundary at different values of ν. The situation is dramatically altered in the forward scan in the presence of 0.1 Pascal He bath gas pressure. As anticipated from earlier discussions, motion of ions of two different initial conditions fall in step, and they have coherent motion at the approach to the trap boundary. This is demonstrated by the indistinguishable trajectories of the two different initial conditions shown in Fig. 3.10(c). In the reverse scan, at this pressure, there continues to be lack of coherence as seen in Fig. 3.11(c). When the He bath gas pressure is further increased to 1 Pascal, ion motion in the forward scan continues to be coherent. Although the ion motion in the reverse scan displays greater coherence at 1 Pascal when compared to the 0.1 Pascal case, there is still some separation in the trajectories corresponding to the two initial conditions as seen in Fig. 3.12.

To investigate the effect of scan rate, we consider increased scan rate of $\gamma = 0.0051$, corresponding to He bath gas pressure of 0.1 Pascal. The time trajectories are presented in Fig. 3.13. From a comparison of Fig. 3.10 (which was plotted for $\gamma = 0.0005$) and Fig. 3.13 it is evident that increasing scan rate has the effect of destroying coherence in the forward direction as has been suggested in our earlier discussion.

3.5 Concluding remarks

The motivation of this chapter was to understand constraints on the pre-ejection dynamics of ions in the forward and reverse scan resonance ejection experiments. Both analytical and numerical computations have been carried out to understand the cause for the variation in resolution of mass spectra observed in the two scan directions. For our analytical study, ion motion was modelled as a damped, driven Duffing oscillator with positive cubic nonlinearity and, using the method of multiple scales, slow flow equations were derived. These slow flow equations were validated using numerical simulations. Numerical studies

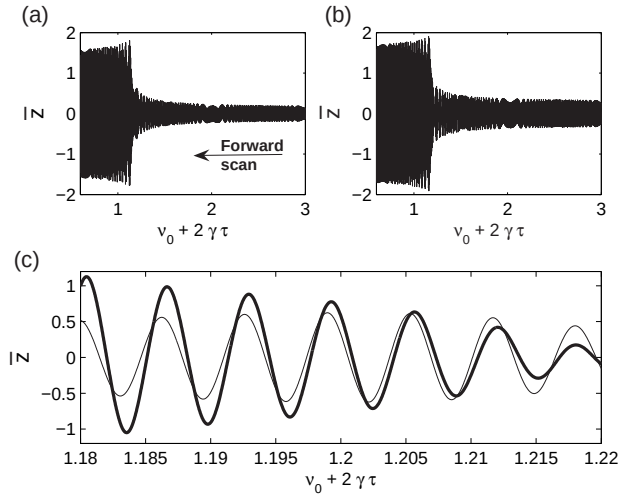

Figure 3.8: Time trajectories in the forward scan for initial conditions (a) (0.1, 0) and (b) (0.25, 0), in the absence of damping. $\nu_0 = 3$, $\gamma = -0.0005$. The trajectories for the two initial conditions in the vicinity of the trap boundary ($\bar{z} \approx 0.7$) are presented in (c). Light curve corresponds to initial condition (0.1, 0) and dark curve corresponds to initial condition (0.25, 0).

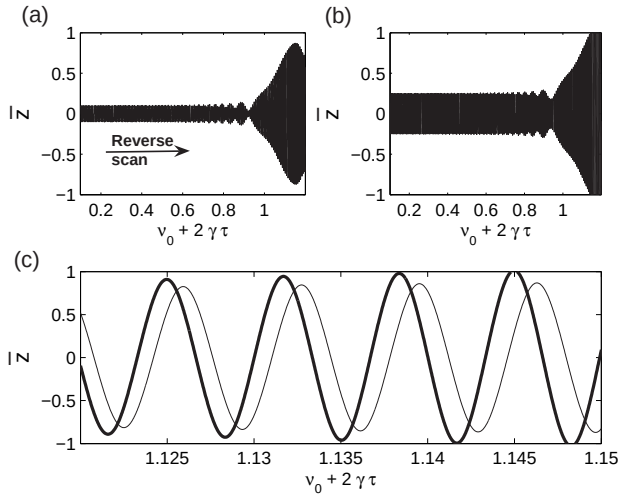

Figure 3.9: Time trajectories in the reverse scan for initial conditions (a) (0.1, 0) and (b) (0.25, 0), in the absence of damping. $\nu_0 = 0.1$, $\gamma = 0.0005$. The trajectories for the two initial conditions in the vicinity of the trap boundary ($\bar{z} \approx 0.7$) are presented in (c). Light curve corresponds to initial condition (0.1, 0) and dark curve to initial condition (0.25, 0).

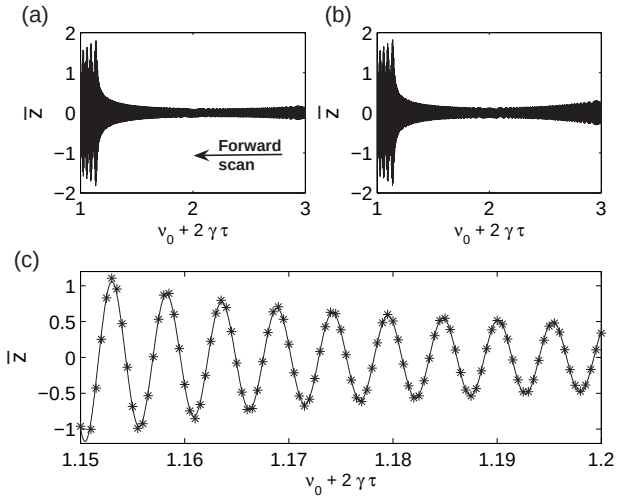

Figure 3.10: Time trajectories in the forward scan for initial conditions (a) (0.1, 0) and (b) (0.25, 0), He gas pressure 0.1 Pascal, $\nu_0 = 3$, $\gamma = -0.0005$. The trajectories for the two initial conditions in the vicinity of the trap boundary ($\bar{z} \approx 0.7$) are presented in (c). Continuous curve corresponds to initial condition (0.1, 0) and '*' to initial condition (0.25, 0).

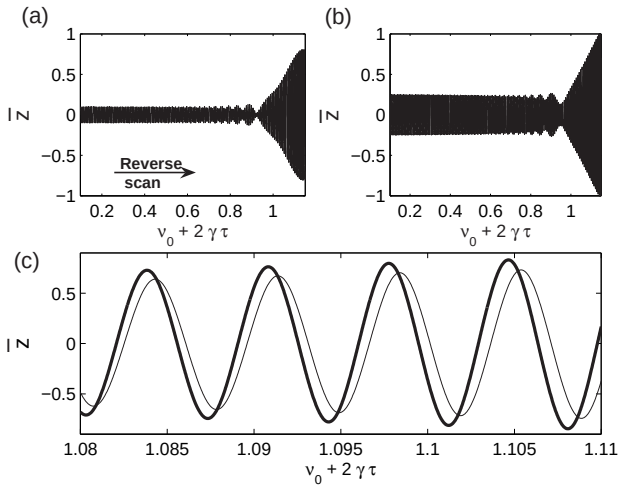

Figure 3.11: Time trajectories in the reverse scan for initial conditions (a) (0.1, 0) and (b) (0.25, 0), He gas pressure 0.1 Pascal, $\nu_0 = 0.1$, $\gamma = 0.0005$. The trajectories for the two initial conditions in the vicinity of the trap boundary ($\bar{z} \approx 0.7$) are presented in (c). Light curve corresponds to initial condition (0.1, 0) and dark curve to initial condition (0.25, 0).

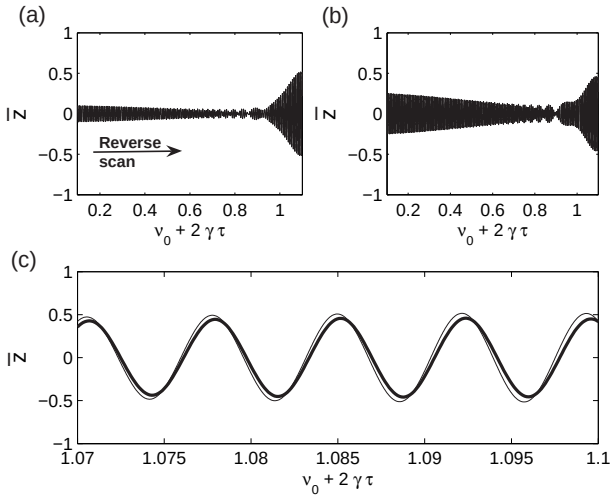

Figure 3.12: Time trajectories in the reverse scan for initial conditions (a) (0.1, 0) and (b) (0.25, 0), He gas pressure 1 Pascal, $\nu_0 = 0.1$, $\gamma = 0.0005$. The trajectories for the two initial conditions in the vicinity of the trap boundary ($\bar{z} \approx 0.7$) are presented in (c). Light curve corresponds to initial condition (0.1, 0) and dark curve to initial condition (0.25, 0).

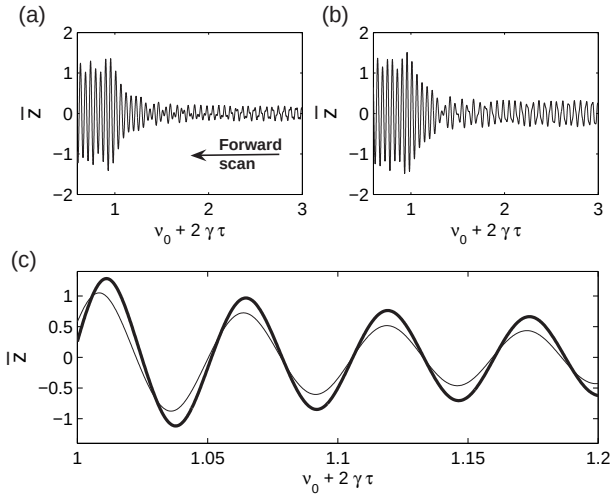

Figure 3.13: Time trajectories in the forward scan for initial conditions (a) (0.1, 0) and (b) (0.25, 0), He gas pressure 0.1 Pascal, $\nu_0 = 3$, $\gamma = -0.0051$. The trajectories for the two initial conditions in the vicinity of the trap boundary ($\bar{z} \approx 0.7$) are presented in (c). Light curve corresponds to initial condition (0.1, 0) and dark curve to initial condition (0.25, 0).

have also been carried out on the original Duffing equation to support our qualitative conclusions obtained from the phase portraits.

First confining attention to the amplitude-response curve (as done by Makarov (1996)) it was observed that the mechanisms of ion ejection in the two scan directions are different. In the forward scan experiment, as previously noted by Makarov, ejection occurs when the ions of a given mass encounter the jump point. At this point, a sudden change in amplitude of ions causes them to get ejected from the trap. In reverse scan experiment, we point out that ion ejection occurs not on account of any jump, but because ion amplitude grows steadily and reaches the trap boundary.

We have, further, studied transient motions away from the amplitude response curve. The role of both damping and scan rate in bringing about coherence in ion motion in the two scan directions has been presented. It is seen that increasing damping leads to coherent ion motion for both scan directions, and decreasing damping leads to loss of coherence. Similarly, very low scan rates result in coherent ion motion in both scan directions and increasing the scan rate destroys the coherence in both directions. However, this effect is larger for reverse scan compared to forward scan. This is because the rate of settling of ions to the periodic motion (coherence) is faster in the forward direction compared to the reverse scan direction.

Finally, we briefly comment on the mechanism proposed in the experimental study reported in Williams et al. (1994). In this paper, they have used the fact that octopole superposition causes the secular frequency of ions to be related to ion oscillation amplitude. Thus in forward scan experiments, the ion secular frequency "runs into" the dipolar excitation frequency causing ejection compacted in time which results in spectra with good resolution. In reverse scan, as ion oscillation amplitude increases, the secular frequency moves away from the dipolar excitation frequency resulting in spectra having poor resolution. The mechanism we have proposed in the present study does not explicitly invoke this amplitude frequency relationship but instead focuses on the constraints on pre-ejection dynamical states to explain the differential resolution. Nevertheless, a shadow of the discussion in Williams et al. (1994) may be seen in our discussion in that in one direction a jump is encountered while in the other direction it is not.

Chapter 4
Preliminary study of some coupled resonances

4.1 Introduction

This chapter presents results of a preliminary study of coupled resonances in Paul traps. The motivation of this chapter is to identify points on the Mathieu stability plot where coupled resonances occur and to select one for detailed numerical study in Chapter 5. Through the studies in this, and the next, chapters we hope to present some results which will give an insight into the complicated, but rich, dynamics associated with coupled resonances experienced by ions in Paul trap mass spectrometers.

Several investigations have confirmed the existence of nonlinear resonances, by identifying points or lines within the Mathieu stability plots where the trapping strength is lower than the neighboring regions. Some notable experimental investigations include those of Guidugli and Traldi (1991), Morand et al. (1993), Guidugli et al. (1992), Alheit et al. (1995), Alheit et al. (1996) and Chu et al. (1998). Loss of ions from the trap along these lines and points has been attributed to nonlinear resonances which arise due to superposition of higher order fields on the predominantly linear field within the trap cavity.

In an early study, Franzen et al. (1995) proposed a relationship between the radial secular frequency, axial secular frequency and the frequency of the rf drive ω_r, ω_z and Ω, respectively, that would represent potential nonlinear resonances. The relationship proposed in their study has the form

$$n_r\omega_r + n_z\omega_z = \nu\Omega \tag{4.1}$$

where n_r, n_z and ν are integers; pure axial resonance occurs when n_z is zero, pure radial resonance occurs when n_r is zero, and coupled resonance occurs when both n_r and n_z are non zero (ν may or may not be zero). The study also suggested that specific multipole superpositions contribute to specific nonlinear resonance. This last observation was confirmed in subsequent analysis of resonance points along the $a_z = 0$ axis by Abraham et al. (2004) who have identified hexapole superposition as a an important contributor to the $\beta_z = 2/3$ resonance and octopole superposition to the $\beta_z = 1/2$ resonance. In another investigation, Prasanna (2005) pointed to the role of decapole superposition in

the $\beta_z = 2/5$ resonance.

In this chapter we will use Eq. (4.1) to begin our search for candidate resonance points (within the Mathieu stability plot) for our study of coupled resonances. The multipole superpositions considered include hexapole, octopole, decapole and dodecapole. For each multipole superposition we first arbitrarily choose some resonances predicted by Eq. (4.1). Potential candidates for our study could be any point along a coupled resonance line or a point where two pure resonances, one in the radial direction and the other in the axial direction, intersect. From amongst the several intersections of different resonance lines we start with, we take up for investigation only those points where at least one coupled nonlinear resonance is also involved. i.e., there is a common intersection of three curves (see Fig. 4.1 below). We then carry out a numerical study at the chosen resonance points, to select a specific resonance for further detailed investigation in Chapter 5.

4.2 Equations of motion

In experimental traps, multipole superpositions are introduced by including higher order terms in the equation of motion. Because of axial symmetry, Legendre polynomials (Beaty,1986) have been used in the mass spectrometry literature (Franzen et al., 1995) to represent the contribution of higher order terms in the potential function. The equations of motion of ions in the axial (z) and radial (r) directions in the practical Paul trap, with hexapole, octopole, decapole and dodecapole superpositions incorporated, takes the form of a coupled, nonlinear Mathieu equation given by (Sevugarajan and Menon, 2002; Abraham et al., 2003)

$$\frac{d^2\bar{z}}{d\tau^2} + (a_z + 2q_z\cos 2\tau)\Bigg(\bar{z} + \frac{3h}{2}\bar{z}^2 - \frac{3h}{4}\bar{r}^2 + 2f\bar{z}^3 - 3f\bar{z}\bar{r}^2 + \frac{5d}{2}\bar{z}^4 - \frac{15d}{2}\bar{z}^2\bar{r}^2 + \frac{15d}{16}\bar{r}^4 + 3k\bar{z}^5 - 15k\bar{z}^3\bar{r}^2 + \frac{45k}{8}\bar{z}\bar{r}^4\Bigg) = 0 \tag{4.2}$$

$$\frac{d^2\bar{r}}{d\tau^2} + (a_r + 2q_r\cos 2\tau)\Bigg(\bar{r} + 3h\bar{z}\bar{r} + 6f\bar{z}^2\bar{r} - \frac{3}{2}\bar{r}^3 + 10d\bar{z}^3\bar{r} - \frac{15d}{2}\bar{z}\bar{r}^3 + 15k\bar{z}^4\bar{r} - \frac{45k}{2}\bar{z}^2\bar{r}^3 + \frac{15k}{8}\bar{r}^5\Bigg) = 0 \tag{4.3}$$

where h, f, d and k are the relative weights (with respect to the weight of the quadrupole superposition, A_2) of hexapole, octopole, decapole and dodecapole nonlinearity, respectively; $\bar{z}(= z/r_0)$ and $\bar{r}(= r/r_0)$ are scaled displacements in z and r directions and a_z, q_z, a_r and q_r are Mathieu parameters for the nonlinear Paul trap which are given by

$$a_z = -2a_r = \frac{8eA_2U}{mr_0^2\Omega^2} \tag{4.4}$$

$$q_z = -2q_r = -\frac{4eA_2V}{mr_0^2\Omega^2} \tag{4.5}$$

Equations (4.2) and(4.3) are coupled nonlinear Mathieu equations, with the former equation representing the motion in the axial direction and the latter equation the radial direction motion. These nonlinear equations will be used in our numerical studies presented below.

4.3 Nonlinear resonances

The resonance conditions, derived from the conditions outlined in Franzen et. al. (1995) and considered in the present study are summarized in Table 4.1. Briefly, Franzen's recommendations on n_r and n_z in Eq. (4.1), pertaining to which multipoles they correspond with, are:

n_r is even for all multipoles,
n_z is even for even multipoles and
any integer for odd multipoles.
and $|n_r| + |n_z| \leq \aleph + 1$

where $\aleph$ refers to the order (number of pairs of poles) of the multipoles. Some choices satisfying these criteria are listed in Table 1. As seen from the table, each nonlinearity is

Table 4.1: Nonlinearities and resonance curves.

Nonlinearity	**Nonlinear resonances**
hexapole	$\beta_z = \frac{1}{2}$, $\beta_r = \frac{1}{2}$, $\beta_z = \frac{2}{3}$, $\beta_r + \beta_z = 1$
otopole	$\beta_z = \frac{1}{2}$, $\beta_r = \frac{1}{2}$, $\beta_r + \beta_z = 1$
decapole	$\beta_r = \frac{1}{3}$, $\beta_r = \frac{1}{2}$, $\beta_z = \frac{1}{2}$ $\beta_z = \frac{1}{3}$, $\beta_z = \frac{2}{5}$ $\beta_r + \beta_z = 1$, $2\beta_r + \beta_z = 1$, $4\beta_r + \beta_z = 2$
dodecapole	$\beta_r = \frac{1}{3}$, $\beta_r = \frac{1}{2}$, $\beta_z = \frac{1}{2}$, $\beta_z = \frac{1}{3}$, $\beta_z = \frac{2}{5}$ $\beta_r + \beta_z = 1$, $2\beta_r + \beta_z = 1$, $4\beta_r + \beta_z = 2$

associated with specific nonlinear resonances in the trap. These resonances include both one-direction resonance (which involves *either* β_r *or* β_z) as well as coupled resonances (which involves *both* β_r *and* β_z). A point to be noted is that resonances $\beta_z = \frac{1}{2}$, $\beta_r = \frac{1}{2}$, $\beta_r + \beta_z = 1$ are common to all superpositions.

Figure 4.1 is the Mathieu stability plot with the nonlinear resonance curves (presented in Table 1) corresponding to the different superpositions. At several points on the plot we observe intersection of two or more nonlinear resonance curves. These intersections involve intersections of one-direction resonance curves as well as intersections with curves of coupled resonances.

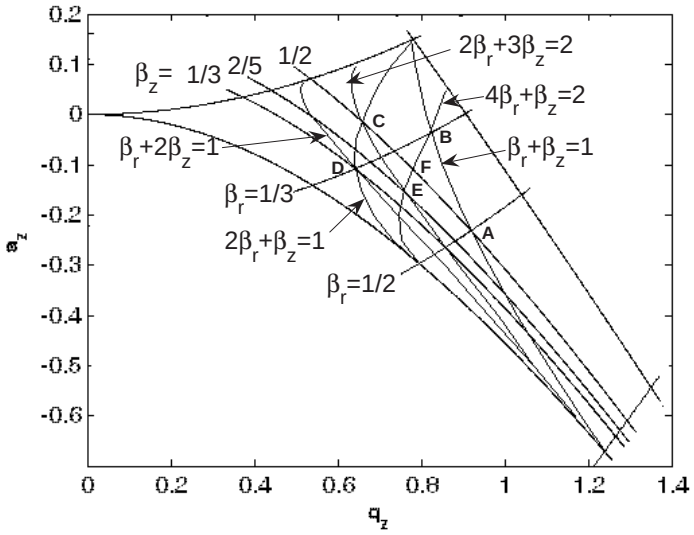

Figure 4.1: Nonlinear resonance lines in Mathieu stability plot

In order to numerically study the ion behavior at these points we need to first determine the values of a_z and q_z at the points of intersection of the resonance curves. In our present study, we restrict our attention to only those points in which at least one coupled resonance (resonance involving both β_z and β_r) is involved. In Fig. 1, these points have been labelled as A, B, C, D, E and F.

To determine the a_z and q_z values for points A to F we first substitute the general solution (Eq. (1.9)) into the linear Mathieu equation (Eq. (1.7)) after expressing a_r and q_r in terms of a_z and q_z (Eq. 1.8)). For a given point we apply the harmonic balance method (below) to obtain two equations in four unknowns viz., β_z, β_r, a_z and q_z. These two equations, when combined with the additional equations of nonlinear resonance at the point under study, enables us to obtain the values of a_z, q_z, β_r and β_z at the chosen point. The values of a_z and q_z at the point of intersection will be referred to as a_z^* and q_z^* in our discussions.

The linear Mathieu equation in the r and z directions can be written as

$$\frac{d^2r}{d\tau^2} - (\frac{a_z}{2} + q_z \cos 2\tau)r = 0 \tag{4.6}$$

$$\frac{d^2z}{d\tau^2} + (a_z + 2q_z \cos 2\tau)z = 0 \tag{4.7}$$

As the cosine series and sine series of the general solution (Equation 1.4) are independent solutions of the linear Mathieu equation, for finding a_z and q_z we substitute the cosine solution

$$u = \sum_{n=-\infty}^{\infty} C_{n,u} \cos(\beta_u + 2n)\tau \tag{4.8}$$

into the linear Mathieu equations. In the presentation below we use a truncated series for $-3 \leq n \leq 3$, although in our actual calculations, we used $-5 \leq n \leq 5$. We therefore have

$$\begin{aligned} r(\tau) = {} & c_{-3,r} \cos(\beta_r \tau - 6\tau) + c_{-2,r} \cos(\beta_r \tau - 4\tau) + c_{-1,r} \cos(\beta_r \tau - 2\tau) \\ & + c_{0,r} \cos(\beta_r \tau) + c_{1,r} \cos(\beta_r \tau + 2\tau) + c_{2,r} \cos(\beta_r \tau + 4\tau) \\ & + c_{3,r} \cos(\beta_r \tau + 6\tau) \end{aligned} \tag{4.9}$$

$$\begin{aligned} z(\tau) = {} & c_{-3,z} \cos(\beta_z \tau - 6\tau) + c_{-2,z} \cos(\beta_z \tau - 4\tau) + c_{-1,z} \cos(\beta_z \tau - 2\tau) \\ & + c_{0,z} \cos(\beta_z \tau) + c_{1,z} \cos(\beta_z \tau + 2\tau) + c_{2,z} \cos(\beta_z \tau + 4\tau) \\ & + c_{3,z} \cos(\beta_z \tau + 6\tau)\,. \end{aligned} \tag{4.10}$$

Substituting Equations (4.9) and (4.10) into Equations (4.6) and (4.7), respectively and equating separately to zero the coefficients of the cosine terms used in the expansion, we have

$$\begin{bmatrix} (-36-\frac{1}{2}a_z & -\frac{1}{2}q_z & 0 & 0 & 0 & 0 & 0 \\ +12\beta_r-\beta_r^2) & & & & & & \\ -\frac{1}{2}q_z & (-16-\beta_r^2+ & -\frac{1}{2}q_z & 0 & 0 & 0 & 0 \\ & 8\beta_r-\frac{1}{2}a_z) & & & & & \\ 0 & -\frac{1}{2}q_z & (-4-\beta_r^2+ & -\frac{1}{2}q_z & 0 & 0 & 0 \\ & & 4\beta_r-\frac{1}{2}a_z) & & & & \\ 0 & 0 & -\frac{1}{2}q_z & -\beta_r^2-\frac{1}{2}a_z & -\frac{1}{2}q_z & 0 & 0 \\ 0 & 0 & 0 & -\frac{1}{2}q_z & (-4-\beta_r^2- & -\frac{1}{2}q_z & 0 \\ & & & & 4\beta_r-\frac{1}{2}a_z) & & \\ 0 & 0 & 0 & 0 & -\frac{1}{2}q_z & (-16-\beta_r^2- & -\frac{1}{2}q_z \\ & & & & & 8\beta_r-\frac{1}{2}a_z) & \\ 0 & 0 & 0 & 0 & 0 & -\frac{1}{2}q_z & (-36-\beta_r^2 \\ & & & & & & -12\beta_r) \end{bmatrix} \begin{bmatrix} c_{-3,r} \\ c_{-2,r} \\ c_{-1,r} \\ c_{0,r} \\ c_{1,r} \\ c_{2,r} \\ c_{3,r} \end{bmatrix} = 0$$

and

$$\begin{bmatrix} (-36+a_z & q_z & 0 & 0 & 0 & 0 & 0 \\ +12\beta_z-\beta_z^2) & & & & & & \\ q_z & (-16-\beta_z^2+ & q_z & 0 & 0 & 0 & 0 \\ & 8\beta_z+a_z) & & & & & \\ 0 & q_z & (-4-\beta_z^2+ & q_z & 0 & 0 & 0 \\ & & 4\beta_z+a_z) & & & & \\ 0 & 0 & q_z & -\beta_z^2+a_z & q_z & 0 & 0 \\ 0 & 0 & 0 & q_z & (-4-\beta_z^2- & q_z & 0 \\ & & & & 4\beta_z+a_z) & & \\ 0 & 0 & 0 & 0 & q_z^* & (-16-\beta_z^2- & q_z \\ & & & & & 8\beta_z+a_z) & \\ 0 & 0 & 0 & 0 & 0 & q_z & (-36-\beta_z^2 \\ & & & & & & -12\beta_z) \end{bmatrix} \begin{bmatrix} c_{-3,z} \\ c_{-2,z} \\ c_{-1,z} \\ c_{0,z} \\ c_{1,z} \\ c_{2,z} \\ c_{3,z} \end{bmatrix} = 0$$

For the set of equations given by the above two matrices to have nontrivial solutions, the determinants of the 7×7 coefficient matrices must be zero. These conditions provide us two equations in the four unknowns β_z, β_r, a_z and q_z. We solve these equations together with $\beta_r + \beta_z = 1$ and $\beta_z = \frac{1}{2}$ or $\beta_r = \frac{1}{2}$ to determine the parameters at A. The values of β_z, β_r, a_z and q_z at points B, C, D, E and F can be determined by the same method. The special a_z, q_z values corresponding to these resonances are denoted with stars below.

The a_z^*, q_z^* for points A to F are presented in Table 4.2. The a_z and q_z values at

Table 4.2: a_z^* and q_z^* at the intersection of nonlinear resonance curves.

Point	**Intersecting curves**	a_z^*	q_z^*
A	$\beta_z = \frac{1}{2}$, $\beta_r = \frac{1}{2}$, $\beta_r + \beta_z = 1$	-0.2313850427	0.9193009931
B	$\beta_r = \frac{1}{3}$, $\beta_r + \beta_z = 1$, $4\beta_r + \beta_z = 2$	-0.0365773350	0.8226392657
C	$\beta_z = \frac{1}{2}$, $2\beta_r + \beta_z = 1$, $2\beta_r + 3\beta_z = 2$	-0.0119395698	0.6556667239
D	$\beta_z = \frac{1}{3}$,$2\beta_r + \beta_z = 1$, $\beta_r = \frac{1}{3}$, $\beta_r + 2\beta_z = 1$	-0.1079706121	0.6423010023
E	$\beta_z = \frac{2}{5}$, $2\beta_r + 3\beta_z = 2$, $4\beta_r + \beta_z = 2$	-0.1530910493	0.7582156960
F	$\beta_z = \frac{1}{2}$, $4\beta_r + \beta_z = 2$	-0.1088800013	0.7792799900

which we expect to observe nonlinear resonant behavior in the experimental traps may be slightly detuned from a_z^* and q_z^*. Consequently, our numerical study will probe ion behavior at a_z, q_z values in the neighborhood of a_z^*, q_z^*.

4.4 Numerical study

We use Poincaré sections (Strogatz, 1994; Rand, 2005) to study the stability of ions at the chosen points on the Mathieu stability diagram. The Poincaré sections are generated by strobing the solutions at intervals equal to the period of the parametric forcing. Figures 4.2 to 4.7 show the Poincaré sections for r and z directions at points A to F, with an initial condition $(z, \dot{z}, r, \dot{r}) = (0.05, 0, 0.05, 0)$. In all these figures, $\diamond$ corresponds to the radial

motion and $\star$ corresponds to axial motion. Although these plots present the behavior of ions for a specific combination of multipole superpositions, they have been selected from a large set of combinations of field superpositions which were analyzed. Table 4.3 presents one example, at point A, of how we proceeded to analyze the stability of ion motion.

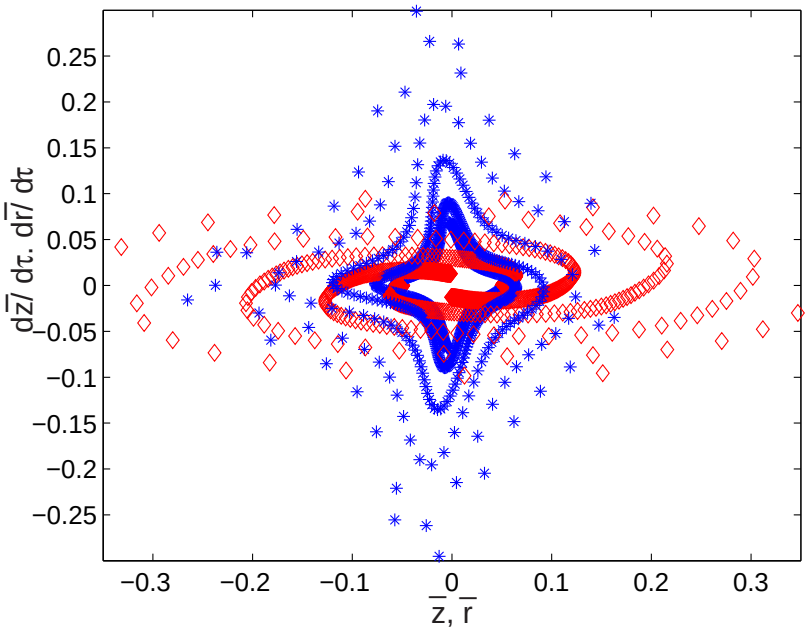

Figure 4.2: Poincaré sections in the z and r direction at $a_z = -0.23131$ and $q_z = 0.91919$ for 10% hexapole and 10% octopole superposition corresponding to point A in Fig. 4.1.

Consider the intersection of the lines $\beta_r = \frac{1}{2}$, $\beta_z = \frac{1}{2}$, $\beta_r + \beta_z = 1$, resonances corresponding to point A in Fig. 4.1. These resonances are common to all nonlinearities. Our detailed study of various combination of nonlinearities revealed that some combinations (Table 4.3) displayed simultaneous unstable behavior in r and z directions, other combinations resulted in only z direction instability and several combinations resulted in stable behavior. Figure 4.2 is a Poincaré section for 10% hexapole and 10% octopole superpositions, where ion motion is unstable in the r and z directions simultaneously. The $a_z$and q_z values chosen for this plots are -0.23131 and 0.91919, respectively, values which are detuned from a_z^* and q_z^*.

Figure 4.3 is the Poincaré section at the intersection of $\beta_r = \frac{1}{3}$, $\beta_r + \beta_z = 1$ and $4\beta_r + \beta_z = 2$ corresponding to point B in Fig. 4.1. Here the curve $\beta_r + \beta_z = 1$ is common for all nonlinearities and curves $\beta_r = \frac{1}{3}$ and $4\beta_r + \beta_z = 2$ are specific to only decapole nonlinearity (as per Franzen's recommendations). Some combinations of nonlinearities displayed stable behavior while other combinations displayed instability only in the z direction; *no* combination of nonlinearity, including those with negative signs assigned to

Table 4.3: Stability of ion motion for different combinations of higher order superpositions in the neighborhood of point A ($a_z = -0.23131$ and $q_z = 0.91919$). All nonzero superpositions were arbitrarily taken to be $\pm 10\%$, to exaggerate their influence.

Percentage of				
hexapole	octopole	decapole	dodecapole	stability
10	10	0	0	r, z unstable
10	10	10	0	r, z unstable
10	10	0	10	r, z unstable
10	10	10	10	r, z unstable
-10	10	0	0	r, z unstable
-10	0	-10	0	r, z unstable
10	10	-10	0	r, z unstable
-10	10	10	0	r, z unstable
-10	10	0	10	r, z unstable
-10	10	10	10	r, z unstable
10	10	-10	10	r, z unstable
10	10	10	-10	r, z unstable
10	0	0	10	z unstable
10	0	10	10	z unstable
10	0	-10	0	z unstable
-10	0	10	0	z unstable
64 other combinations involving 0 and $\pm 10\%$				r, z stable

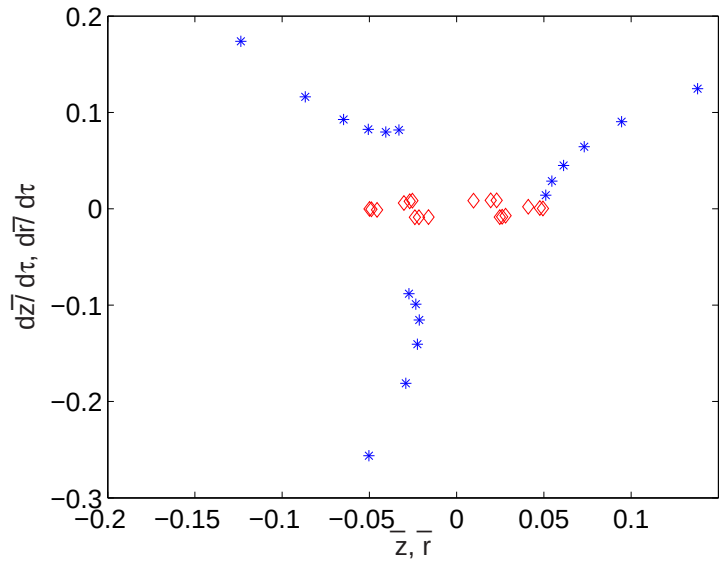

Figure 4.3: Poincaré sections in the z and r direction at $a_z = -0.0365$ and $q_z = 0.8226$ for 10% hexapole, 10% octopole, 10% decapole and 10% dodecapole superposition corresponding to point B in Fig. 4.1.

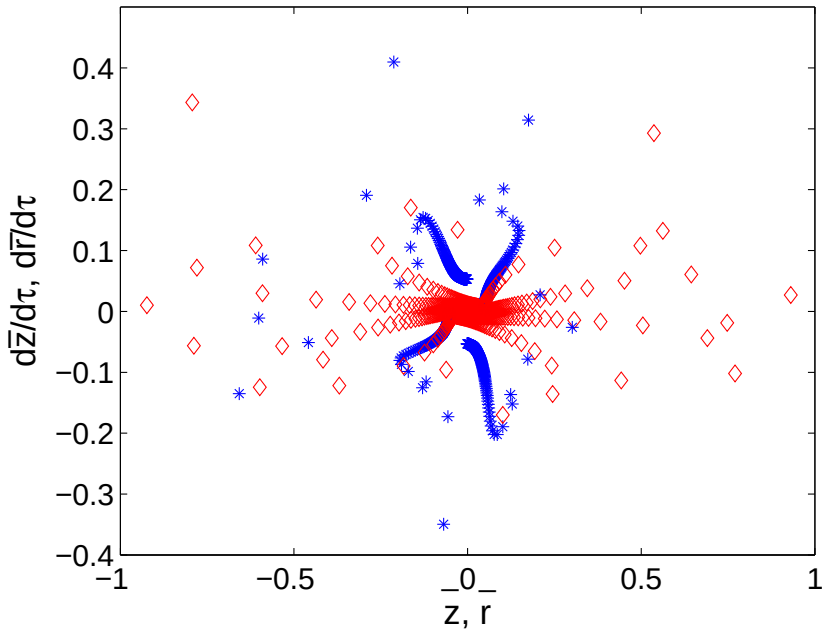

Figure 4.4: Poincaré sections in the z and r direction at $a_z = -0.0119$ and $q_z = 0.6556$ for 10% hexapole, 10% decapole and 10% dodecapole superposition corresponding to point C in Fig. 4.1.

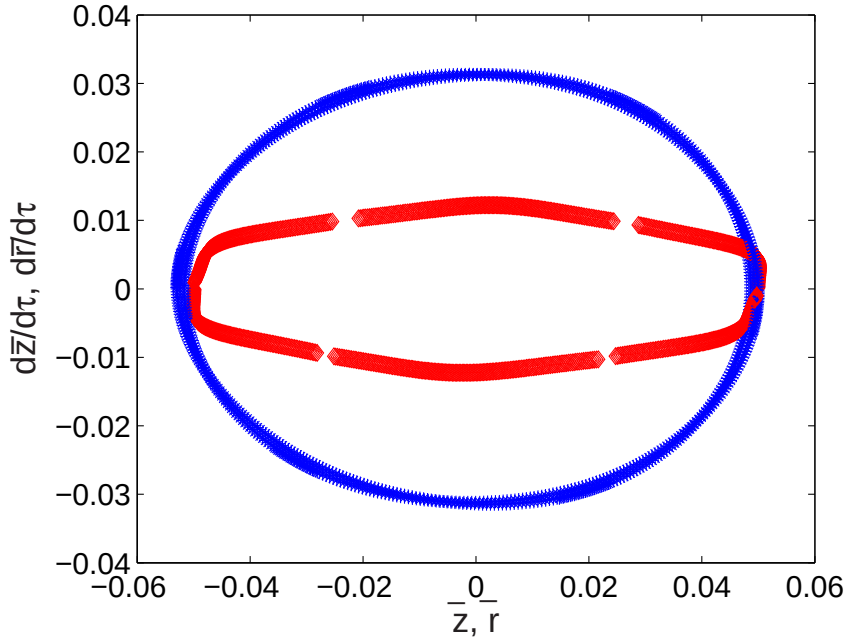

Figure 4.5: Poincaré sections in the z and r direction at ($a_z = -0.1079$, $q_z = 0.6423$) for 10% decapole and 10% dodecapole superposition corresponding to point D in Fig. 4.1.

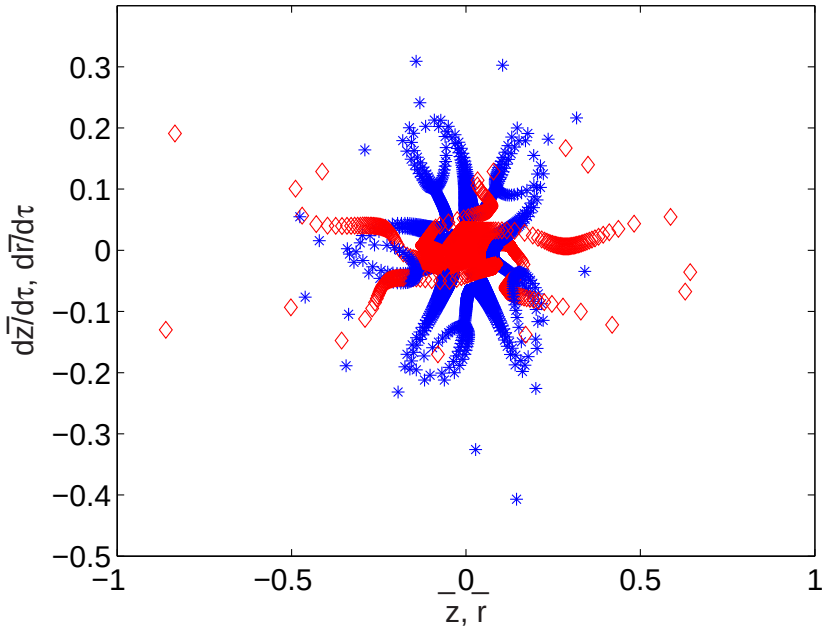

Figure 4.6: Poincaré sections in the z and r direction at $a_z = -0.1531$ and $q_z = 0.7582$ for 10% decapole superposition corresponding to point E in Fig. 4.1.

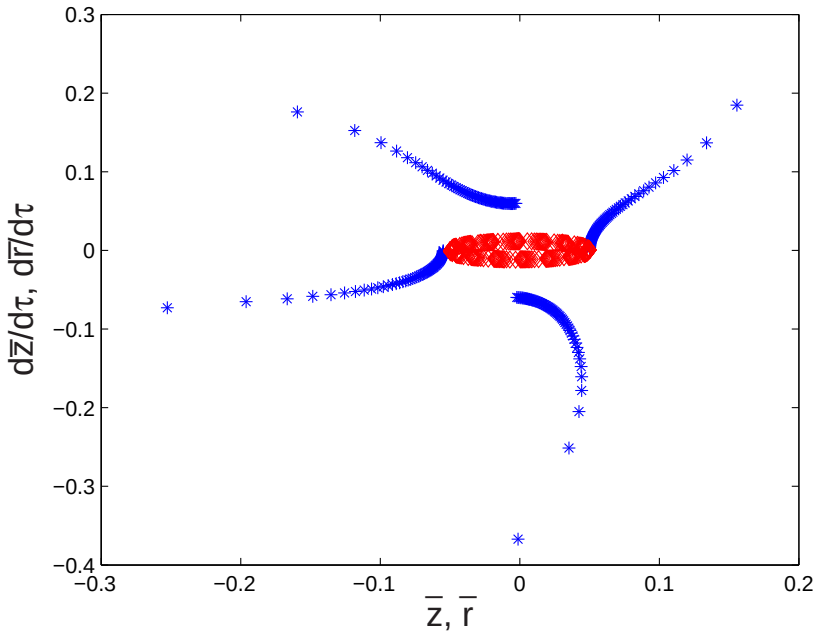

Figure 4.7: Poincaré sections in the z and r direction at $a_z = -0.1088$ and $q_z = 0.7792$ for 10% hexapole, 10% decapole and 10% dodecapole superposition corresponding to point F in Fig. 4.1.

the nonlinearity, displayed instability in both directions simultaneously. It may be noted that $\beta_r = \frac{1}{3}$, which implies $\beta_z = \frac{2}{3}$, causes the 3π periodicity in the z direction motion observed in the figure. Detuned a_z and q_z values used for this plot are -0.0365 and 0.8226, respectively.

Figure 4.4 is the Poincaré section at the intersection of $\beta_z = \frac{1}{2}$, $2\beta_r + \beta_z = 1$ and $2\beta_r + 3\beta_z = 2$ corresponding to point C in Fig. 4.1. Resonance occurs along $\beta_z = \frac{1}{2}$ for all nonlinearities. $2\beta_r + \beta_z = 1$ is a resonance curve corresponding to decapole and dodecapole superpositions while $2\beta_r + 3\beta_z = 2$ is specific to decapole superposition only (as per Franzen's recommendations). Here two situations arise for different combinations of nonlinearities, one which displays stable behavior in r and z directions and the other which displays unstable behavior in both z and r directions. Figure 4.4 shows the Poincaré plot for 10% hexapole, 10% decapole and 10% dodecapole nonlinearities at the detuned a_z and q_z values of -0.0119 and 0.6557, respectively, for a situation in which the ion becomes simultaneously unstable in both the z and r directions. We further observed that in the *absence* of hexapole the ions are stable, and the presence of octopole stabilizes the ion motion.

Figure 4.5 is the Poincaré section at the intersection of $\beta_r = \frac{1}{3}$, $\beta_z = \frac{1}{3}$, $2\beta_r + \beta_z = 1$ and $\beta_r + 2\beta_z = 1$ corresponding to point D in Fig. 4.1. All these resonance curves are due

to the superposition of decapole and dodecapole nonlinearities only, and we observed that all combinations of decapole and dodecapole superpositions resulted in stable behavior. The Poincaré section for 10% decapole and 10% dodecapole superpositions shown in Fig. 4.5 displays stable trajectories in both directions for $a_z = -0.1079$ and $q_z = 0.6423$.

Figure 4.6 is the Poincaré section at the intersection of $\beta_z = \frac{2}{5}$, $2\beta_r + 3\beta_z = 2$ and $4\beta_r + \beta_z = 2$ corresponding to point E in Fig. 4.1. The resonance curves here are due to decapole superposition alone. Figure 4.6 is a Poincaré plot for 10% decapole superposition which displays instability in both z and r directions at $a_z = -0.1531$ and $q_z = 0.6536$.

Figure 4.7 is the Poincaré section at the intersection of $\beta_z = \frac{1}{2}$ and $4\beta_r + \beta z = 2$ corresponding to point F in Fig. 4.1. $\beta_z = \frac{1}{2}$ is a resonance line for all nonlinearities and $4\beta_r + \beta z = 2$ corresponds to decapole superposition alone. Here a combination of 10% hexapole, 10% decapole and 10% dodecapole resulted in unstable z direction motion while all other combinations displayed stable behavior in both directions for detuned a_z and q_z values of -0.1088 and 0.7792, respectively. In this figure it may be seen that z direction motion has a 4π periodicity since $\beta_z = \frac{1}{2}$.

4.5 Concluding remarks

The Poincaré sections presented above at select points on the Mathieu stability plot (Fig. 4.1 and Table 4.2) reveal a variety of behaviors. Amongst these six points studied it was seen that D displayed stable behavior, B and F displayed instability only in the z direction, and points A, C and E showed simultaneous instability in z and r directions.

We note that all the figures generated were for specific arbitrary choices of detuning, and so the study necessarily presents a limited picture. However, as will be seen, this is sufficient for our purpose.

For proceeding with our detailed study in Chapter 5 we select the resonance at $\beta_r = \frac{1}{2}$, $\beta_z = \frac{1}{2}$, $\beta_r + \beta_z = 1$ (corresponding to A in Fig. 4.1). We choose this point from among A, C and E primarily on the experimental observation of Alheit et al., (1995) where it was noted that this resonance is very prominent. Our study will consequently focus on the dynamics of coupled resonance in the neighborhood of $a_z^* = -0.2313850427$ and $q_z^* = 0.9193009931$.

In order to confirm that the instability seen in Fig. 4.2 is indeed due to coupling, we generated Poincaré sections of the uncoupled solutions. The uncoupled solution in the axial direction is obtained by setting the initial conditions as $(\bar{z}, \dot{\bar{z}}, \bar{r}, \dot{\bar{r}}) = (0.05, 0, 0, 0)$ and for the uncoupled solution in the radial direction the initial conditions were chosen as $(\bar{z}, \dot{\bar{z}}, \bar{r}, \dot{\bar{r}}) = (0, 0, 0.05, 0)$. Figure 5.1 shows the Poincaré sections in the r and z directions

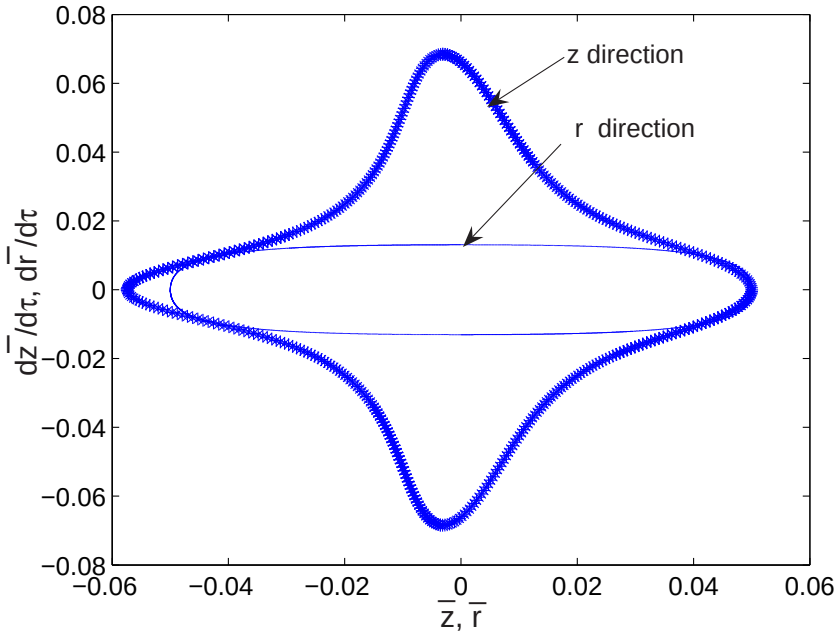

Figure 4.8: Poincaré sections of the uncoupled solutions in r direction and z direction at $a_z = -0.23131$ and $q_z = 0.91919$ for 10% hexapole and 10% octopole superposition.

for the uncoupled system at $a_z = -.23131$ and $q_z = .91919$ for 10 percent heaxapole and octopole superposition. The uncoupled solutions are seen to be stable confirming that the dynamics observed in Fig. 4.2 was on account of coupled resonance.

In the numerical study above it was seen that at point A in Fig. 4.1 ion destabilization occurs simultaneously in the z and r directions. Although the resonance curves at this point are relevant to all nonlinearities, we saw that inclusion of hexapole and octopole nonlinearities alone were adequate to display this coupled resonance. Further, we also determined that even weaker nonlinearity was sufficient to cause simultaneous ion destabilization. Consequently in the analytical study presented in the next chapter our equation of motion will include only hexapole and octopole nonlinearities, and the strength of these nonlinearities will be fixed at 2%.

Chapter 5

Approximate averaging of coupled radial/axial ion motions in Paul trap near a double resonance point

5.1 Introduction

In this chapter we make a detailed study of the resonant point proposed in Chapter 4. We consider the coupled nonlinear Mathieu equations, with hexapole and octopole superpositions only, which has the form

$$\frac{d^2\bar{z}}{d\tau^2} + (a_z + 2q_z \cos 2\tau)\left[\bar{z} + \frac{3h}{2}\bar{z}^2 - \frac{3h}{4}\bar{r}^2 + 2f\bar{z}^3 - 3f\bar{z}\bar{r}^2\right] = 0 \tag{5.1}$$

$$\frac{d^2\bar{r}}{d\tau^2} + (a_r + 2q_r \cos 2\tau)\left[\bar{r} + 3h\bar{z}\bar{r} + 6f\bar{z}^2\bar{r} - \frac{3f}{2}\bar{r}^3\right] = 0 \tag{5.2}$$

where h and f are small. a_z $(= -2a_r)$ and q_z $(= -2q_r)$ are called Mathieu parameters, and $\bar{r}$ and $\bar{z}$ refer to the nondimesionalized radial and axial displacements of ions. We develop new analytical approximations for the ion dynamics in the neighborhood of an interesting coupled nonlinear resonance, and investigate several aspects of the resonant dynamics that precedes eventual escape of the ion from the trap.

The unperturbed Mathieu equation has a general solution, referred to as the Mathieu function (McLachlan, 1947, 1958; Abromowitz and Stegun, 1970), of the form

$$u = A_u \sum_{n=-\infty}^{\infty} C_{2n,u} \cos(\beta_u + 2n)\tau + B_u \sum_{n=-\infty}^{\infty} C_{2n,u} \sin(\beta_u + 2n)\tau \tag{5.3}$$

where u could refer to either r or z, A_u and B_u are arbitrary constants and $C_{2n,u}$ are interrelated constants which give the relative amplitudes of the various harmonics in the solution. Finally, β_u is a parameter dependent on the Mathieu parameters a_u and q_u (more on this below).

It is known that in Paul traps nonlinear resonances lead to instability of ions within the trap (Franzen et al., 1995). These resonances may lead to individual z- or r- direction instabilities or to inherently coupled z- and r- instability as was seen in Chapter 4. An earlier analytical study has looked at uncoupled resonances when $a_z = 0$ and $q_z = 0.64$ and 0.78 in Eq. (5.1) (Abraham and Chatterjee, 2003). In the present study we take up

one prominent coupled resonance, which has also been observed experimentally (Alheit et al., 1995), at the intersection on the (a_z, q_z) plane of the curves along which $\beta_z = \frac{1}{2}$, $\beta_r = \frac{1}{2}$ and, consequently $\beta_r + \beta_z = 1$.

Equations (5.1) and (5.2) are not solvable in closed form. We note however that the secular frequency (a quantity proportional to β_u) of the linearized system in the z- and r- directions are subharmonics of the forcing frequency.

In this chapter, we will develop approximate analytical expressions using the method of harmonic balance based averaging (Chatterjee, 2002; Abraham and Chatterjee, 2003) for the slow flow equations governing motion of ion in the two directions. These will be used to understand some features of the dynamics of coupled resonance at the intersection of $\beta_z = \frac{1}{2}$, $\beta_r = \frac{1}{2}$ and $\beta_r + \beta_z = 1$.

We will present a numerical, and admittedly limited, study of the slow flow with the objective of exploring and displaying some of the possible types of interesting ion motions. In particular, we will choose specific but arbitrary parameter values; study the stability of the individual radial and axial motion invariant manifolds; examine the rather large times associated with escape of ions; notice regions in the averaged phase space wherein trajectories do not, in fact, escape; observe apparently chaotic dynamics preceding escape for ions that do escape; and note that trajectories that do not escape appear to be confined to 4-tori. We will finally conclude with some comments on the implications for practical operation of the Paul trap near this resonant point.

5.2 Harmonic balance and initial numerics

The values of a_z and q_z at the resonant point of interest, were determined by the harmonic balance method in Chapter 4. The main result is that, for the linearized system ($f = 0$, $h = 0$ in Eqs. (5.1) and (5.2)), if $a_z = -0.2313850427$, $q_z = 0.9193009931$, $a_r = -a_z/2$, and $q_r = -q_z/2$, then $\beta_r = 1/2$, $\beta_z = 1/2$, and $\beta_r + \beta_z = 1$. These values of a_z and q_z will be referred to as a_z^* and q_z^*. In this chapter, we will consider the effects of small nonlinearities (small f and h), as well as a_z and q_z values that are detuned slightly from these ideal resonant values.

To numerically study the stability of the system (Eqsz. (5.1) and (5.2)) we generate Poincaré maps by strobing the solutions at periodic intervals corresponding to the period of the parametric forcing ($\cos 2\tau$). Figures 5.1(a) and 5.1(b) are the Poincaré maps for uncoupled solutions for two sets of initial conditions, one with $\bar{r} \equiv 0$ and one with $\bar{z} \equiv 0$. These figures show that r and z motions are individually stable. Figure 5.2 shows the coupled instability in the z- and r- directions, for a solution in which both $\bar{r}$ and $\bar{z}$ are nonzero. The point here is that r or z motions, at these parameter values, are not

individually unbounded; however, if both $\bar{r}$ and $\bar{z}$ are nonzero, then there is an instability that leads to unbounded solutions.

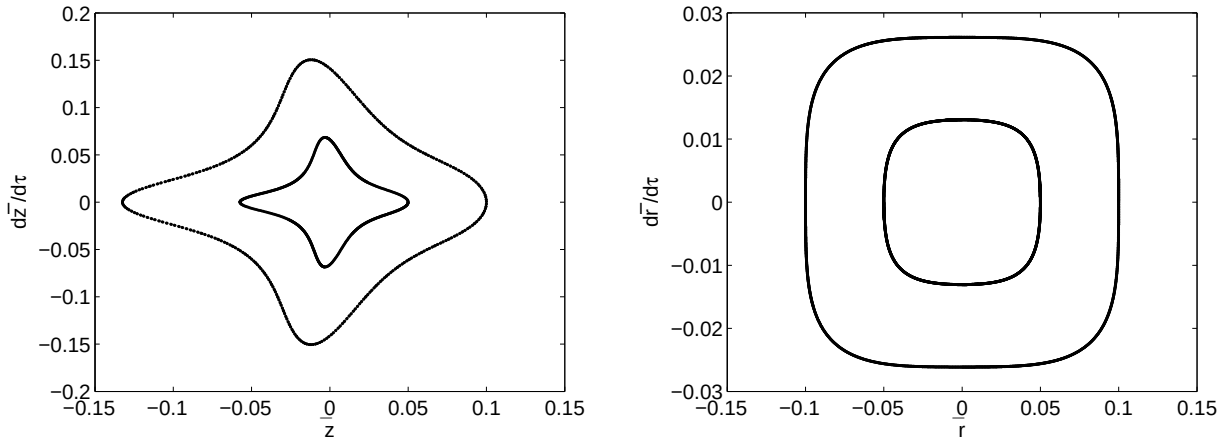

(a) (b)

Figure 5.1: Poincaré sections of the uncoupled solutions for two different sets of initial conditions at $a_z = -0.23131$, $q_z = 0.91919$ and for $h = f = 0.1$. (a) z-direction, obtained by setting $\bar{r} \equiv 0$, and (b) r-direction, obtained by setting $\bar{z} \equiv 0$.

5.3 Analytical treatment

To investigate the behavior of the ions near the point of our interest we develop approximate analytical expressions using harmonic balance based averaging (Chatterjee, 2002; Abraham and Chatterjee, 2003; Nandakumar and Chatterjee, 2004). In particular, in formally conducting higher order averaging even though we use harmonic balance approximations for the solution of the unperturbed system, we are really doing pseudoaveraging that is not asymptotically valid, but nevertheless useful, as discussed in Nandakumar and Chatterjee (2005 (b)).

5.3.1 Change of variables

We begin by rewriting Eqs. (5.1) and (5.2) in the form

$$\frac{d^2\bar{z}}{d\tau^2} + (a_z^* + 2q_z^* \cos 2\tau)\bar{z} + \epsilon F_1(\bar{z}, \bar{r}, \tau) = 0 \tag{5.4}$$

$$\frac{d^2\bar{r}}{d\tau^2} + (a_r^* + 2q_r^* \cos 2\tau)r + \epsilon F_2(\bar{z}, \bar{r}, \tau) = 0 \tag{5.5}$$

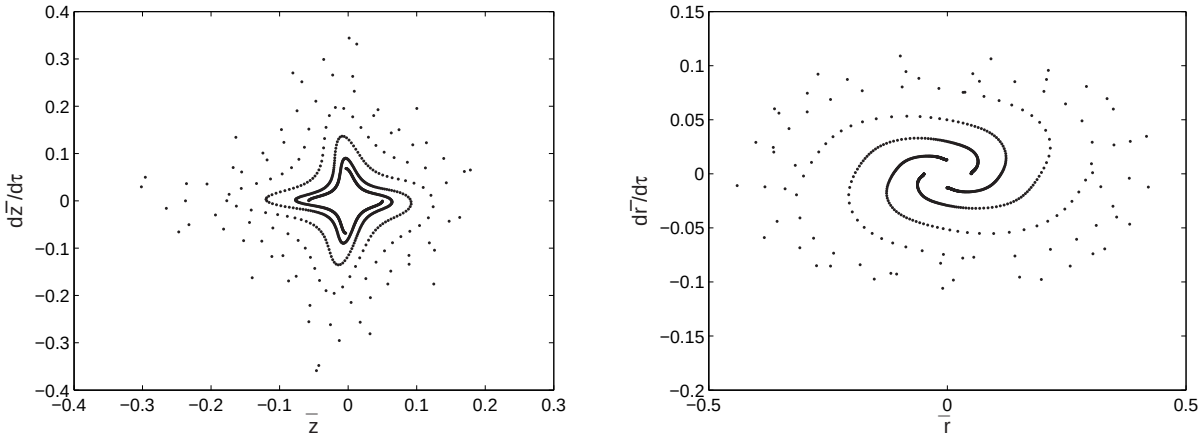

(a) (b)

Figure 5.2: Poincaré sections of the coupled solutions at $a_z = -0.23131$, $q_z = 0.91919$ and for $h = f = 0.1$. Initial conditions for $(\bar{z}, \dot{\bar{z}}, \bar{r}, \dot{\bar{r}}) = (0.05, 0, 0.05, 0)$. (a) z- direction motion (b) r-direction motion.

where F_1 and F_2 are π-periodic functions in τ and represent perturbations to the linear Mathieu equations at the resonant point. The perturbation is assumed to be small, i.e., $0 < \epsilon \ll 1$. The parameters of Eqs. (5.1) and (5.2) are expressed as

$$a_z = a_z^* + \epsilon \bar{a}_z \qquad q_z = q_z^* + \epsilon \bar{q}_z \tag{5.6}$$

and

$$h = \epsilon \bar{h} \qquad f = \epsilon \bar{f} \tag{5.7}$$

where $\bar{a}_z$ and $\bar{q}_z$ are called detuning parameters. F_1 and F_2 in Eqs. (5.4) and (5.5) are then

$$F_1 = (\bar{a}_z + 2\bar{q}_z \cos 2\tau)\bar{z} + (a_z^* + 2q_z^* \cos 2\tau)\left(\frac{3}{2}\bar{h}\bar{z}^2 - \frac{3}{4}\bar{h}\bar{r}^2 + 2\bar{f}\bar{z}^3 - 3\bar{f}\bar{z}\bar{r}^2\right) \tag{5.8}$$

$$F_2 = (\bar{a}_r + 2\bar{q}_r \cos 2\tau)\bar{r} + (a_r^* + 2q_r^* \cos 2\tau)\left(3\bar{h}\bar{r} + 6\bar{h}\bar{z}\bar{r} - \frac{3}{2}\bar{f}\bar{r}^3\right) \tag{5.9}$$

When $\epsilon = 0$, Eqs. (5.4) and (5.5) represent the unperturbed system which will have periodic solutions of the form

$$\bar{z} = A_z g_{z1}(\tau) + B_z g_{z2}(\tau) \tag{5.10}$$

$$\bar{r} = A_r g_{r1}(\tau) + B_r g_{r2}(\tau) \tag{5.11}$$

where A_z, B_z, A_r, B_r are arbitrary constants and g_{z1}, g_{z2}, g_{r1}, g_{r2} are linearly independent solutions having the form

$$g_{z1}(\tau) = \sum_{n=-\infty}^{\infty} C_{2n,z} \cos(\beta_z + 2n)\tau \tag{5.12}$$

$$g_{z2}(\tau) = \sum_{n=-\infty}^{\infty} S_{2n,z} \sin(\beta_z + 2n)\tau \tag{5.13}$$

$$g_{r1}(\tau) = \sum_{n=-\infty}^{\infty} C_{2n,r} \cos(\beta_r + 2n)\tau \tag{5.14}$$

$$g_{r2}(\tau) = \sum_{n=-\infty}^{\infty} S_{2n,r} \sin(\beta_r + 2n)\tau \tag{5.15}$$

Any finite number of the coefficients $C_{2n,z}$, $S_{2n,z}$, $C_{2n,r}$ and $S_{2n,r}$ can be evaluated by the method of harmonic balance (Abraham and Chatterjee, 2003). g_{z1}, g_{z2}, g_{r1} and g_{r2} for $-3 < n < 3$, are given in Section 5.6.1.

When $\epsilon \neq 0$ we assume, as is usual in the method of averaging, that the perturbed equations continue to have solutions of the form of Eqs. (5.10) and (5.11), but the coefficients A_z, B_z, A_r and B_r will now be slowly varying functions of τ. The solutions of Eqs. (5.4) and (5.5) can then be written as

$$\bar{z} = A_z(\tau) g_{z1}(\tau) + B_z(\tau) g_{z2}(\tau) \tag{5.16}$$

$$\bar{r} = A_r(\tau) g_{r1}(\tau) + B_r(\tau) g_{r2}(\tau) \tag{5.17}$$

To solve Eqs. (5.4) and (5.5) after substituting Eqs. (5.16) and (5.17), we impose additional constraints as usual,

$$\dot{\bar{z}} = A_z(\tau) \dot{g}_{z1}(\tau) + B_z(\tau) \dot{g}_{z2}(\tau) \tag{5.18}$$

$$\dot{\bar{r}} = A_r(\tau) \dot{g}_{r1}(\tau) + B_r(\tau) \dot{g}_{r2}(\tau) \tag{5.19}$$

Substituting Eqs. (5.18) and (5.19) into Eqs. (5.4) and (5.5), and dropping the dependence on τ for the sake of brevity, we get

$$A_z \ddot{g}_{z1} + \dot{A}_z \dot{g}_{z1} + B_z \ddot{g}_{z2} + \dot{B}_z \dot{g}_{z2} + (a_z + 2q_z \cos 2\tau)(A_z g_{z1} + B_z g_{z2}) + \epsilon F_1 = 0 \tag{5.20}$$

$$A_r \ddot{g}_{r1} + \dot{A}_r \dot{g}_{r1} + B_r \ddot{g}_{r2} + \dot{B}_r \dot{g}_{r2} + (a_r + 2q_r \cos 2\tau\ )(A_r g_{r1} + B_r g_{r2}) + \epsilon F_2 = 0 \tag{5.21}$$

As g_{z1}, g_{z2}, g_{r1}, g_{r2} are solutions to the unperturbed equations, from Eqs. (5.4) and (5.5) we have

$$A_z \ddot{g}_{z1} + B_z \ddot{g}_{z2} + (a_z + 2q_z \cos 2\tau)(A_z g_{z1} + B_z g_{z2}) = 0 \tag{5.22}$$

$$A_r\ddot{g}_{r1} + B_r\ddot{g}_{r2} + (a_r + 2q_r\cos 2\tau)\,(A_r g_{r1} + B_r g_{r2}) = 0 \tag{5.23}$$

Substituting Eqs. (5.22) and (5.23) in Eqs. (5.20) and (5.21) we get

$$\dot{A}_z\dot{g}_{z1} + \dot{B}_z\dot{g}_{z2} = -\epsilon F_1 \tag{5.24}$$

$$\dot{A}_r\dot{g}_{r1} + \dot{B}_r\dot{g}_{r2} = -\epsilon F_2 \tag{5.25}$$

To solve for $\dot{A}_z$, $\dot{B}_z$, $\dot{A}_r$, $\dot{B}_r$, we need two more equations, obtained by differentiating Eqs. (5.16) and (5.17) with respect to τ and comparing them with Eqs. (5.18) and (5.19), giving

$$\dot{A}_z g_{z1} + \dot{B}_z g_{z2} = 0 \tag{5.26}$$

$$\dot{A}_r g_{r1} + \dot{B}_r g_{r2} = 0 \tag{5.27}$$

Solving Eqs. (5.24), (5.25), (5.26) and (5.27) we get

$$\dot{A}_z = \frac{\epsilon F_1 g_{z2}}{\dot{g}_{z1}g_{z2} - \dot{g}_{z2}g_{z1}}; \quad \dot{B}_z = \frac{\epsilon F_1 g_{z1}}{\dot{g}_{z2}g_{z1} - \dot{g}_{z1}g_{z2}} \tag{5.28}$$

$$\dot{A}_r = \frac{\epsilon F_2 g_{r2}}{\dot{g}_{r1}g_{r2} - \dot{g}_{r2}g_{r1}}; \quad \dot{B}_r = \frac{\epsilon F_2 g_{r1}}{\dot{g}_{r2}g_{r1} - \dot{g}_{r1}g_{r2}} \tag{5.29}$$

The above equations represent the dynamics of the original system.

5.3.2 Verification of modified equations

Equations (5.28) and (5.29) are modified equations which transform $\bar{z}$-$\dot{\bar{z}}$ and $\bar{r}$-$\dot{\bar{r}}$ co-ordinates of the original equations into A_z-B_z and A_r-B_r co-ordinates. In principle, there is no approximation so far, since this is only a change of variables. However, we have used harmonic balance to approximately determine the periodic functions (g's) used here. For validation of the approximations made so far, a comparison of solutions obtained from the modified equations with those from the original equations are presented in Fig. 5.3.

In Fig. 5.3, the initial conditions for the modified equations are arbitrarily selected as $(A_z, B_z, A_r, B_r) = (0.2439, 0.2439, 0.2439, 0.2439)$. We choose the initial conditions for the original equations by transforming these initial conditions to $\bar{z}$-$\dot{\bar{z}}$ and $\bar{r}$-$\dot{\bar{r}}$ by using Eqs. (5.16), (5.17), (5.18) and (5.19) at $\tau = 0$. The initial values of $(\bar{z}, \dot{\bar{z}}, \bar{r}, \dot{\bar{r}})$ are obtained as $(0.1244, 0.1582, 0.3176, 0.0830)$. For the simulation, ϵ is chosen as 0.02 and the parameters $\bar{h}$ and $\bar{f}$ are both taken as 1; and the parameters $\bar{a}_z$ and $\bar{q}_z$ are chosen as -0.3 and 0.1, respectively. The values of $\bar{z}$, $\dot{\bar{z}}$ and $\bar{r}$, $\dot{\bar{r}}$ obtained from numerical integration of the original equations of motion are transformed back into A_z, B_z and A_r, B_r for comparison, using Eqs. (5.16), (5.17), (5.18) and (5.19). These values, obtained from the original equations, are called A_{zeval}, B_{zeval} and A_{reval}, B_{reval}. Figures 5.3(a) and 5.3(b) show the results obtained for $\tau = 5000$, which corresponds to about 1600 rf cycles. In other words,

the curves drawn are actually the envelopes of about 400 cycles of slowly modulated, almost periodic functions. Agreement over this rather long time shows that the modified equations, in spite of the harmonic balance approximations made, faithfully represent the original dynamics. We henceforth accept these modified equations as accurate.

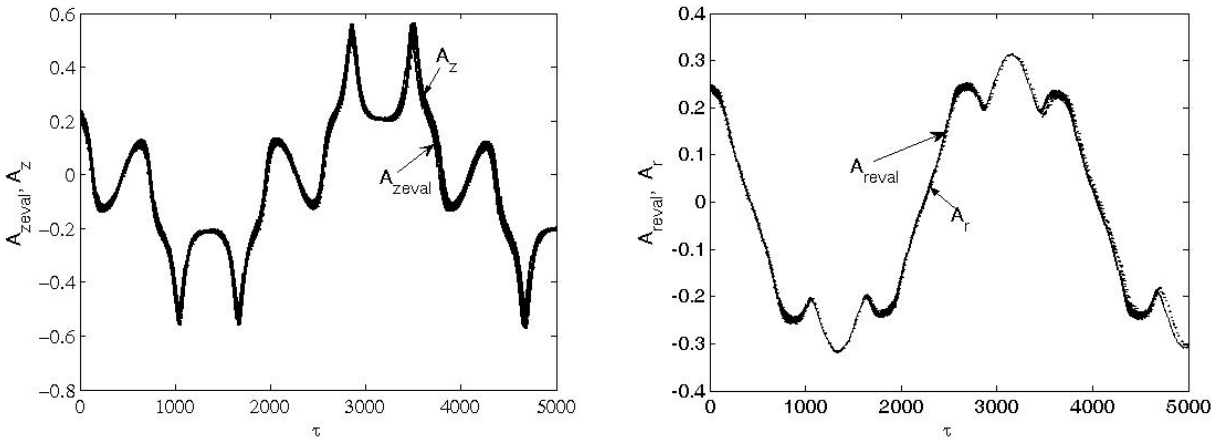

(a) (b)

Figure 5.3: (a) A_{zeval} (from original equations) and A_z (modified equations) versus time (b) A_{reval} (from original equations) and A_r (modified equations) versus time for $\epsilon = 0.02$, $\bar{h} = \bar{f} = 1$, $\bar{a}_z = -0.3$, $\bar{q}_z = 0.1$.

Also, in the interest of limiting our search somewhat, all subsequent *numerical* results are generated for parameters $\bar{a}_z$ and $\bar{q}_z$ chosen as -0.3 and 0.1, respectively. We also arbitrarily fix the numerical value of ϵ in simulations at 0.02. A more detailed investigation of other parameter values is left for future work.

5.3.3 Averaging

We next carry out averaging up to second order, which involves a tedious calculation made practical by symbolic algebra programs (see, e.g., Rand and Armbruster, 1987).

A key point in the averaging calculation is that the denominators of the right hand sides of Eqs. (5.28) and (5.29) turn out to be essentially constants (we drop some small oscillating parts with numerical coefficient's of about 10^{-4} or lower, since these are comparable to other approximations we are making along the way). The constancy of the denominator allows the usual averaging procedure to be carried out more easily.

Since ϵ is small the variation of $\dot{A}_z$, $\dot{B}_z$, $\dot{A}_r$, $\dot{B}_r$ is slow with respect to time and these are approximately constant over one period of g_z1, g_z2, g_r1 and g_r2. Consequently

averaging these equations over the period 4π will give us the required slow flow equations to first order (Verhulst, 1990). The first order averaged are given in Section 5.6.2

The first order averaged equations do not contain terms with $\bar{h}$ which corresponds to the hexapole superposition. This term was, however, seen to play a role in making the system unstable in both r and z directions in our numerical study. In view of this we will seek a second order averaged equation to introduce hexapole superposition's contribution to ion dynamics at the resonance point.

In order to derive the second order averaged equations we introduce near-identity transformations. The near-identity transformation for A_z, B_z, A_r and B_r are as follows:

$$A_z = \bar{A}_z + \epsilon\, W_{z1}\left(\bar{A}_z, \bar{B}_z, \bar{A}_r, \bar{B}_r, \tau\right) + \epsilon^2\, W_{z2}\left(\bar{A}_z, \bar{B}_z, \bar{A}_r, \bar{B}_r, \tau\right) \tag{5.30}$$

$$B_z = \bar{B}_z + \epsilon\, V_{z1}\left(\bar{A}_z, \bar{B}_z, \bar{A}_r, \bar{B}_r, \tau\right) + \epsilon^2\, V_{z2}\left(\bar{A}_z, \bar{B}_z, \bar{A}_r, \bar{B}_r, \tau\right) \tag{5.31}$$

$$A_r = \bar{A}_r + \epsilon\, W_{r1}\left(\bar{A}_z, \bar{B}_z, \bar{A}_r, \bar{B}_r, \tau\right) + \epsilon^2\, W_{r2}\left(\bar{A}_z, \bar{B}_z, \bar{A}_r, \bar{B}_r, \tau\right) \tag{5.32}$$

$$B_r = \bar{B}_r + \epsilon\, V_{r1}\left(\bar{A}_z, \bar{B}_z, \bar{A}_r, \bar{B}_r, \tau\right) + \epsilon^2\, V_{r2}\left(\bar{A}_z, \bar{B}_z, \bar{A}_r, \bar{B}_r, \tau\right) \tag{5.33}$$

where $\bar{A}_z$, $\bar{B}_z$, $\bar{A}_r$, $\bar{B}_r$ are averaged quantities, and W_{z1}, W_{z2}, V_{z1}, V_{z2}, W_{r1}, W_{r2}, V_{r1}, V_{r2} are functions yet to be determined. In order to obtain $\dot{A}_z, \dot{B}_z, \dot{A}_r, \dot{B}_r$ we differentiate Eqs. (5.30) to (5.33) with respect to τ to get

$$\begin{aligned}
\dot{A}_z &= \epsilon \frac{\partial}{\partial \tau} W_{z1}(\bar{A}_z, \bar{B}_z, \bar{A}_r, \bar{B}_r, \tau) + \epsilon^2 \frac{\partial}{\partial \tau} W_{z2}(\bar{A}_z, \bar{B}_z, \bar{A}_r, \bar{B}_r, \tau) \\
&\quad + \left(1 + \epsilon \frac{\partial}{\partial \bar{A}_z} W_{z1}(\bar{A}_z, \bar{B}_z, \bar{A}_r, \bar{B}_r, \tau) + \epsilon^2 \frac{\partial}{\partial \bar{A}_z} W_{z2}(\bar{A}_z, \bar{B}_z, \bar{A}_r, \bar{B}_r, \tau)\right) \dot{\bar{A}}_z \\
&\quad + \left(\epsilon \frac{\partial}{\partial \bar{B}_z} W_{z1}(\bar{A}_z, \bar{B}_z, \bar{A}_r, \bar{B}_r, \tau) + \epsilon^2 \frac{\partial}{\partial \bar{B}_z} W_{z2}(\bar{A}_z, \bar{B}_z, \bar{A}_r, \bar{B}_r, \tau)\right) \dot{\bar{B}}_z
\end{aligned} \tag{5.34}$$

$$\begin{aligned}
\dot{B}_z &= \epsilon \frac{\partial}{\partial \tau} V_{z1}(\bar{A}_z, \bar{B}_z, \bar{A}_r, \bar{B}_r, \tau) + \epsilon^2 \frac{\partial}{\partial \tau} V_{z2}(\bar{A}_z, \bar{B}_z, \bar{A}_r, \bar{B}_r, \tau) \\
&\quad + \left(1 + \epsilon \frac{\partial}{\partial \bar{A}_z} V_{z1}(\bar{A}_z, \bar{B}_z, \bar{A}_r, \bar{B}_r, \tau) + \epsilon^2 \frac{\partial}{\partial \bar{A}_z} V_{z2}(\bar{A}_z, \bar{B}_z, \bar{A}_r, \bar{B}_r, \tau)\right) \dot{\bar{A}}_z \\
&\quad + \left(\epsilon \frac{\partial}{\partial \bar{B}_z} V_{z1}(\bar{A}_z, \bar{B}_z, \bar{A}_r, \bar{B}_r, \tau) + \epsilon^2 \frac{\partial}{\partial \bar{B}_z} V_{z2}(\bar{A}_z, \bar{B}_z, \bar{A}_r, \bar{B}_r, \tau)\right) \dot{\bar{B}}_z
\end{aligned} \tag{5.35}$$

$$\begin{aligned}
\dot{A}_r &= \epsilon \frac{\partial}{\partial \tau} W_{z1}(\bar{A}_z, \bar{B}_z, \bar{A}_r, \bar{B}_r, \tau) + \epsilon^2 \frac{\partial}{\partial \tau} W_{z2}(\bar{A}_z, \bar{B}_z, \bar{A}_r, \bar{B}_r, \tau) \\
&\quad + \left(1 + \epsilon \frac{\partial}{\partial \bar{A}_r} W_{z1}(\bar{A}_z, \bar{B}_z, \bar{A}_r, \bar{B}_r, \tau) + \epsilon^2 \frac{\partial}{\partial \bar{A}_r} W_{z2}(\bar{A}_z, \bar{B}_z, \bar{A}_r, \bar{B}_r, \tau)\right) \dot{\bar{A}}_r \\
&\quad + \left(\epsilon \frac{\partial}{\partial \bar{B}_r} W_{z1}(\bar{A}_z, \bar{B}_z, \bar{A}_r, \bar{B}_r, \tau) + \epsilon^2 \frac{\partial}{\partial \bar{B}_r} W_{z2}(\bar{A}_z, \bar{B}_z, \bar{A}_r, \bar{B}_r, \tau)\right) \dot{\bar{B}}_r
\end{aligned} \tag{5.36}$$

$$\begin{aligned}\dot{B}_r &= \epsilon \frac{\partial}{\partial \tau} V_{z1}(\bar{A}_z, \bar{B}_z, \bar{A}_r, \bar{B}_r, \tau) + \epsilon^2 \frac{\partial}{\partial \tau} V_{z2}(\bar{A}_z, \bar{B}_z, \bar{A}_r, \bar{B}_r, \tau) \\ &+ \left(1 + \epsilon \frac{\partial}{\partial \bar{A}_r} V_{z1}(\bar{A}_z, \bar{B}_z, \bar{A}_r, \bar{B}_r, \tau) + \epsilon^2 \frac{\partial}{\partial \bar{A}_r} V_{z2}(\bar{A}_z, \bar{B}_z, \bar{A}_r, \bar{B}_r, \tau)\right) \dot{\bar{A}}_r \\ &+ \left(\epsilon \frac{\partial}{\partial \bar{B}_r} V_{z1}(\bar{A}_z, \bar{B}_z, \bar{A}_r, \bar{B}_r, \tau) + \epsilon^2 \frac{\partial}{\partial \bar{B}_r} V_{z2}(\bar{A}_z, \bar{B}_z, \bar{A}_r, \bar{B}_r, \tau)\right) \dot{\bar{B}}_r \end{aligned} \tag{5.37}$$

Since $\dot{A}_z$, $\dot{B}_z$, $\dot{A}_r$ and $\dot{B}_r$ are of $O(\epsilon)$ and $\bar{A}_z$, $\bar{B}_z$, $\bar{A}_r$ and $\bar{B}_r$ are close to A_z, B_z, A_r and B_r, therefore $\dot{\bar{A}}_z$, $\dot{\bar{B}}_z$ $\dot{\bar{A}}_r$ and $\dot{\bar{B}}_r$ are also of $O(\epsilon)$. For book keeping we write

$$\dot{\bar{A}}_z = \epsilon\, \dot{\bar{A}}_{z1} + \epsilon^2\, \dot{\bar{A}}_{z2} \tag{5.38}$$

$$\dot{\bar{B}}_z = \epsilon\, \dot{\bar{B}}_{z1} + \epsilon^2\, \dot{\bar{B}}_{z2} \tag{5.39}$$

$$\dot{\bar{A}}_r = \epsilon\, \dot{\bar{A}}_{r1} + \epsilon^2\, \dot{\bar{A}}_{r2} \tag{5.40}$$

$$\dot{\bar{B}}_r = \epsilon\, \dot{\bar{B}}_{r1} + \epsilon^2\, \dot{\bar{B}}_{r2} \tag{5.41}$$

We now use the method outlined in Rand (1994) to derive the second order averaged equations which are given in Section 5.6.3 (where numerical coefficients have been replaced with rational approximations).

To confirm that the second order averaged equations are useful we compare the solutions obtained from them with those obtained from the original equations. This comparison is presented in Fig. 5.4. The initial conditions for the averaged equations and the original equations are the same as in Fig. 5.3. Here too, we transform the values of $\bar{z}$, $\dot{\bar{z}}$ and $\bar{r}$, $\dot{\bar{r}}$ obtained from numerical integration of the original equations of motion back into A_z, B_z and A_r, B_r, using Eqs. (5.16), (5.17), (5.18) and (5.19). The figure shows that there is now a small error in the time scale of the modulation dynamics; however, the shape of the curve is faithfully retained, and so we expect that qualitative conclusions drawn from the averaged equations will remain valid. In principle, tightening the harmonic balance and subsequent approximations, as well as using smaller values of ϵ, should improve the match.

Readers interested in error analysis (which we do not attempt here) may note that, before averaging, the transformed equations contained errors only due to harmonic balance approximations. Now, after averaging, there are further errors that go to zero as $\epsilon \to 0$. The formal guarantees for averaging, even in the absence of harmonic balance errors, hold for time scales of $\mathcal{O}(1/\epsilon)$. Here, we have used $\epsilon = 0.02$, whence $1/\epsilon = 50$, but we are looking at time scales of a few thousands, which is large. Thus, the results of Fig. 5.4 are actually quite good.

It may be noted that the original system is Hamiltonian. We have verified that the

averaged equations also satisfy the Hamiltonian conditions

$$\frac{\partial \dot{A}_z}{\partial A_z} + \frac{\partial \dot{B}_z}{\partial B_z} = 0 \tag{5.42}$$

and

$$\frac{\partial \dot{A}_r}{\partial A_r} + \frac{\partial \dot{B}_r}{\partial B_r} = 0. \tag{5.43}$$

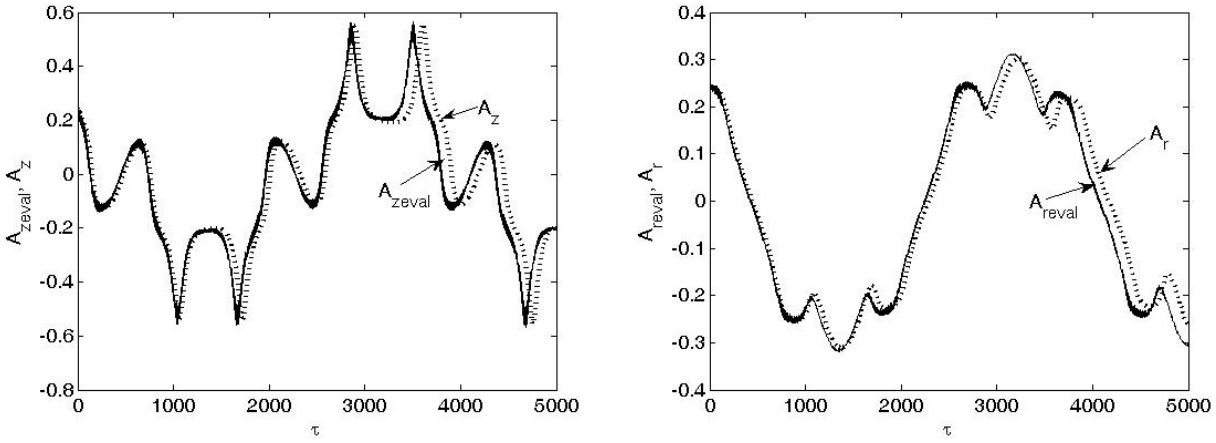

(a) (b)

Figure 5.4: (a) A_{zeval} (from original equations) and A_z (averaged equations) versus time and (b) A_{reval} (from original equations) and A_r (averaged equations) versus time for $\epsilon = 0.02$, $\bar{h} = \bar{f} = 1$, $\bar{a}_z = -0.3$, $\bar{q}_z = 0.1$.

The dynamics of Hamiltonian systems comprises a mature subject, and the reader is referred to, e.g., Ott (1993) and Hilborn (1994) for introductions. However, no formal exploitation of the Hamiltonian structure of the averaged system is attempted in this chapter. Instead, faced with the formidable analytical form of the averaged equations, as well as the presence of four free parameters (two for detuning in the operating point and two for the relative strengths of nonlinear terms), we will confine ourselves to a numerical study of the dynamics of some solutions of this system. As stated in the introduction of this chapter, we will choose specific but arbitrary parameter values; study the stability of the individual radial and axial motion invariant manifolds; examine the rather large times associated with escape of ions; notice regions in the averaged phase space wherein trajectories do not, in fact, escape; observe apparently chaotic dynamics preceding escape for ions that do escape; and note that trajectories that do not escape appear to be confined to 4-tori.

5.4 Numerical investigation of the averaged equations

Henceforth, we use

$$\bar{\tau} = \epsilon\,\tau.$$

We will look at $\bar{\tau}$ on the order of 1000-10000. In our study of this system, we do not aim for a complete understanding of this system. Rather, we are able to demonstrate some interesting behavior in this system, as mentioned above, by a process of successively limiting our search in a sequence of steps. Further detailed understanding of this system may emerge with future work.

5.4.1 Invariant manifolds

To begin our study of the averaged equations, we first study the two invariant manifolds, $(A_z = B_z = 0)$ and $(A_r = B_r = 0)$, which represent the uncoupled dynamics. Our study of near-resonant dynamics, near the intersection of $\beta_z = \frac{1}{2}$, $\beta_r = \frac{1}{2}$ and $\beta_z + \beta_r = 1$, will eventually be carried out using initial conditions that are close to these invariant manifolds (the computed trajectories may travel far from these manifolds, however).

We now generate the phase portraits for these two invariant manifolds. Figure 5.5(a) is the phase portrait of A_r-B_r in the invariant manifold $(A_z = B_z = 0)$. It can be observed that the uncoupled r direction ion motion is stable at the origin. There are additional fixed points away from the origin. Figure 5.5(b) is the phase portrait of A_z-B_z in the invariant manifold $(A_r = B_r = 0)$. Here too the ion motion is stable at the center and there exist fixed points away from the center. These observations are consistent with the initial study of the original system using Poincaré sections (as is well understood, the Poincaré map is approximated by the slow flow).

5.4.2 Neighborhoods of invariant manifolds

We now move slightly away from the two invariant manifolds.

The dynamics in the vicinity of the invariant manifold $(A_z = B_z = 0)$ is investigated by linearizing the averaged equations for A_z and B_z nonzero but small (note that A_r and B_r are not small).

Under these conditions we can neglect the terms involving A_z^2, B_z^2, $A_z B_z$ and higher order terms involving A_z and B_z in the slow flow equations. The resulting equations are of the form

$$\dot{A}_z = f_1(A_r, B_r)A_z + f_2(A_r, B_r)B_z \tag{5.44}$$

$$\dot{B}_z = g_1(A_r, B_r)A_z + g_2(A_r, B_r)B_z \tag{5.45}$$

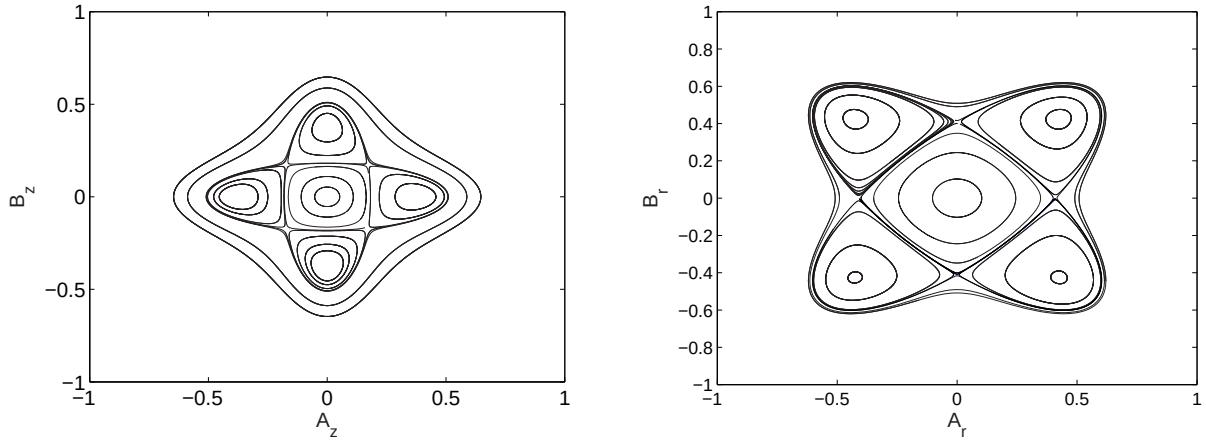

(a) (b)

Figure 5.5: Phase portraits generated for the invariant manifolds (a) $(A_r = 0, B_r = 0)$ and (b) $(A_z = 0, B_z = 0)$ for $\epsilon = 0.02$, $\bar{h} = \bar{f} = 1$, $\bar{a}_z = -0.3$, $\bar{q}_z = 0.1$.

$$\dot{A}_r = h_1(A_r, B_r) \tag{5.46}$$

and

$$\dot{B}_r = h_2(A_r, B_r) \tag{5.47}$$

where $f_1, f_2, g_1, g_2, h_1, h_2$ are functions of A_r and B_r (the long expressions involved are not presented here). It turns out that A_z and B_z do not appear in the A_r and B_r equations at all. If the solutions for A_r and B_r are periodic which they mostly are, then the linear dynamics of A_z and B_z involves time-periodic coefficients, and could show exponential instabilities (as per Floquet theory, which we do not explicitly use here).

We now integrate the above set of equations, linearized in A_z, B_z. We choose randomly generated initial conditions for A_z and B_z. Since the trajectories are symmetric on the A_r-B_r plane (as seen in Fig. 5.5(b)) it is sufficient to investigate only the first quadrant of the A_r-B_r plane. The initial conditions for A_r and B_r are considered along a grid of 300×300 points with A_r and B_r varying from 0 to 1. The numerical integration of the ODEs is carried out for a time $\bar{\tau} = 1000$. With a view to delineating stable and unstable regions we use a measure of the average exponential growth in the magnitudes of A_z and B_z. This is done by calculating

$$\lambda_z(\bar{\tau}) = \ln\left(\sqrt{A_z(\bar{\tau})^2 + B_z(\bar{\tau})^2}\right) \tag{5.48}$$

for each set of initial conditions. Then the exponent

$$\sigma_z = \lim_{\bar{\tau}\to\infty} \frac{1}{\bar{\tau}} \lambda(\bar{\tau}) \approx \frac{\lambda(1000)}{1000} \tag{5.49}$$

is a measure of the growth of the amplitude in the z direction. We calculate the parameter σ_z for the 300×300 points chosen in the grid. Positive values of σ_z indicate unstable behavior whereas zero values (in our numerical work, values close to zero) suggest stable behavior. Figure 5.6(a) shows the results. The ring-like regions of instability presumably correspond to combinations of amplitude and frequency of the parametric forcing in the A_z and B_z equations that cause exponential growth. The several distinct 'rings' each clearly correspond to disjoint sets of contiguous periodic solutions of A_r and B_r. While an analytical Floquet treatment of the equations is not attempted here, we point out that different periodic solutions of A_r and B_r correspond to different amplitudes and frequencies of parametric forcing in the A_z and B_z equations, and the alternating 'rings' of instability qualitatively correspond to the passage through alternating instability regions of a curve on, to draw a parallel, the plane of parameters of the familiar linear Mathieu equation.

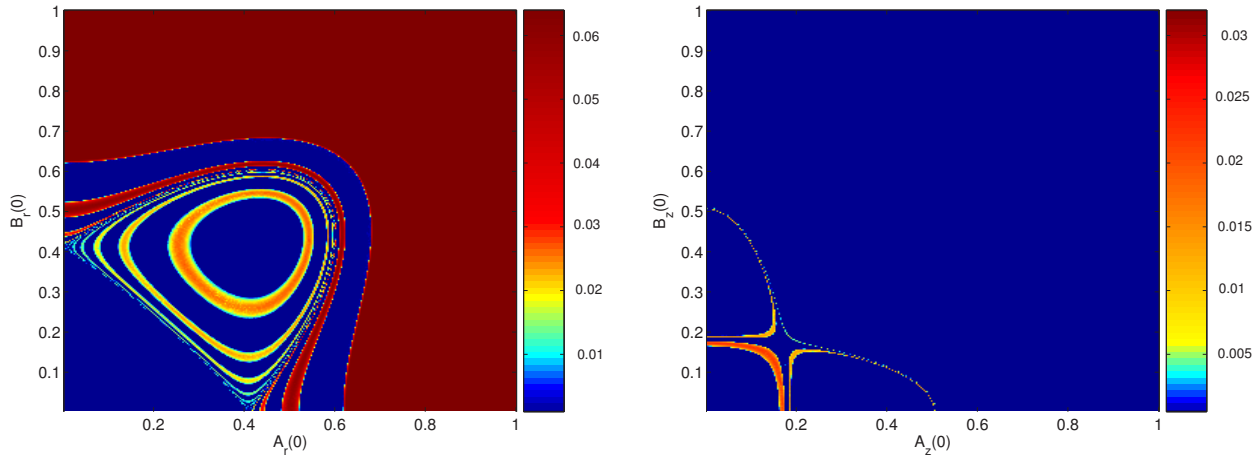

(a) (b)

Figure 5.6: Stability of invariant manifolds (a) ($A_z = 0$, $B_z = 0$) (b) ($A_r = 0$, $B_r = 0$). See text for details.

The same procedure is repeated for studying the stability of the invariant subspace $A_r = 0$ and $B_r = 0$. Here we linearize the A_r and B_r terms in the averaged equations, and retain terms nonlinear in A_z and B_z. Results (σ_r values) are shown in Fig. 5.6(b). Much of the region shown is stable in this case (in contrast to the previous case), though some small unstable regions ('rings' again) are seen.

The primary qualitative conclusion from the analysis so far is that large regions on the invariant manifolds are actually stable; and thus, there are several nonzero sized regions in the 4-dimensional averaged phase space from which unbounded trajectories do not arise.

In other words, there are nonzero sized regions of the phase space which contain bounded trajectories.

Yet, there are also regions on the invariant manifolds which are *unstable*, and trajectories starting close to such regions diverge from the unstable manifold. Can some such trajectories be unbounded, leading to escape of the ion? Can some other trajectories remain bounded? We find below, based on a study near one arbitrarily chosen point, that both answers are in the affirmative, although they involve complex dynamics which we can only partially explore in this chapter.

5.4.3 Further investigation of specific solutions

Figure 5.6(b) indicates that the dominant behavior of the ion motion in the neighborhood of the invariant manifold ($A_r = 0$, $B_r = 0$) in the grid of ($A_z(0)$, $B_z(0)$) involves bounded ion trajectories. However, some portions of the invariant manifold are unstable.

We select a point in one such region, where the initial conditions for A_z and B_z are $A_z(0) = 0.1$ and $B_z(0) = 0.15$ (an arbitrary choice), for further investigation.

We further choose two sets of initial conditions for A_r and B_r. These are (i) $A_r(0) = 0.2215$, $B_r(0) = 0.1609$ and (ii) $A_r(0) = 0.1369$, $B_r(0) = 0.2371$. Note that the value of $\sqrt{A_r(0)^2 + B_r(0)^2}$ is 0.2738 in both cases, i.e., the magnitudes are the same though the phases are different.

Figure 5.7(a) shows the solution for the first set ($A_r(0) = 0.2215$, $B_r(0) = 0.1609$). The integration is carried out for $\bar{\tau}$ from 0 to 3000. The trajectories seem stable and periodic, though large departures occur from the ($A_r = 0$, $B_r = 0$) invariant manifold. Thus, there are solutions *not* confined close to the invariant manifolds that nevertheless appear to remain bounded and periodic or near-periodic for at least an extended period of time (the figure shows only 1/30 of the full duration of the simulation).

In contrast to the above, Fig. 5.7(b) shows the plots of A_z, B_z and A_r, B_r versus $\bar{\tau}$ for the other set of initial conditions ($A_r(0) = 0.1369$ and $B_r(0) = 0.2371$). Now, after a long time, and without any obvious warning, the solutions develop a larger amplitude, aperiodic structure and then, again without discernible warning, escape to infinity at about $\bar{\tau} = 1,990$. The aperiodic motions preceding final escape appear chaotic, and are expected to be chaotic within the Hamiltonian context (see Ott, 1993); however, given the finite time of such motions preceding escape, we have not conducted formal checks for chaos.

5.4.4 Probabilities of escape

The possibility of escape, and its dependence on initial conditions, is investigated further below. We consider a larger grid of initial conditions for A_r and B_r while still keeping $A_z(0)$, $B_z(0)$ fixed at 0.1 and 0.15, respectively.

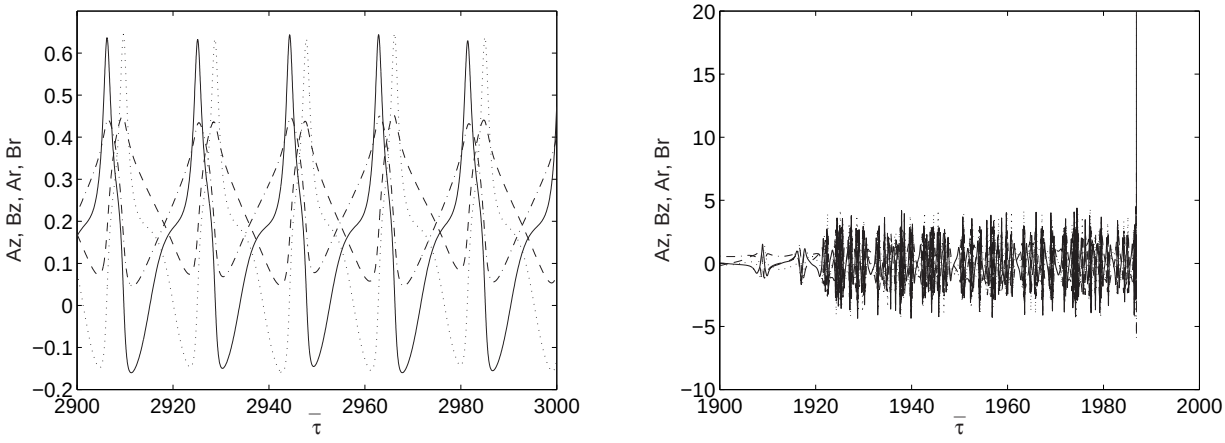

(a) (b)

Figure 5.7: Zoomed portion of the plot of A_z (-), B_z (..), A_r (- -) and B_r (- . -) for (a) $A_r(0) = 0.2215$ and $B_r(0) = 0.1609$ (b) $A_r(0) = 0.1369$ and $B_r(0) = 0.2371$.

The grid of initial conditions for A_r and B_r is chosen by first defining $A_r(0) = R\cos\theta$ and $B_r(0) = R\sin\theta$. By varying R and θ we generate different initial conditions for A_r and B_r. In the present study R has been varied between 0.0001 and 0.5 in 100 steps on a logarithmic scale. (Few initial states below $R = 0.0001$ grew unbounded within our integration duration ($\bar{\tau} = 12,000$) and very many initial states above $R = 0.5$ escaped within this duration.) Also, θ is chosen as $\theta = \frac{2\pi k}{N}$ where $N = 300$ and k varies from 1 to 300. Thus, our numerical investigation involves 30,000 initial conditions for A_r and B_r (while still keeping $A_z(0)$, $B_z(0)$ fixed at 0.1 and 0.15, respectively).

The integration is carried out for $\bar{\tau} = 12000$ which is rather long because $\bar{\tau} = \epsilon\tau$, as mentioned above. We look for the instability (escape) of solutions of the averaged equation within three different times: $\bar{\tau} = 3000$, 6000 and 12000. We keep count of the number of initial conditions of θ for a given R which results in unstable trajectories (escape). This count is used to estimate the probability that an ion will escape within a given time, if it starts from a given value of R.

Figure 5.8 is a plot of the probability of escape versus the value of R. Curve A represents escape before $\bar{\tau} = 3000$, curve B represents escape before $\bar{\tau} = 6000$, and curve C represents escape before $\bar{\tau} = 12000$. For all three curves, for trajectories starting from

small R, the probability of escape within the time of observation is relatively small. Also, for any given R, if a larger time interval is allowed, then the probability of escape increases. As is known to occur for other Hamiltonian systems (see, e.g., Guzzo et al. (2001) and references therein), however, there may be some trajectories that remain bounded over arbitrarily long times of observation.

The figure also shows that, as the initial R value increases, the probability of escape on the whole increases as well, peaking at around $R = 0.14$ before dipping down sharply at about $R = 0.2738$. Except for this dipping down, by and large an increase in R increases the probability of escape within a given time.

5.4.5 Closer look at $R = 0.2738$

The dip at $R = 0.2738$ is interesting especially because it appears in the large initial condition region, a region where we might loosely expect ions to be unstable. Furthermore, this decrease and subsequent increase in probability is seen for plots corresponding to all the three integration times. This reduction in probability suggests that not all the initial conditions along the circle with $R = 0.2738$ are actually escaping: some trajectories are indeed bounded, at least for very long times.

Accordingly, we now explore the dynamics at $R = 0.2738$. Thus, of the 4 possible initial condition components, we are still keeping $A_z(0)$ and $B_z(0)$ fixed at 0.1 and 0.15, respectively; we are further fixing R; and only θ remains as an independent initial condition.

In particular, we consider $\theta = \frac{2\pi k}{600}$, with k varied from 1 to 600. By numerically integrating the averaged equations for time $\bar{\tau} = 12000$ we can determine the values of k for which solutions escape and values for which they do not.

Figure 5.9 shows the results plotted against a normalized k. On the vertical axis, we assign and plot a value of 1 when ion motion is bounded (stable) and a value of 0 when it escapes (unstable). The figure suggests that there are some bands of initial conditions where the solution is bounded and others where it is unbounded.

5.4.6 Further investigation of the dependence on θ

In order to understand Fig. 5.9 we now further study three dimensional plots which depict the evolution of the system. There are two types of plots that we generate.

First, we solve the slow flow equations and plot only B_z, A_r and B_r, dropping A_z. Then, we generate some three dimensional Poincaré sections taken at $A_z = 0$ with A_z

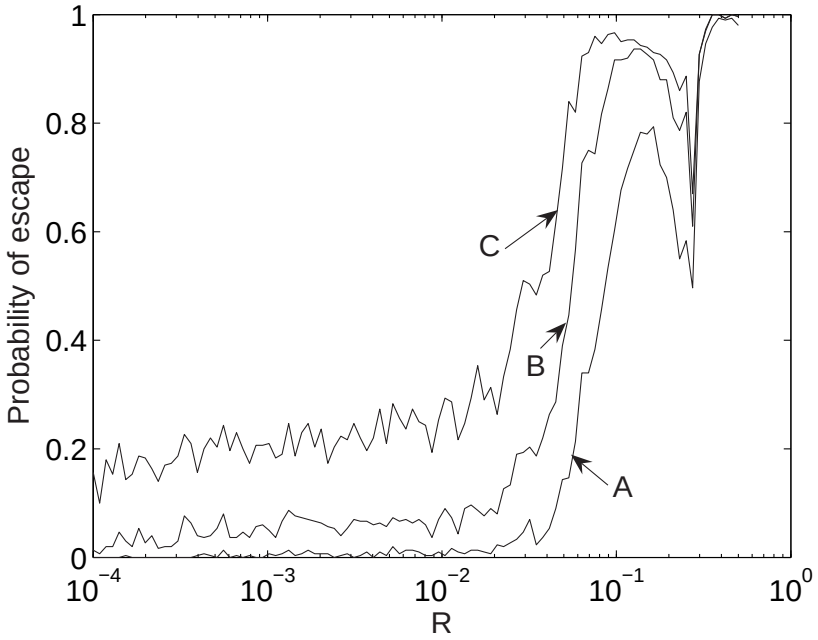

Figure 5.8: Probability of escape versus R for $\bar{\tau} < 3000$ (A), $\bar{\tau} < 6000$ (B), $\bar{\tau} < 12000$ (C).

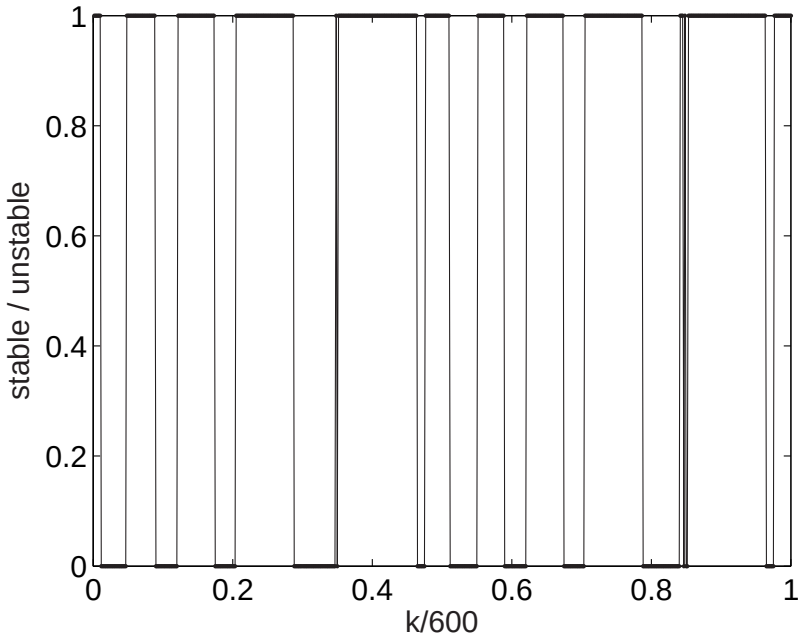

Figure 5.9: Normalized values of k, and hence $\theta/(2\pi)$, for which no escape occurs within $\bar{\tau} = 12000$.

going from positive to negative values (linear interpolation near the zero crossing is used for accurate determination of the points on the section).

In Figs. 5.10 through 5.13 we present the three dimensional trajectories and the corresponding Poincaré sections for four different values of k for which escape does *not* occur. These k values are 27, 63, 197 and 422, and correspond to $\theta = \frac{2\pi k}{600}$ in each case, as mentioned above. The figures suggest that each of these solutions lie on 4-tori, thereby eliminating the possibilities of either chaos or escape; an extremely slow departure from these tori leading to eventual escape, of course, is not ruled out by our finite-time numerics.

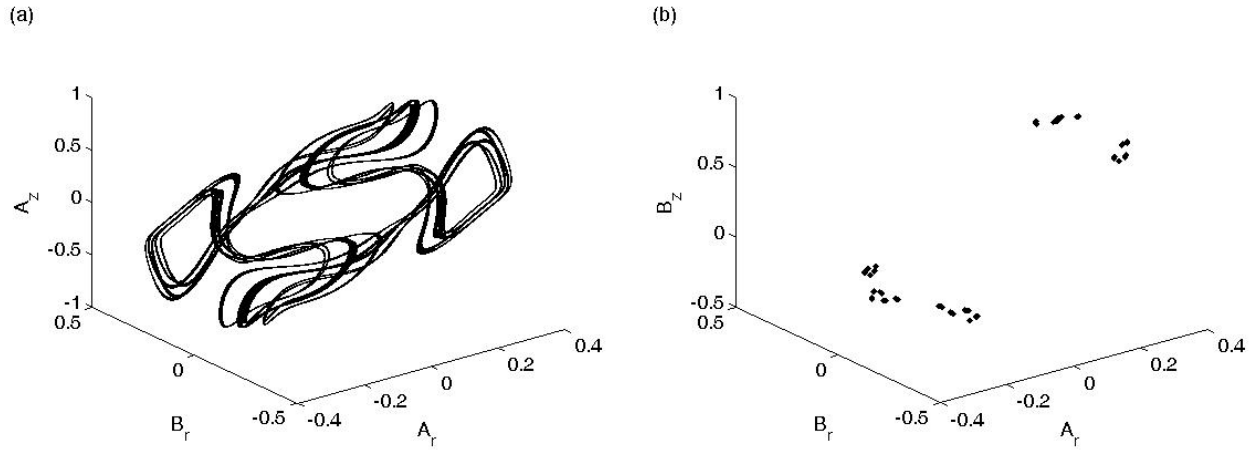

Figure 5.10: (a) Trajectories and (b) Poincaré section for $k = 27$.

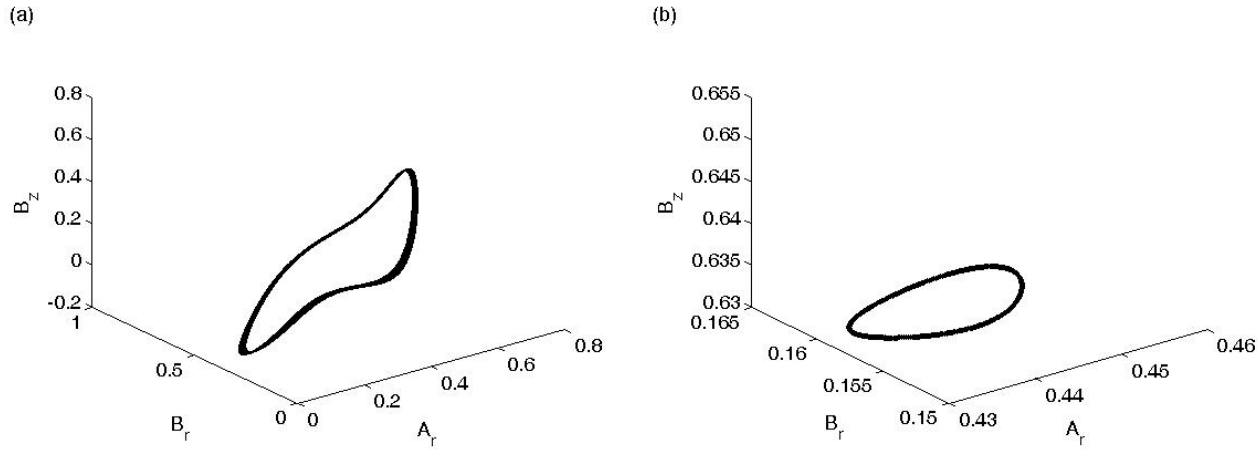

Figure 5.11: (a) Trajectories and (b) Poincaré section for $k = 63$.

We finally turn our attention to *one* transition between bounded and unbounded solutions. We study the system between $k = 28$ (bounded) and $k = 29$ (unbounded),

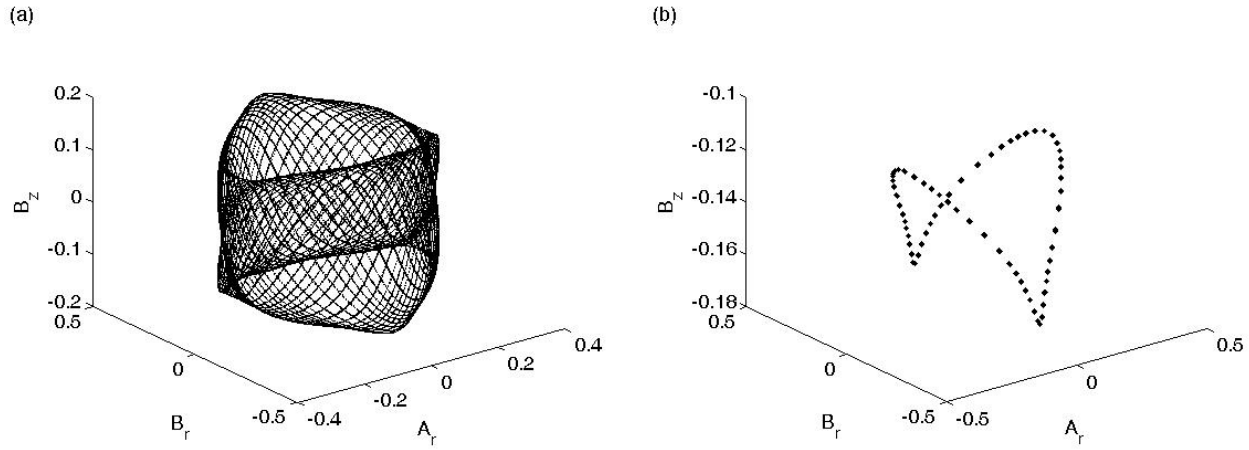

Figure 5.12: (a) Trajectories and (b) Poincaré section for $k = 197$.

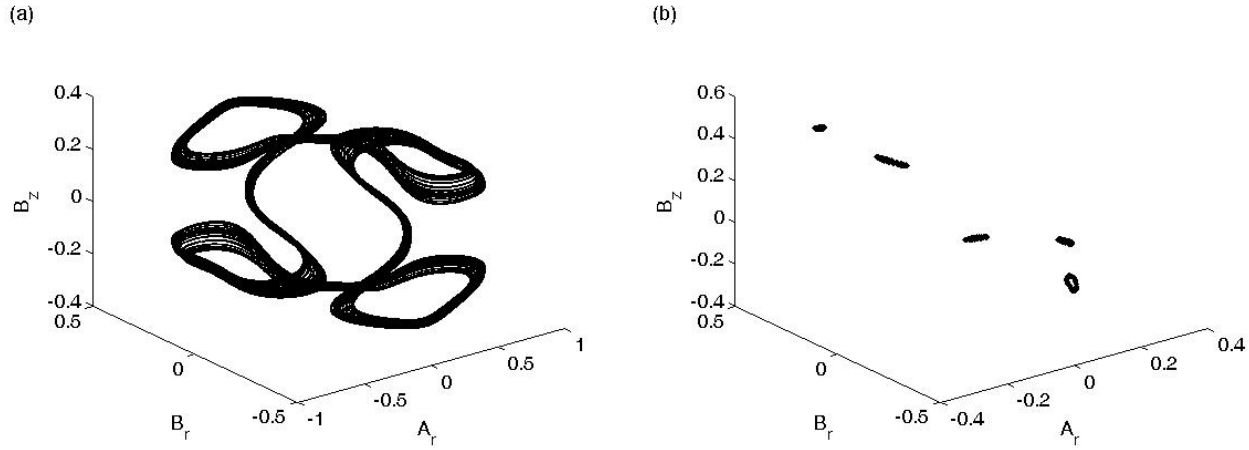

Figure 5.13: (a) Trajectories and (b) Poincaré section for $k = 422$.

allowing fractional values of k. We observed that at $k = 28.7050$ the solution appears bounded and at $k = 28.7060$ the solution is unbounded. As k moves towards instability, the trajectories lose their toroidal structure. This is illustrated in Figs. 5.14 through 5.19 which present time plots, trajectories, and Poincaré sections for $k = 28.7050$ (apparently stable), 28.7055 (visibly borderline) and $k = 28.7060$ (unstable).

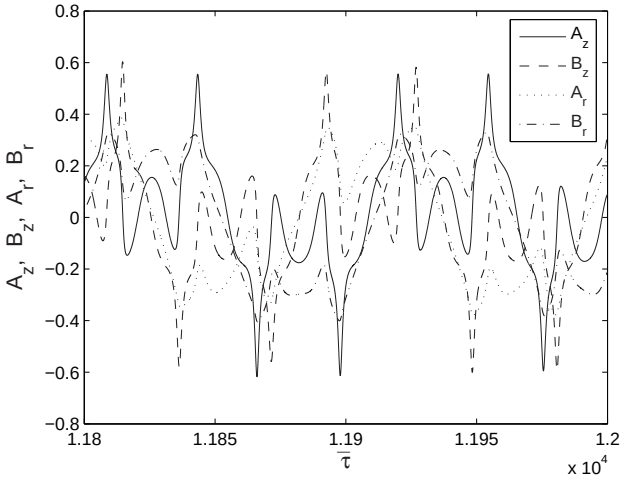

Figure 5.14: Plot of A_z, B_z, A_r, B_r versus τ for $k = 28.7050$.

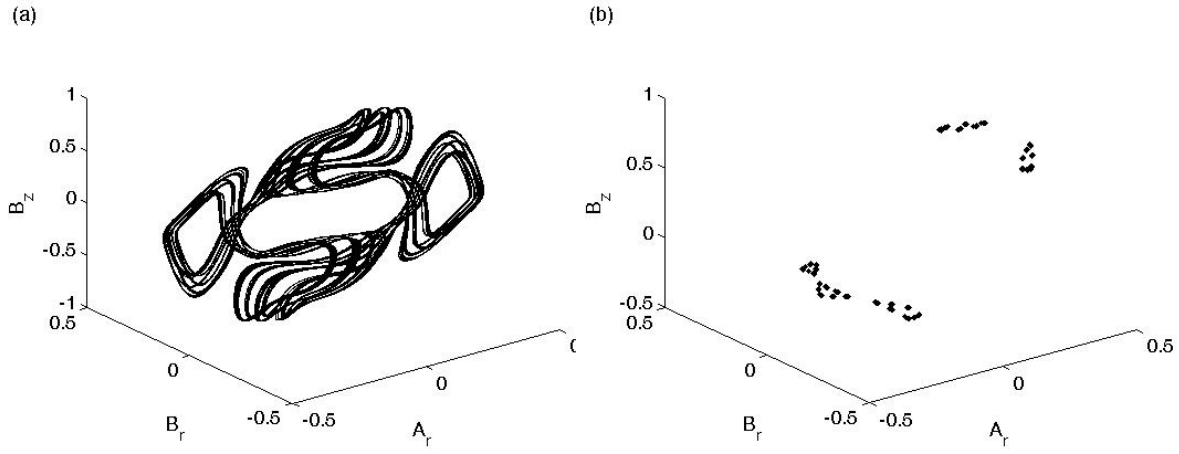

Figure 5.15: Trajectory and Poincaré section for $k = 28.7050$.

Thus, it appears that escape may be typical for trajectories that are not confined to tori (by definition, trajectories confined to tori do not escape).

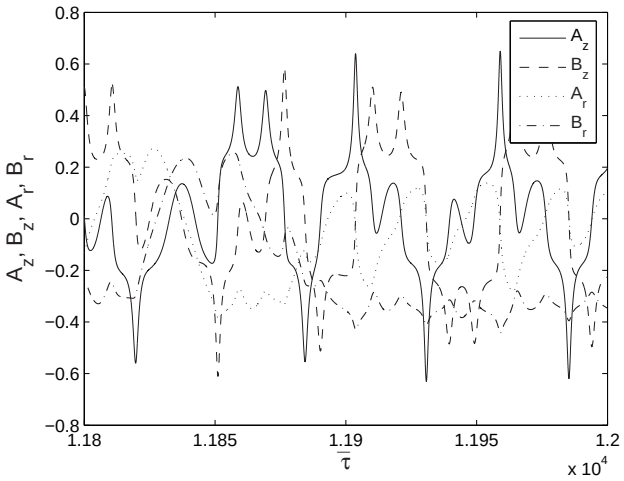

Figure 5.16: Plot of A_z, B_z, A_r, B_r versus τ for $k = 28.7055$.

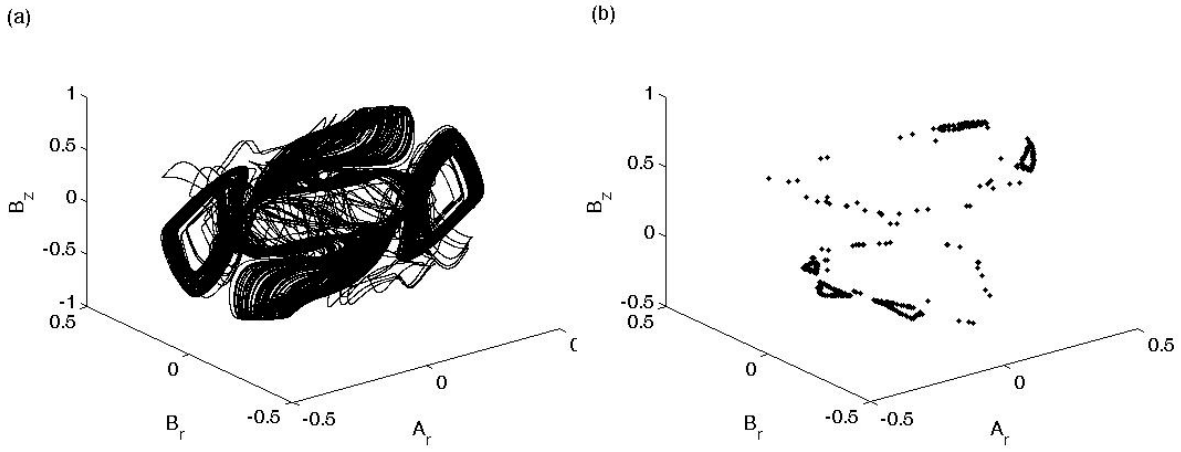

Figure 5.17: Trajectory and Poincaré section for $k = 28.7055$.

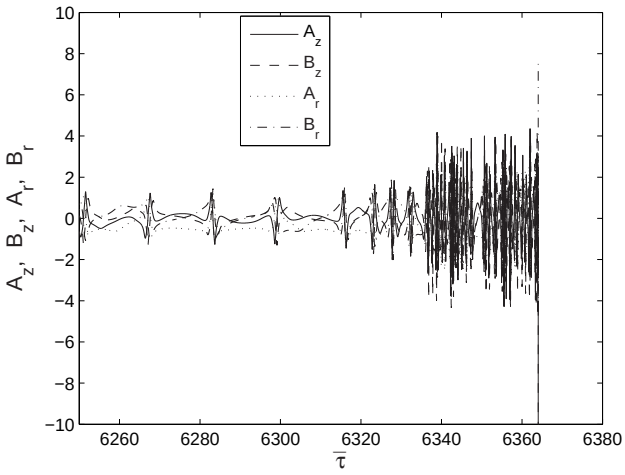

Figure 5.18: Plot of A_z, B_z, A_r, B_r versus τ for $k = 28.7060$.

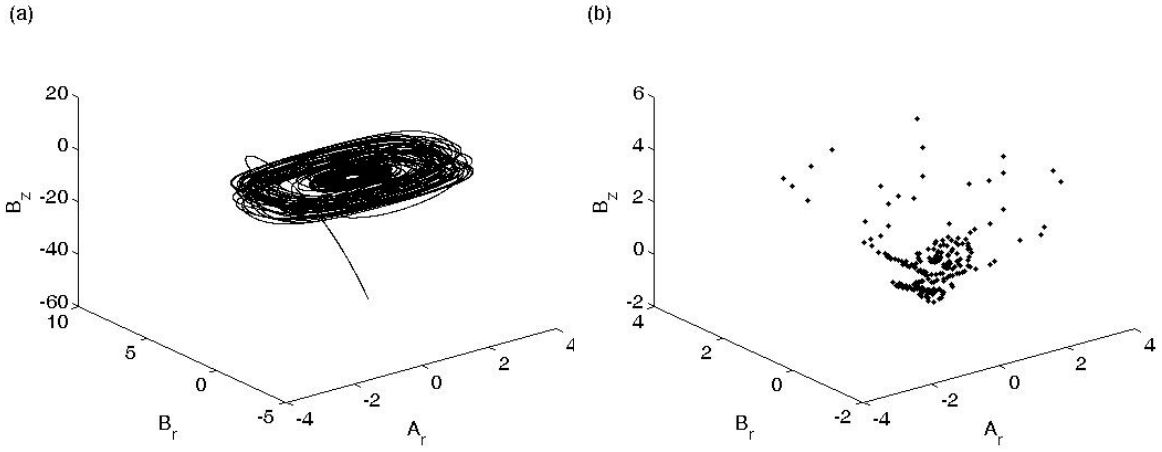

Figure 5.19: Trajectory and Poincaré section for $k = 28.7060$.

5.5 Concluding remarks

The motivation of this study was to explore solutions near the coupled resonance which occurs at $\beta_r = \frac{1}{2}$, $\beta_z = \frac{1}{2}$ and $\beta_r + \beta_z = 1$.

In order to analytically probe the resonance we developed second order averaged equations to approximate the original nonlinear Mathieu equation. Using the averaged equation, we identified on the A_z-B_z and A_r-B_r planes, close to the invariant manifolds, regions where the system becomes unstable. An interesting observation was made in this investigation. For some set of initial conditions in the neighborhood of the invariant manifold ($A_r = 0$, $B_r = 0$), the system was seen to be unstable. One of these points, corresponding to $A_z(0) = 0.1$ and $B_z(0) = 0.15$ was selected for detailed study.

The stability of the system at these points was studied by varying the initial conditions of $A_r(0)$ and $B_r(0)$ as well as by varying the integration times. What emerged from this study was yet another interesting observation, namely that at along particular surface corresponding to $R = 0.2738$, there is a dramatic increase in the stability and the probability of ions getting destabilized suddenly diminishes.

This sudden change in the stability of ions was then probed using three dimensional plots as well as three dimensional Poincaré sections, the latter being obtained by strobing the magnitude of three variables on the zero-crossing of the fourth.

Using harmonic balance based approximate averaging up to second order, we obtained a slow flow that, we have numerically demonstrated, approximates the actual ion dynamics. We have found that the slow flow is Hamiltonian. We have studied the slow flow numerically for specific but arbitrary parameter values; studied the stability of the individual radial and axial motion invariant manifolds; examined the rather large times associated with escape of ions; noticed regions in the averaged phase space wherein trajectories do not, in fact, escape; observed apparently chaotic dynamics preceding escape for ions that do escape; and noted that trajectories that do not escape appear to be confined to 4-tori.

From a mass spectroscopic point of view, this chapter may be contrasted with previous studies of resonance induced ejection of ions from Paul traps (Sudakov, 2001; Abraham et al., 2003; Prasanna, 2005) as follows. In these investigations, only the axial motion (decoupled from the radial motion) was studied numerically and analytically. There, it was found that as the resonant point was approached and crossed, depending on the type of nonlinearity, ions could become inherently unstable with unbounded solutions, or develop periodic modulations that grow in amplitude as parameter cross and go beyond the resonant point. Here, we have studied the system at an arbitrary but fixed point close to the resonant point, i.e., for fixed values of the detuning parameters. However, we

have simultaneously considered motions in both axial and radial directions. Much of the complex behavior observed here can exist only when both radial and axial motions are simultaneously nonzero. In particular, the possibility has not previously been noted in the ion trapping literature that, even if we hold the system fixed near a resonance point, some ions may get ejected sequentially and essentially randomly, and over a long period of time. Moreover, the complex nature of motions inside the trap, preceding escape, has not hitherto been pointed out.

5.6 Appendix

5.6.1 Linearly independent solutions of the unperturbed Mathieu equations at $a_z = -0.2313850427$ and $q_z = 0.9193009931$.

The solutions g_z1, g_z2, g_r1 and g_z2, obtained by harmonic balance, with coefficients replaced with rational approximations are provided below.

$$\begin{aligned} g_{z1}(\tau) &= -\frac{3}{3538}\cos(\beta-6)\tau + \frac{23}{818}\cos(\beta-4)\tau - \frac{315}{827}\cos(\beta-2)\tau \\ &\quad + \cos(\beta\tau) - \frac{184}{1289}\cos(\beta+2)\tau + \frac{13}{2027}\cos(\beta+4)\tau \\ &\quad - \frac{1}{7205}\cos(\beta+6)\tau \end{aligned} \tag{5.50}$$

$$\begin{aligned} g_{z2}(\tau) &= -\frac{3}{3538}\sin(\beta-6)\tau + \frac{23}{818}\sin(\beta-4)\tau - \frac{315}{827}\sin(\beta-2)\tau \\ &\quad + \sin(\beta\tau) - \frac{184}{1289}\sin(\beta+2)\tau + \frac{13}{2027}\sin(\beta+4)\tau \\ &\quad - \frac{1}{7205}\sin(\beta+6)\tau \end{aligned} \tag{5.51}$$

$$\begin{aligned} g_{r1}(\tau) &= \frac{1}{7966}\cos(\beta-6)\tau + \frac{2}{243}\cos(\beta-4)\tau + \frac{38}{175}\cos(\beta-2)\tau \\ &\quad + \cos(\beta\tau) + \frac{31}{413}\cos(\beta+2)\tau + \frac{7}{4084}\cos(\beta+4)\tau \\ &\quad + \frac{1}{53481}\cos(\beta+6)\tau \end{aligned} \tag{5.52}$$

$$\begin{aligned} g_{r2}(\tau) &= \frac{1}{7966}\sin(\beta-6)\tau + \frac{2}{243}\sin(\beta-4)\tau + \frac{38}{175}\sin(\beta-2)\tau \\ &\quad + \sin(\beta\tau) + \frac{31}{413}\sin(\beta+2)\tau + \frac{7}{4084}\sin(\beta+4)\tau \\ &\quad + \frac{1}{53481}\sin(\beta+6)\tau \end{aligned} \tag{5.53}$$

5.6.2 First order slow flow equations.

The slow equations obtained by carrying out out first order averaging are given below.

$$\begin{aligned}\dot{A}_z &= \epsilon\big(0.97382\,\bar{f}\,B_z\,{A_r}^2 - 0.19803\,\bar{f}\,B_z\,{B_r}^2 - 9.3511\,\bar{f}\,A_z^2 B_z \\ &\quad +2.0388\,\bar{f}\,A_z\,A_r\,B_r - 1.6186\,\bar{q}_z\,B_z - 1.7633\,\bar{a}_z\,B_z \\ &\quad -3.0003\,\bar{f}\,{B_z}^3\big) \qquad (5.54)\end{aligned}$$

$$\begin{aligned}\dot{B}_z &= \epsilon\big(1.6186\,\bar{q}_z\,A_z - 2.0388\,\bar{f}\,B_z\,A_r\,B_r + 0.19803\,\bar{f}\,A_z\,{A_r}^2 \\ &\quad -0.97382\,\bar{f}\,A_z\,{B_r}^2 + 9.3511\,\bar{f}\,A_z\,{B_z}^2 + 3.0003\,\bar{f}\,A_z^3 \\ &\quad +1.7633\,\bar{a}_z\,A_z\big) \qquad (5.55)\end{aligned}$$

$$\begin{aligned}\dot{A}_r &= \epsilon\big(-0.14778\,\bar{f}\,{B_z}^2 B_r + 0.72669\,\bar{f}\,{A_z}^2 B_r - 0.093252\,\bar{f}\,{A_r}^2 B_r \\ &\quad +1.5215\,\bar{f}\,A_z\,B_z\,A_r - 0.33185\,\bar{q}_z\,B_r + 0.59396\,\bar{a}_z\,B_r \\ &\quad +1.2699\,\bar{f}\,{B_r}^3\big) \qquad (5.56)\end{aligned}$$

$$\begin{aligned}\dot{B}_r &= \epsilon\big(-0.72669\,\bar{f}\,{B_z}^2 A_r + 0.14778\,\bar{f}\,{A_z}^2 A_r + 0.093252\,\bar{f}\,A_r\,{B_r}^2 \\ &\quad -1.5215\,\bar{f}\,A_z\,B_z\,B_r - 0.59396\,\bar{a}_z\,A_r + 0.33185\,\bar{q}_z\,A_r \\ &\quad -1.2699\,\bar{f}\,{A_r}^3\big) \qquad (5.57)\end{aligned}$$

5.6.3 Second order slow flow equations

The second order slow flow equations, with numerical coefficients approximated using fractions correct up to 4 decimal places, are as follows:

$$
\begin{aligned}
\dot{A}_z \;=\;& \epsilon\left(\frac{36}{37}\,\bar{f}\,B_r\,{A_r}^2-\frac{187}{20}\,\bar{f}\,{A_z}^2B_z-\frac{23}{116}\,\bar{f}\,B_z\,{B_r}^2+\frac{53}{26}\,\bar{f}\,A_z\,A_r\,B_r-3\,\bar{f}\,{B_z}^3\right.\\
&\left.-\frac{34}{21}\,\bar{q}_z\,B_z-\frac{30}{17}\,\bar{a}_z\,B_z\right)\\
&+\epsilon^2\left(\frac{161}{27}\,\bar{f}\,{B_z}^3\bar{a}_z-\frac{46}{15}\,\bar{f}^2{A_r}^2B_z\,{B_r}^2+\frac{37}{73}\,\bar{f}^2A_z\,A_r\,{B_r}^3+\frac{61}{2}\,\bar{f}^2{A_z}^2B_z\,{B_r}^2\right.\\
&+\frac{150}{29}\,\bar{f}\,{B_r}^2\bar{q}_z\,B_z-\frac{37}{28}\,\bar{f}\,{A_r}^2\bar{q}_z\,B_z+\frac{203}{34}\,\bar{f}\,{B_r}^2\bar{a}_z\,B_z+\frac{37}{4}\,\bar{f}^2{A_z}^4B_z\\
&-\frac{23}{28}\,\bar{q}_z^2B_z+\frac{33}{35}\,\bar{f}\,A_r\,B_r\,\bar{a}_z\,A_z+\frac{76}{3}\,\bar{h}^2{B_z}^3-\frac{59}{29}\,\bar{f}\,A_r\,B_r\,\bar{q}_z\,A_z\\
&+\frac{73}{49}\,\bar{a}_z^2B_z-\frac{178}{31}\,\bar{f}\,{A_z}^2B_z\,\bar{q}_z+\frac{43}{10}\,\bar{f}^2B_z\,{A_r}^4-\frac{47}{15}\,B_r\,\bar{f}^2{A_z}^3A_r\\
&-\frac{44}{63}\,\bar{f}^2{B_z}^3{A_r}^2-\frac{61}{20}\,\bar{f}\,{B_z}^3\bar{q}_z+\frac{202}{11}\,\bar{f}^2{B_z}^3{B_r}^2+\frac{83}{21}\,\bar{h}^2B_z\,{A_r}^2\\
&+\frac{35}{34}\,\bar{a}_z\,\bar{q}_z\,B_z+\frac{65}{57}\,\bar{f}^2B_z\,{B_r}^4-\frac{353}{11}\,\bar{h}^2{A_z}^2B_z+\frac{65}{21}\,\bar{h}^2B_z\,{B_r}^2\\
&-\frac{47}{5}\,B_r\,\bar{f}^2A_z\,{B_z}^2A_r+\frac{61}{2}\,\bar{f}^2{A_z}^2{A_r}^2B_z+21\,\bar{f}\,{A_z}^2B_z\,\bar{a}_z\\
&+\frac{207}{31}\,\bar{h}^2B_r\,A_z\,A_r+\frac{63}{314}\,\bar{f}\,{A_r}^2\bar{a}_z\,B_z+\frac{37}{73}\,B_r\,\bar{f}^2A_z\,{A_r}^3\\
&\left.+\frac{37}{2}\,\bar{f}^2{A_z}^2{B_z}^3-\frac{13}{24}\,\bar{f}^2{B_z}^5\right)
\end{aligned}
\tag{5.58}
$$

$$
\begin{aligned}
\dot{B}_z \;=\;& \epsilon\left(\frac{23}{116}\,\bar{f}\,A_z\,{A_r}^2-\frac{36}{37}\,\bar{f}\,A_z\,{B_r}^2+\frac{187}{20}\,\bar{f}\,A_z\,{B_z}^2-\frac{53}{26}\,\bar{f}\,B_z\,A_r\,B_r\right.\\
&\left.+\frac{30}{17}\,\bar{a}_z\,A_z+\frac{34}{21}\,\bar{q}_z\,A_z+3\,\bar{f}\,{A_z}^3\right)\\
&+\epsilon^2\left(\frac{23}{28}\,\bar{q}_z^2A_z-\frac{76}{3}\,\bar{h}^2{A_z}^3-\frac{73}{49}\,\bar{a}_z^2A_z+\frac{59}{29}\,B_r\,\bar{f}\,A_r\,\bar{q}_z\,B_z\right.\\
&+\frac{47}{5}\,\bar{f}^2{A_z}^2A_r\,B_z\,B_r+\frac{13}{24}\,\bar{f}^2{A_z}^5-\frac{37}{2}\,\bar{f}^2{B_z}^2{A_z}^3-\frac{202}{11}\,\bar{f}^2{A_z}^3{A_r}^2\\
&-\frac{35}{34}\,\bar{a}_z\,\bar{q}_z\,A_z+\frac{353}{11}\,\bar{h}^2A_z\,{B_z}^2-\frac{65}{21}\,\bar{h}^2A_z\,{A_r}^2+\frac{44}{63}\,\bar{f}^2{A_z}^3{B_r}^2\\
&+\frac{61}{20}\,\bar{f}\,{A_z}^3\bar{q}_z-\frac{161}{27}\,\bar{f}\,{A_z}^3\bar{a}_z-\frac{65}{57}\,\bar{f}^2A_z\,{A_r}^4-\frac{43}{10}\,\bar{f}^2A_z\,{B_r}^4-\frac{37}{4}\,\bar{f}^2A_z\,{B_z}^4\\
&-\frac{83}{21}\,\bar{h}^2A_z\,{B_r}^2-\frac{33}{35}\,B_r\,\bar{f}\,A_r\,\bar{a}_z\,B_z-\frac{61}{2}\,\bar{f}^2A_z\,{A_r}^2{B_z}^2-\frac{61}{2}\;\;barf^2A_z\,{B_z}^2{B_r}^2\\
&+\frac{178}{31}\,\bar{f}\,A_z\,{B_z}^2\bar{q}_z-\frac{207}{31}\,\bar{h}^2B_z\,A_r\,B_r-\frac{203}{34}\,\bar{f}\,A_z\,{A_r}^2\bar{a}_z+\frac{37}{28}\,\bar{f}\,{B_r}^2\bar{q}_z\,A_z\\
&-\frac{37}{73}\,\bar{f}^2{A_r}^3B_z\,B_r-21\,\bar{f}\,A_z\,{B_z}^2\bar{a}_z-\frac{63}{314}\,\bar{f}\,A_z\,\bar{a}_z\,{B_r}^2+\frac{47}{15}\,B_r\,\bar{f}^2A_r\,{B_z}^3\\
&\left.-\frac{150}{29}\,\bar{q}_z\,\bar{f}\,A_z\,{A_r}^2+\frac{46}{15}\,\bar{f}^2A_z\,{A_r}^2{B_r}^2-\frac{37}{73}\,\bar{f}^2A_r\,B_z\,{B_r}^3\right)
\end{aligned}
\tag{5.59}
$$

$$
\begin{aligned}
\dot{A}_r \;=\;& \epsilon\left(\frac{8}{11}\,\bar{f}\,{A_z}^2B_r-\frac{4}{27}\,\bar{f}\,{B_z}^2B_r-\frac{11}{118}\,\bar{f}\,{A_r}^2B_r+\frac{19}{32}\,\bar{a}_z\,B_r\right.\\
&\left.+\frac{33}{26}\,\bar{f}\,{B_r}^3-\frac{74}{223}\,\bar{q}_z\,B_r+\frac{35}{23}\,\bar{f}\,A_z\,B_z\,A_r\right)\\
&+\epsilon^2\left(\frac{48}{7}\,\bar{f}^2{B_z}^4B_r+\frac{45}{7}\,\bar{f}^2{A_z}^2{B_r}^3+\frac{63}{37}\,\bar{f}^2{B_r}^3{B_z}^2+\frac{67}{29}\,\bar{h}^2B_r\,{B_z}^2\right.\\
&+\frac{13}{98}\,\bar{h}^2B_r\,{A_r}^2-\frac{6}{23}\,\bar{f}^2{A_z}^4B_r-\frac{21}{58}\,\bar{f}^2{A_r}^4B_r-\frac{11}{101}\,\bar{q}_z\,\bar{a}_z\,B_r+\frac{66}{79}\,\bar{q}_z\,\bar{f}\,{B_r}^3\\
&-\frac{21}{29}\,\bar{f}^2{A_r}^2{B_r}^3+\frac{86}{49}\,\bar{a}_z\,\bar{f}\,{B_r}^3+\frac{62}{21}\,\bar{h}^2{A_z}^2B_r+\frac{17}{15}\,\bar{f}^2A_r\,{B_r}^2A_z\,B_z\\
&+\frac{9}{32}\,\bar{a}_z^2B_r-\frac{14}{79}\,\bar{q}_z^2B_r+\frac{25}{39}\,\bar{f}^2{B_r}^5-\frac{41}{27}\,\bar{f}\,A_z\,B_z\,\bar{q}_z\,A_r-\frac{21}{43}\,\bar{h}^2{B_r}^3\\
&+\frac{19}{27}\,\bar{f}\,A_z\,B_z\,\bar{a}_z\,A_r-\frac{16}{7}\,\bar{f}^2{A_r}^2{B_z}^2B_r+\frac{17}{45}\,\bar{f}^2{A_r}^3A_z\,B_z\\
&-\frac{138}{59}\,\bar{f}^2{A_z}^3B_z\,A_r-\frac{16}{7}\,\bar{f}^2{A_r}^2{A_z}^2B_r-\frac{73}{74}\,\bar{q}_z\,\bar{f}\,{A_z}^2B_r+\frac{27}{7}\,\bar{q}_z\,\bar{f}\,{B_z}^2B_r\\
&+\frac{114}{5}\,\bar{f}^2{A_z}^2{B_z}^2B_r-\frac{138}{59}\,\bar{f}^2A_z\,{B_z}^3A_r+\frac{19}{71}\,\bar{f}\,{A_r}^2B_r\,\bar{q}_z+\frac{25}{167}\,\bar{a}_z\,\bar{f}\,{A_z}^2B_r\\
&\left.-\frac{13}{53}\,\bar{f}\,{A_r}^2B_r\,\bar{a}_z+\frac{49}{11}\,\bar{a}_z\,\bar{f}\,{B_z}^2B_r+\frac{334}{67}\,\bar{h}^2A_z\,B_z\,A_r\right)
\end{aligned}
\tag{5.60}
$$

$$
\begin{aligned}
\dot{B}_r \;=\; & \epsilon\left(\frac{11}{118}\,\bar{f}\,A_r\,{B_r}^2+\frac{4}{27}\,\bar{f}\,{A_z}^2A_r-\frac{8}{11}\,\bar{f}\,{B_z}^2A_r+\frac{74}{223}\,\bar{q}_z\,A_r\right.\\
& \left.-\frac{35}{23}\,\bar{f}\,A_z\,B_z\,B_r-\frac{19}{32}\,\bar{a}_z\,A_r-\frac{33}{26}\,\bar{f}\,{A_r}^3\right)\\
& +\epsilon^2\left(-\frac{13}{98}\,\bar{h}^2{B_r}^2A_r-\frac{48}{7}\,\bar{f}^2{A_z}^4A_r-\frac{25}{39}\,\bar{f}^2{A_r}^5-\frac{66}{79}\,\bar{f}\,{A_r}^3\bar{q}_z-\frac{86}{49}\,\bar{f}\,{A_r}^3\bar{a}_z\right.\\
& +\frac{41}{27}\,\bar{q}_z\,\bar{f}\,A_z\,B_z\,B_r-\frac{63}{37}\,\bar{f}^2{A_r}^3{A_z}^2-\frac{67}{29}\,\bar{h}^2{A_z}^2A_r+\frac{11}{101}\,\bar{q}_z\,\bar{a}_z\,A_r\\
& +\frac{6}{23}\,\bar{f}^2{B_z}^4A_r+\frac{21}{58}\,\bar{f}^2A_r\,{B_r}^4-\frac{62}{21}\,\bar{h}^2A_r\,{B_z}^2+\frac{21}{43}\,\bar{h}^2{A_r}^3\\
& -\frac{45}{7}\,\bar{f}^2{A_r}^3{B_z}^2+\frac{14}{79}\,\bar{q}_z^2A_r+\frac{21}{29}\,\bar{f}^2{A_r}^3{B_r}^2-\frac{17}{15}\,\bar{f}^2{A_r}^2B_r\,A_z\,B_z\\
& -\frac{9}{32}\,\bar{a}_z^2B_r-\frac{19}{27}\,\bar{a}_z\,\bar{f}\,A_z\,B_z\,B_r+\frac{138}{59}\,\bar{f}^2{A_z}^3B_z\,B_r-\frac{19}{71}\,\bar{f}\,{B_r}^2\bar{q}_z\,A_r\\
& +\frac{16}{7}\,\bar{f}^2{B_r}^2{B_z}^2A_r+\frac{138}{59}\,\bar{f}^2{B_z}^3A_z\,B_r-\frac{25}{167}\,\bar{a}_z\,\bar{f}\,{B_z}^2A_r+\frac{13}{53}\,\bar{f}\,A_r\,{B_r}^2\bar{a}_z\\
& -\frac{114}{5}\,\bar{f}^2{A_z}^2A_r\,{B_z}^2-\frac{27}{7}\,\bar{f}\,{A_z}^2\bar{q}_z\,A_r+\frac{73}{74}\,\bar{f}\,{B_z}^2A_r\,\bar{q}_z+\frac{16}{7}\,\bar{f}^2{B_r}^2{A_z}^2A_r\\
& \left.\left.-\frac{49}{11}\,\bar{f}\,{A_z}^2A_r\,\bar{a}_z-\frac{17}{45}\,\bar{f}^2{B_r}^3A_z\,B_z-\frac{334}{67}\,\bar{h}^2B_r\,A_z\,B_z\right)\right. \qquad (5.61)
\end{aligned}
$$

Chapter 6
Summary and concluding remarks

The motivation of this thesis was to investigate dynamics of trapped ions in nonlinear Paul trap mass spectrometers. Three problems have been taken up for investigation in this thesis. These include (1) understanding the early/delayed ejection of ions in mass selective boundary ejection experiments, (2) investigation of the dependence of resolution on scan direction in resonance ejection experiments, and (3) study of coupled nonlinear resonance which causes destabilization of ions within the nominally stable region of the Mathieu stability plot.

In the first problem, the method of multiple scales was used to derive approximate solutions of a weakly nonlinear Mathieu equation in the neighborhood of the stability boundary. This method allowed easy inclusion of higher order multipoles (we included multipole superpositions up to dodecapole) as well as permitted extension of computations to higher orders. The dynamics associated with early and delayed ejection was understood through phase portraits where it was seen that the mechanism of ion ejection was different for positive even multipoles, on the one hand, and negative even multipoles and odd multipoles of either sign, on the other. Through phase portraits, in the first case, it was seen that ion destabilization occurs *before* the nominal stability boundary at $q_z^* = 0.908046$. In the second case, ion motion is stable beyond q_z^*, and ions get destabilized from the trap only when their oscillation amplitude increases beyond the trap boundary. It was further seen that sign of the odd multipoles did not alter dynamics so long as the sign of the individual odd multipoles changed together.

The differential resolution in the forward and reverse scan in resonance ejection experiments was analyzed within the Dehmelt approximation region which is applicable when $q_z < 0.4$. The equation of motion has the form of a damped, forced Duffing equation. Here too, the method multiple scales was used to obtain approximate solution and using this, phase portraits were constructed in different regions close to the jump point of the amplitude response curve. It was seen that the good resolution in froward scan experiment was due to motional coherence at the jump point. In reverse scan experiments it was suggested that lack of coherence for mass spectrometrically relevant scan rates was the cause for poor resolution.

In the study of coupled resonance, an approximate solution of the weakly coupled nonlinear Mathieu equation was derived using harmonic balanced based averaging up to second order. Having demonstrated that the unbounded solutions are caused by coupling

(since r- and z-direction motion in the absence of coupling are individually stable), we proceeded to numerically study the nature of instability in the neighborhood of the invariant manifolds. Several aspects of this very interesting dynamics have been explored and they reveal apparently chaotic ion motion prior to escape.

The important contribution of these studies is that it offers new perspective on the role of field inhomogeneities in altering trap performance. This was possible through development of analytical expressions which enable estimation of the contribution of specific field superpositions in the different problems that we investigated. As shown in our studies, the governing equations were weakly nonlinear and they were not solvable in closed form. Consequently, using perturbation techniques we derived slow flow equations to approximate the original equations. The solution of the slow flow equations were compared with that of original equations and a close match was noted. These slow flow equations are now available for researchers who may wish to analytical expressions in their investigations.

In some sense, the work embodied in this thesis is the culmination of a collaborative effort which began 5 years ago. Inspired by the dynamics of ions in Paul traps, Chatterjee (2002) developed the Harmonic Balance Based Averaging (HBBA) technique to study resonances along the $a_z = 0$ axis of the Mathieu stability plot (Abraham and Chatterjee, 2003). The latter study relied on the fact that when nonlinear resonances occur, axial and drive frequency have a simple rational relationship. Using this, Abraham (2002), Abraham et al. (2004) and Prasanna (2005) demonstrated that the $\beta = 2/3$, $\beta = 1/2$, and $\beta = 2/5$ were primarily influenced by hexapole, octopole and decapole superpositions, respectively. The above studies, the investigations in this thesis and the reports in Rajanbabu et al. (2006a, 2006b) are perhaps the first formal use of the techniques of nonlinear dynamics to Paul trap mass spectrometry. The utility of these results may gain importance in coming years which will see a renewed interest in novel trap geometries for their ability to be miniaturized and made portable.

References

[1] Abraham, G. T. (2002) *Escape Velocity and Ejection via Nonlinear Resonances in Paul Traps*, Unpublished MSc (Engg.) thesis, Department of Instrumentation, Indian Institue of Science, Bangalore, India.

[2] Abraham, G. T. and Chatterjee, A. (2003) Approximate asymptotics for a nonlinear Mathieu equation using harmonic balance based averaging, *Nonlinear Dynamics*, 31, 347-365.

[3] Abraham, G. T., Chatterjee, A. and Menon, A. G. (2004) Escape velocity and resonant ion dynamics in Paul trap mass spectrometers, *International Journal of Mass Spectrometry*, 231, 1-16.

[4] Abromowitz, M. and Stegun, I.A. (1970) *Handbook of Mathematical Functions*, Dover, New York.

[5] Alheit, R., Hennig, C., Morgenstern, R., Vedel, F. and Werth, G. (1995) Observation of instabilities in a Paul trap with higher order anhormonicities, *Applied Physics B*, 61, 277-283.

[6] Alheit, R., Kleineidam, S., Vedel, F., Vedel, M. and Werth, G. (1996) Higher order non-linear resonances in a Paul trap, *International Journal of Mass Spectrometry and Ion Processes*, 154, 155-169.

[7] Arnold, N. S., Hars, G. and Meuzelaar, H. L. C. (1994) Extended theoretical consideration in the resonance ejection mode of quadrupole ion trap mass spectrometry, *Journal of American Society for Mass Spectrometry*, 5, 676-688.

[8] Austin, D. E., Cruz, D. and Blain, M. G. (2006) Simulations of ion trapping in a micrometer-sized cylindrical ion trap, *Journal of American Society for Mass Spectrometry*, 17, 430-441.

[9] Blain, M. G., Riter, L.S., Cruz, D., Austin, D. E., Wu, G., Plass, W. R. and Cooks, R. G. (2004) Towards the hand-held spectrometer: design considerations, simulation,

and fabrication of micrometer-scaled cylindrical ion traps, *International Journal of Mass Spectrometry*, 236, 91-104.

[10] Beaty, E. C. (1986) Calculated electrostatic properties of ion traps, *Physical Review A*, 33, 3645-3656.

[11] Bonner, R. F., Fulford, J. E. and March, R. E. (1977) The cylindrical ion trap. Part I. General introduction, *International Journal of Mass Spectrometry and Ion Physics*, 24, 255-269.

[12] Brown, L.S. and Gabrielse, G. (1986) Geonium theory: Physics of single electron or ion in a Penning trap, *Review of Modern Physics*, 58, 233-311.

[13] Chatterjee, A. (2002) Harmonic balance based averaging: Approximate realizations of an assymptotic technique, *Nonlinear Dynamics*, 32, 323-343.

[14] Chatterjee, A. and Chatterjee, D. (2006) Analytical investigation of hydrodynamic cavitation control by ultrasonics, *Nonlinear Dynamics* (in press).

[15] Collings, B. A. (2005) Increased fragmentation efficiency of ions in a low pressure linear ion trap with an added dc octopole field, *Journal of American Society for Mass Spectrometry*, 16, 1342-1352.

[16] Collings, B. A., Stott, W. R. and Londry, F. A. (2003) Resonant excitation in a low-pressure linear ion trap, *Journal of American Society for Mass Spectrometry*, 14, 622-634.

[17] Chu, X. Z., Holzki, M., Alheit, R. and Werth, G. (1998) Observation of high-order non-linear resonances of an ion cloud in a Paul trap, *International Journal of Mass Spectrometry and Ion Processes*, 173, 107-112.

[18] Cooks, R. G. and Rockwood, A. L. (1991) The 'Thomson'. A suggested unit for mass spectroscopy, *Rapid Communications in Mass Spectrometry*, 5, 93.

[19] Cox, K. A., Cleven, C. D. and Cooks, R.G. (1995) Mass shifts and local space charge effects observed in the quadrupole ion trap at higher resolution, *International Journal of Mass Spectrometry and Ion Processes*, 144, 47-65.

[20] Das, S. L. and Chatterjee, A. (2003) Multiple scales via Galerkin projections: Approximate asymptotics for strongly nonlinear oscillations, *Nonlinear Dynamics*, 32, 161-186.

[21] Dawson, P. H. (1976) *Quadrupole Mass Spectrometry and its Application*, Elsevier, Amsterdam.

[22] Dawson, P. H. and Whetten, N. R. (1968a) Ion storage in the three dimensional rotationally symmetric quadrupole fields I - A theoretical treatment, *Journal of Vacuum Science and Technology*, 5, 1-10.

[23] Dawson, P. H. and Whetten, N. R. (1968b) Ion storage in the three dimensional rotationally symmetric quadrupole fields II - A sensitive mass spectrometer, *Journal of Vacuum Science and Technology*, 5, 11-18.

[24] Fischer, E. (1959) Die dreidimensionale Stabilisierung von Ladungstragern in einem Vierpolfeld, *Zeitschrift Für Physik*, 156, 1-26.

[25] Franzen, J. (1993) The non-linear ion trap. Part 4. Mass selective instability scan with multipole superposition, *International Journal of Mass Spectrometry and Ion Processes*, 125, 165-170.

[26] Franzen, J. (1994) The non-linear ion trap. Part 5. Nature of non-linear resonances and resonant ion ejection, *International Journal of Mass Spectrometry and Ion Processes*, 130, 15-40.

[27] Franzen, J., Gabling, R. H., Schubert, M. and Wang, Y. (1995) Non-linear ion traps. In: R. E. March, J. F. J. Todd (Eds.), *Practical Aspects of Ion Trap Mass Spectrometry*, Volume 1, CRC Press, New York, Chapter 3, pp. 49-167.

[28] Fulford, J. E., Hoa, D.-N., Hughes, R. J., March, R. E., Bonner, R.F. and Wong, G.J. (1980) Radio-frequency mass selective excitation and resonant ejection of ions in a three-dimensional quadrupole ion trap, *Journal of Vacuum Science and Technology*, 17, 829-835.

[29] Fulford, J. E. and March, R. E. (1978) A new mode of operation for the three dimensional quadrupole ion store (QUISTOR): The selective ion reactor, *International Journal of Mass Spectrometry and Ion Processes*, 26, 155-162.

[30] Goeringer, D. E., Whitten, W. B., Ramsey, J. M., McLuckey, S. A. and Glish, G. L. (1992) Theory of high-resolution mass spectrometry achieved via resonance ejection in the quadrupole ion trap, *Analytical Chemistry*, 64, 1434-1439.

[31] Guidugli F. and Traldi P. (1991) A phenomenological description of a black hole for collisionally induced decomposition products in ion trap mass spectrometry, *Rapid Communination in Mass Spectrometry*, 5, 343-348.

[32] Guidugli F., Traldi P., Franklin A. M., Langford M. L., Murrel J. and Todd J. F. J. (1992) Further thoughts on the occurrence of black holes in ion trap mass spectrometry, *Rapid Communication in Mass Spectrometry*, 6, 229-231.

[33] Guckenheimer, J. and Holmes, P. (1983) *Nonlinear Oscillations, Dynamical Systems, and Bifurcations of Vector Fields*, Springer-Verlag, New York.

[34] Guzzo, M., Lega, E. and Froeschle, C. (2002) On the numerical detection of the effective stability of chaotic motions in quasi-integrable systems, *Physica D*, 163, 125.

[35] Hilborn, R. C. (1994) *Chaos and Nonlinear Dynamics. An Introduction for Scientists and Engineers*, Oxford University Press, UK.

[36] Hinch, E. J. (1991) *Perturbation Methods*, Cambridge University Press, UK.

[37] Holmes, M. J. (1991) *Introduction to Perturbation Methods*, Springer-Verlag, New York.

[38] Knight, R. D. (1983) The general form of the quadrupole ion trap potential, *International Journal of Mass Spectrometry and Ion Physics*, 51, 127-131.

[39] Kevorkian J. and Cole J. D. (1996) *Multiple Scale and Singular Perturbation Methods*, Applied Mathematical Sciences 114, Springer-Verlag, New York.

[40] Landau, L. D. and Lifshitz, E. M. (1976) *Mechanics*, Third Edition, Pergamon, UK.

[41] Langmuir, D. B., Langmuir, R. V., Shelton, H. and Wuerker, R. F. (1962) Containment device, U. S. Patent 3,065,640.

[42] Louris, J., Schwartz, J., Stanfford, G., Syka, J. and Taylor, D. (1992) Proceedings of the 40th ASMS conference on Mass Spectrometry and Allied Topics, Washington D. C., 1003.

[43] Luo, X., Zhu, X., Gao, K., Li, J., Yan, M., Shi, L. and Xu, J. (1996) Origin and manifestation of the anharmonic potential felt in an ion-cloud in an actual Paul trap, *Applied Physics B*, 62, 421-426.

[44] Major, F. G. and Dehmelt, H. G. (1967) Exchange-collision for the rf spectroscopy of stored ions, *Physical Review*, 170, 91-107.

[45] Makarov, A. A. (1996) Resonance ejection from the Paul trap: A theoretical treatment incorporating a weak octopole field, *Analytical Chemistry*, 68, 4257-4263.

[46] Marathe, A. (2006) PhD thesis under preparation, Department of Mechanical Engineering, Indian Institue of Science, Bangalore, India.

[47] March, R. E. (1992) Ion trap Mass Spectrometry, *International Journal of Mass Spectrometry and Ion Processes*, 118/119, 72-135.

[48] March, R. E. and Hughes, R. J. (1989) *Quadrupole Storage Mass Spectrometry*, Wiley-Interscience, New York.

[49] March, R. E. and Londry, F. A. (1995) Introduction to practical aspects of ion trap mass spectrometry. In: March, R. E. and Todd, J. F. J. (Eds.) *Practical Aspects of Ion Trap Mass Spectrometry*, Volume 1, CRC Press, New York, Chapter 2, pp. 25-48.

[50] March, R. E., McMahon, A. W., Allinson, E. T., Londry, A. F., Alfred, R.L., Todd, J. F. J. and Vedel, F. (1990a) Resonance excitation of ions stored in a quadrupole ion trap. Part 1. A simulation study, *International Journal of Mass Spectrometry and Ion Processes*, 95, 119-156.

[51] March, R. E., McMahon, A. W., Allinson, E. T., Londry, A. F., Alfred, R.L., Todd, J. F. J. and Vedel, F. (1990b) Resonance excitation of ions stored in a quadrupole ion trap. Part 2. Further simulation studies, *International Journal of Mass Spectrometry and Ion Processes*, 99, 109-124.

[52] March R. E. and Todd, J. F. J. (1995) *Practical Aspects of Ion Trap Mass Spectrometry*, Volume 1, CRC Press, New York.

[53] McLachlan, N. W. (1947) *Theory and Applications of Mathieu Functions*, Oxford University Press, UK.

[54] McLachlan, N. W. (1958) *Ordinary Non-linear Differential Equations in Engineering and Physical Sciences*, Oxford University Press, UK.

[55] Michaud, A. L., Frank, A. J., Ding, C., Zhao, X.-Z. and Douglas, D. J. (2005) Ion excitation in a linear quadrupole ion trap with an added octopole field, *Journal of American Society for Mass Spectrometry*, 16, 835-849.

[56] Mitropol'skii, Y. A. (1965) *Problems of the Assymptotic Theory of Nonstationary Vibrations*, Israel Program for Scientific Translations, Jerusalem.

[57] Morand, K. L., Lammert, S. A. and Cooks R. G. (1991) Concerning black holes in ion trap mass spectrometry, *Rapid Communications in Mass Spectrometry*, 5, 491.

[58] Nandakumar, K. and Chatterjee, A. (2004) The simplest resonance capture problem, using harmonic balance based averaging. *Nonlinear Dynamics*, 37, 271284.

[59] Nandakumar, K. and Chatterjee, A. (2005a) Resonance, parameter estimation, and modal interactions in a strongly nonlinear benchtop oscillator, *Nonlinear Dynamics*, 40, 149-167.

[60] Nandakumar, K. and Chatterjee, A. (2005b) Higher-order pseudoaveraging via harmonic balance for strongly nonlinear oscillations. Transactions ASME *Journal of Vibration and Acoustics*, 127, 416-419.

[61] Nayfeh, A. H. (1973) *Perturbation Methods*, Wiley Interscience, New York.

[62] Nayfeh, A. H. and Mook, D.T. (1979) *Nonlinear Oscillations*, Wiley Interscience, New York.

[63] Ott, E. (1993) *Chaos in Dynamical System*, Cambridge University Press, UK.

[64] Paul, W. and Steinwedel, H. (1960), U.S. Patent No. 2939952.

[65] Plass, W. R., Li, H. and Cooks, R. G. (2003) Theory, simulation and measurement of chemical mass shifts in RF quadrupole ion traps, *International Journal of Mass Spectrometry*, 228, 237-267.

[66] Prasanna, N. (2005) *Study of the $\beta = \frac{2}{5}$ Resonance and Resonace Excitation in Nonlinear Traps*, Unpublished MSc (Engg.) thesis, Department of Instrumentation, Indian Institue of Science, Bangalore, India.

[67] Rajanbabu, N., Chatterjee, A. and Menon, A. G. (2006a) Motional coherence during resonance ejection of ions from Paul traps, to appear in *International Journal of Mass Spectrometry*.

[68] Rajanbabu, N., Marathe, A., Chatterjee, A. and Menon, A. G. (2006b) Multiple scales analysis of early and delayed boundary ejection in Paul traps, to appear in *International Journal of Mass Spectrometry*.

[69] Rand, R. H., (1994) *Topics in Nonlinear Dynamics with Computer Algebra*, Computation in Education, Volume 1, Gordon and Breach Science Publishers, Langhorne, PA, USA.

[70] Rand, R. H. (2005) *Lecture Notes on Nonlinear Vibrations*, Version 36, available online at http://www.tam.cornell.edu/randdocs/.

[71] Rand, R. H. and Armbruster, D. (1987) *Perturbation Methods, Bifurcation Theory and Computer Algebra*, Springer, Berlin.

[72] Schwartz, J. C., Senko, M. W. and Syka, J. E. P. (2002) A two-dimensional quadrupole ion trap mass spectrometer, *Journal of American Society for Mass Spectrometry*, 13, 659-669.

[73] Sevugarajan, S. and Menon, A. G. (1999) Field imperfection induced axial secular frequency shifts in non-linear ion traps, *International Journal of Mass Spectrometry*, 189, 53-61.

[74] Sevugarajan, S. and Menon, A. G. (2001) Frequency perturbation in nonlinear Paul traps: a simulation study of the effect of geometric aberration, space charge, dipolar excitation, and damping on ion axial secular frequency, *International Journal of Mass Spectrometry*, 197, 263-278.

[75] Sevugarajan, S. and Menon, A. G. (2002) Transition curves and iso-β_u lines in non-linear Paul traps, *International Journal of Mass Spectrometry*, 218, 181-196.

[76] Stafford, G. C., Kelley, P. E, Syka, J. E. P, Reynolds, W. E. and Todd, J. F. J. (1984) Recent improvements in and analytical applications of advanced ion trap technology, *International Journal of Mass Spectrometry and Ion Processes*, 60, 85-98.

[77] Stoker, J. J. (1950) *Nonlinear Vibrations in Mechanical and Electrical Systems*, Interscience, New York.

[78] Strogatz, S. H. (1994) *Nonlinear Dynamics and Chaos*, Addison-Wesley, New York.

[79] Sudakov, M. (2001) Effective potential and the ion axial beat motion near the boundary of the first stable region in a non-linear ion trap, *International Journal of Mass Spectrometry*, 206, 27-43.

[80] Sugiyama, K. and Yoda, J. (1990) Anharmonic oscillations of ions trapped in a RF trap with light buffer gas, *Applied Physics B*, 51, 146-152.

[81] Syka, J. (1995) Commercialization of the quadrupole ion trap. In: March, R. E. and Todd, J. F. J. (Eds.) *Practical Aspects of Ion Trap Mass Spectrometry*, Volume 1, CRC Press, New York, Chapter 4, pp. 169-205.

[82] Vedel, F., Vedel, M. and March, R. E. (1990) New schemes for resonant ejection in R.F. quadrupolar ion traps, *International Journal of Mass Spectrometry and Ion Processes*, 99, 125-138.

[83] Verhulst, F. (1990) *Nonlinear Differential Equations and Dynamical systems*, Springer-Verlag, Berlin.

[84] Wang, Y. and Franzen, J. (1994) The non-linear ion trap. Part 3. Multipole components in three types of practical ion traps, *International Journal of Mass Spectrometry and Ion Processes*, 132, 155-172.

[85] Wang, Y., Franzen, J. and Wanczek, K. P. (1993) The non-linear resonance ion trap. Part 2. A general theoretical analysis, *International Journal of Mass Spectrometry and Ion Processes*, 124, 125-144.

[86] Wells, J. M., Plass, W. R, Patterson, G. E, Ouyang, Z., Badman, R. E. and Cooks, R. G. (1999) Chemical mass shifts in ion trap mass spectrometry: Experiments and simulations, *Analytical Chemistry*, 71, 3405-3415

[87] Williams, J. D., Cox, K. A., Cooks, R. G., McLuckey, S.A., Hart, K.J. and Goeringer, D.E. (1994) Resonance ejection ion trap mass spectrometry and nonlinear field contributions: The effect of scan direction on mass resolution, *Analytical Chemistry*, 66, 725-729.

[88] Wu, G., Cooks, R. G. and Ouyang, Z. (2005) Goemetry optimization for the cylindrical ion trap: field calculations, simulations and experiments, *International Journal of Mass Spectrometry*, 241, 119-132.